

Editorial corner – a personal view

Is the use of correct terms and definitions important in creation of new materials?

S. Fakirov*

Centre for Advanced Composite Materials, Department of Mechanical Engineering, The University of Auckland, Private Bag 92019, Auckland, New Zealand

The best example of non-proper use of a well-defined and widely applied term is a case in composite community, where the thermodynamic term ‘*phase*’ is used instead of the term ‘*component*’. Obviously, the misuse of the term ‘*phase*’ is a remnant from the time when the colloid chemistry was formulated (second half of 19th century, i.e. long before the polymer science was defined). The confusion of this misuse can be easily demonstrated by poly(vinylidene fluoride) (PVDF) exhibiting five crystalline polymorphic modifications (phases!) and one amorphous phase but PVDF is still a one-component system.

While this example does not have a direct effect on the creation of new materials, the next one, the definition of the relatively new type of polymer composites, the *single polymer composites* (SPCs), does. SPCs have also been called: *one polymer composites* (R. Porter), *homocomposites*, *self-reinforced composites*, *one-phase composites*, *homogeneous composites*, or *all-polymer composites*. The concept of SPCs has been formulated by R. Porter some 40 years ago (DOI: [10.1007/BF00554928](https://doi.org/10.1007/BF00554928)) as attempt to solve the basic problem in polymer science and technology, namely, the low adhesion quality between matrix and reinforcement due to their different chemical composition. The approach is quite simple – the matrix and the reinforcement have to be of the same polymer, i.e. to be chemically identical. The idea attracted the attention of academia and industry during the last decade when patents were registered and products were commercialized; nanofibrillar SPCs with superior mechanical properties were also created (DOI:

[10.1002/mame.201200226](https://doi.org/10.1002/mame.201200226)). What is more, similar products were prepared and called also SPCs (DOIs: [10.1007/s10853-009-3792-1](https://doi.org/10.1007/s10853-009-3792-1), and [10.1016/j.compscitech.2013.12.006](https://doi.org/10.1016/j.compscitech.2013.12.006)) using highly oriented polypropylene (PP) (as reinforcement) and the random copolymer of PP (usually with polyethylene) as a matrix thus neglecting the basic requirement (R. Porter) for identical chemical composition of matrix and reinforcement. Strictly speaking, such composites belong to the category of polymer–polymer composites. The same holds for thermoplastic copolyesters reinforced with ‘homo’-poly(ethylene terephthalate). The argument that the two chemically different components belong to the same polymer family (DOI: [10.1016/j.compscitech.2013.12.006](https://doi.org/10.1016/j.compscitech.2013.12.006)) could hardly be seriously considered – it only smears the boundary between the two types of composites, the polymer-polymer ones and the SPCs and makes the clear definition of single polymer composites hardly possible affecting in this way negatively their further development! In order to make use of the unique properties of SPCs we should not forget that they could be multi-phase but always remain one-component systems!



Prof. Dr. Stoyko Fakirov
Member of International Advisory Board

*Corresponding author, e-mail: s.fakirov@auckland.ac.nz
© BME-PT

Natural rubber/graphene oxide composites: Effect of sheet size on mechanical properties and strain- induced crystallization behavior

X. Wu¹, T. F. Lin¹, Z. H. Tang¹, B. C. Guo^{1*}, G. S. Huang²

¹Department of Polymer Materials and Engineering, South China University of Technology, 510640 Guangzhou, People's Republic of China

²College of Polymer Science and Engineering, State Key Laboratory of Polymer Materials Engineering, Sichuan University, 610065 Chengdu, People's Republic of China

Received 10 November 2014; accepted in revised form 1 February 2015

Abstract. In order to analyze the influence of the lateral size of graphene oxide (GO) on the properties of natural rubber/graphene oxide (NR/GO) nanocomposites, three different sized graphene oxide sheets, namely G1, G2 and G3 were used to fabricate a series of NR/GO nanocomposites by latex mixing. The results indicate that adding GO can remarkably increase the modulus of NR. The enhancement of modulus is strongly dependent on the size of GO sheets incorporated. G1 with smallest sheet size gives the maximum reinforcement effect compared with G2 and G3. Dynamic mechanical measurement and swelling ratios (Q_f/Q_g) indicate that G1 has stronger interfacial interaction with NR. XRD shows G1 is more effective in accelerating the strain-induced crystallization (SIC) of NR. The strong interfacial interaction facilitates the stress transfer and strain-induced crystallization, both of which lead to the improved modulus.

Keywords: nanocomposites, size effect, natural rubber, SIC, graphene oxide

1. Introduction

Nowadays, rubber technology has become an important part in industry; nevertheless, the low strength and modulus limit its applications in many cases. So, it needs to be filled with various fillers to achieve optimum properties for practical purposes. Among a variety of reinforcing fillers, graphene (GE) as a new type of nanofiller has attracted increasing interest since it has a thin-layered 2D structure, high specific surface area, excellent mechanical properties, thermal properties and electrical properties [1–3]. The excellent mechanical properties of the natural rubber would be attributed to strain-induced crystallization (SIC) [4–6]. The reinforcement effect of filler on NR is variously attributed to ‘strain amplification’ and ‘stress transfer’ through the filler net-

work [7–9]. Nanofillers are of remarkable influence on the strain-induced crystallization of NR because of their strong interfacial interaction with polymer matrix [10]. The introduction of filler in NR changes the stress field, increases the local strain of the chain, makes SIC to start at a lower strain, which is called ‘strain amplification’ [11]. In order to obtain high effective reinforcement, a sufficient load transfer from polymer to reinforcing fillers is required. On application of an external stress, the polymer matrix undergoes greater strain than the filler, resulting in shear stresses at the polymer-filler interfaces [12]. The matrix shear stress increases with the external stress and is transferred to the fillers until the failure of the filler-polymer interfaces. Strong interfaces are able to support large interfacial stresses and pro-

*Corresponding author, e-mail: psbcguo@scut.edu.cn
© BME-PT

duce excellent mechanical properties of the composites.

As a precursor of graphene, GO also exhibits high strength and modulus [13, 14]. Due to its excellent hydrophilicity and the availability of a latex form for most rubbers, GO can be incorporated into rubbers via the latex co-coagulation process for reinforcement [15]. As for examples, Kang *et al.* [16] reported that with 1.9 vol% GO, the tensile strength and tear strength of carboxylated acrylonitrile butadiene rubber/graphene oxide (XNBR/GO) increased by 357 and 117%, respectively. There is hydrogen bonding between GO and XNBR, since both contain many oxygen-containing groups. Hence, the strong interfacial interactions would promote the dispersion of GO and facilitate the load transfer from XNBR to the GO sheets. Moghaddam *et al.* [17] prepared NR/rGO nanocomposites by thermodynamically favorable self-assembly of GO at oil-water interfaces and found improvements in the modulus and ultimate strength of the nanocomposites. Mao *et al.* [18] prepared styrene-butadiene rubber (SBR)/GO nanocomposites by combined latex compounding and spray drying. With 5 phr GO, the composite exhibited 7.8 times higher modulus at 300% strain and 6.4 times higher tensile strength compared with the pure SBR.

It is well known that the filler size is an important factor that determines the overall performances of the resulting nanocomposite, but there are rarely reports concerning the size effect of graphene. Wang *et al.* [19] prepared SBR composites with different size of fillers and found that the fillers with smaller size exhibited higher reinforcing efficiency towards SBR as they could reach so-called critical particle-particle distance for reinforcement at lower filler content. But the tensile strength was almost unchanged when the filler size became small enough. Khan *et al.* [20] found that as the flake size of graphene decreased, the Young's modulus of polyurethane/graphene composites fell dramatically while the ultimate tensile strength and the strain at break rose slightly. Choi *et al.* [21] reported that functionalized graphene sheets (FGS) with a larger particle size have better reinforcement in 5% secant modulus of thermoplastic polyurethane/functionalized graphene sheets nanocomposites, but lower in tensile strength and elongation at break. He proposed that the stress transfer from matrix polymer to dispersed FGS will

be more effective when the aspect ratio of the filler is larger. Chatterjee *et al.* [22] studied the influence of graphene nanoplatelets (GnPs) size on composite properties, pointed that the bigger size of graphene nanoplatelets resulted in greater reinforcement of fracture toughness and flexural modulus for epoxy resin at all GnPs concentrations. He ascribed this to the higher aspect ratio and load transfer efficiency of larger size GnPs. Wang *et al.* [23] got an opposite conclusion, he studied the mechanism of graphene oxide toughening epoxy and suggested that graphene oxide with smaller sheet size were highly effective in resisting crack propagation and gave the maximum reinforcement effect in fracture toughness compared with larger ones. These contradictory results may be due to the fact that the properties of polymer composites are affected by multi-factors including filler types and dispersion, filler-polymer interaction, and polymer matrices [24–26]. Herein, the graphene and matrix types as well as the nanocomposite manufacturing technique account for the discrepancies [27]. So far, although a few studies on polymer/graphene composites have been made, some questions still remain.

Considering that NR is a strategically important material with unique SIC behavior and the NR/GO composites are widely reported, the effects of GO size on the properties of the composites are generally ignored. Herein, we prepare a series of NR/GO nanocomposites filled with different GO sizes through latex co-coagulation technology, and aim to evaluate the effect of GO size on the mechanical properties of NR/GO nanocomposites and discuss its influence on SIC of natural rubber.

2. Experimental

2.1. Materials

NR latex (60 wt% of NR content) was obtained from the China Hainan Rubber Industry Group Co., Ltd. Three sizes of graphite flakes were purchased from Qing Dao JinRiLai Graphite CO. Ltd (China). Their average size is 10000, 325 and 50 mesh, respectively. The reagents including concentrated sulfuric acid (H₂SO₄), hydrochloric acid (HCl), calcium chloride (CaCl₂), potassium permanganate (KMnO₄) and sodium nitrate (NaNO₃) were analytically pure and commercially available. All the rubber ingredients were industrial grade and used as received.

2.2. Preparation of graphite oxide

Graphite oxide was prepared by oxidizing natural graphite powder (or expanded graphite) based on a modified Hummers method [28]. Typically, 10 g of graphite powder (or expanded graphite) and 5 g of NaNO_3 were added into 230 mL of concentrated H_2SO_4 in an ice bath. Under vigorous stirring, 30 g of KMnO_4 was gradually added within 1 h. The mixture was then stirred at 35°C for 0.5 h, followed by diluting with 460 mL of deionized (DI) water. The temperature of the mixture was maintained at 90°C for 15 min. The reaction was terminated by adding 1400 mL of DI water and 25 mL of H_2O_2 aqueous solution (30%). The obtained graphite oxide slurry was filtered and washed with diluted HCl aqueous solution to remove metal ions. Finally, the product was washed with DI water repeatedly until it was neutral. The obtained graphite oxide was then exfoliated in water via sonication to form GO suspension. The GO powder was denoted as G1, G2 and G3 according to different size of GO sheets.

The graphite flakes with the size of 10000 and 325 mesh were directly oxidized. The graphite flakes with the size of 50 mesh were thermally expanded before oxidizing for their strong interlayer interactions. Natural graphite flakes (50 mesh) and sulfuric acid were mixed and then nitric acid was added into the mixture. After magnetic stirring for 24 h, the mixture was washed with DI water to neutral and dried to obtain graphite intercalation compound (GIC). The dry GIC powder was expanded in a microwave oven for 20 second to obtain expanded graphite (EG).

2.3. Preparation of NR/GO composites

A desired amount of GO suspension was added into the NR latex and stirred to produce homogeneous mixtures. After 1 h stirring, the resulting mixture was co-coagulated by adding CaCl_2 (1.0 wt%) aqueous solutions as the flocculating agents. The co-coagulated compounds were washed with de-ionized water several times until no chloride ion was detected. After that, the compounds were vacuum dried at 50°C over night. Then the dried compounds were compounded with rubber ingredients with a two-roll mill and subjected to compression at 150°C for the optimum curing time determined by the U-CAN UR-2030 vulcameter. The formulation of the composite

is as follows: NR 100 phr, sulfur 2 phr, ZnO 5 phr, CZ 0.9 phr, stearic acid 1 phr and 4010NA 1 phr (where phr means parts per 100 parts of rubber).

2.4. Characterization

To measure the size of GO sheets, the GO droplets were applied on the silicon wafer and dried to take clear images of GO under scanning electron microscope (SEM) (FESEM, Hitachi S-4800). The cross section of tensile fractured surfaces after tensile test was examined by SEM. Before testing, these samples were sputter coated with Au. The measurement of the mechanical properties was conducted on a universal testing machine (GOTECH AI-7000S, Taiwan) at room temperature with a cross-head speed of 500 mm/min. X-ray photoelectron spectroscopy (XPS) analysis was carried out on a Kratos Axis Ultra DLD with Al K α radiation (1486.6 eV). X-ray diffraction (XRD) analysis was performed using an X'pert Pro diffractometer (Panalytical, Netherlands). The X-ray beam was Cu K α ($\lambda = 0.1548$ nm) radiation operated at 40 kV and 40 mA. The samples at different strain ratio were fixed in a homemade fixture and scanned for the XRD tests.

Dynamic mechanical properties were determined by a dynamic mechanical analyzer Q800 (TA Instrument, Inc., USA). The tests were carried out at frequency of 1 Hz, strain 0.01 (1%), temperature range -100 to $+30^\circ\text{C}$ with a heating rate of $3^\circ\text{C}/\text{min}$ under tensile mode. The strain sweep experiments were conducted in a strain range of 0.01–200% at 60°C under 1 Hz using RPA2000 rubber process analyzer (Alpha Technologies Co., Akron, USA). The samples used in the RPA measurement were the unvulcanized compounds containing curing additives.

The rubber–filler interaction was determined using Park and Lorenz equation [29] (Equation (1)):

$$\frac{Q_f}{Q_g} = ae^{-z} + b \quad (1)$$

where the subscripts f and g refer to filled and gum vulcanizates, respectively; z is the ratio by weight of the filler to the rubber hydrocarbon in the vulcanizates; and a and b are constants. Q_f and Q_g are the toluene uptake per gram of filled and gum vulcanizates, respectively, which are measured as following. The cured sample is immersed in toluene until equilibrium swelling for 48 h at 25°C . The samples

were dried in an oven at 60°C until constant weights were obtained. The toluene uptake per gram of rubber (Q) was determined using Equation (2):

$$Q = \frac{W_s - W_d}{W_0 \cdot \varphi} \quad (2)$$

where W_s is the swollen weight, W_d is the dried weight, W_0 is the original weight, and φ is the mass fraction of the rubber in the composites.

3. Results and discussion

3.1. Characterization of three types of GO sheets

There are various factors which would affect the size of GO sheets, such as degree of oxidation [30, 31], controlled centrifugation [32], pH value [33], shaking or sonication [34]. Unfortunately, these methods are not suitable for mass production due to their low yield. So the large scale production of high-

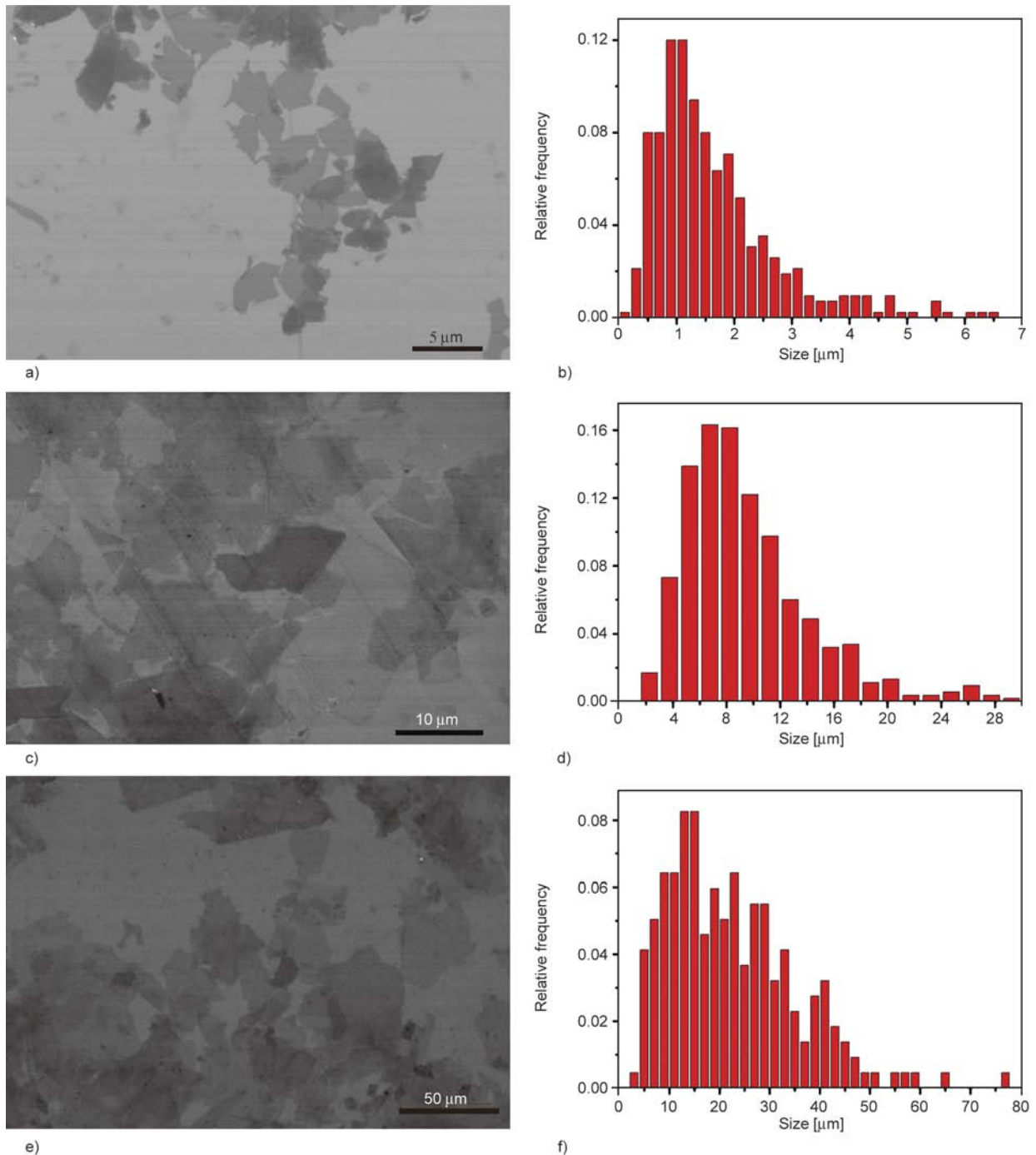


Figure 1. Typical SEM images of (a) G1, (c) G2, (e) G3, and the histograms for the size distribution of (b) G1, (d) G2, (f) G3

quality GO sheets with controlled size still remains a significant challenge. According to Zhou and Liu's [35] study, the size of the exfoliated GO sheets are closely associated with those of the starting graphite flakes. In this paper, a simple and effective strategy to tune the size of GO sheets was used by selecting suitable starting graphite materials. The average size of three kinds of graphite flakes are 10 000, 325 and 50 mesh, respectively.

The morphology and size of GO sheets were examined by SEM. Figure 1 presents the SEM images of three types of GO sheets and their corresponding size distributions. The size distributions histograms were obtained based on the measurement of the SEM images for more than 200 sheets for each sample. Obviously, there is an increase in size from G1 to G3. The mean lateral size of G1, G2 and G3 sheets, obtained from the SEM size statistical analysis, are 1.71, 9.52 and 22.44 μm , respectively.

The surface chemistry of GO sheets is significantly influenced by the GO size. Thus XPS measurements were carried out to analyze the surface chemical composition of the three types of GO sheets in Figure 2a and the corresponding carbon assignments are summarized in Table 1. The peaks at 284.6, 286.4 and 288.5 eV are assigned to C–C, C–O and C=O functional groups, respectively [36]. The C/O atomic ratio is an important parameter for evaluating the degree of oxidation of GO sheets. It can be seen that there is little change of C/O atomic ratio among the three types of GO sheets, showing that the degree of oxidation of them are similar.

The X-ray diffraction (XRD) peaks of three types of GO papers are shown in Figure 2b. For all the GO papers, the 2θ values are around 11° and the typical

Table 1. Relative atomic percentage of GO sheets of different size

	C/O	C–C [%]	C–O [%]	C=O [%]
G1	1.95	39.3	58.26	2.42
G2	1.81	38.39	60.07	1.54
G3	1.86	41.26	55.33	3.4

(002) diffraction peak at 26.5° for natural graphite has completely disappeared. The interlayer spacing in GO sheets is proportional to the degree of oxidation [30]. The d-spacing between the adjacent GO sheets are 7.68, 8.62 and 7.82 \AA for G1, G2 and G3 papers, respectively. The d-spacing is quite consistent with the C/O atomic ratio of three types of GO sheets. Generally, the GO papers with lower C/O atomic ratio have higher d-spacing, this can be explained by higher degree of functionalization. The GO sheets with more oxygenated functional groups can absorb more water through hydrogen bonding during film formation, inevitably increasing the interlayer distance to accommodate the water molecules [37].

3.2. The dispersion state of the GO sheets in the NR/GO nanocomposites

It is well-known that the dispersion state of the filler and the interfacial interactions are two crucial factors in governing the performance of the composite [17]. The dispersion of the GO sheets in the nanocomposites was characterized by XRD. Figure 3 shows the XRD patterns of NR/GO nanocomposites with 2 phr GO with different sizes. The broad diffraction peak around 20° is noncrystalline structure of NR, while the diffraction peaks between $30\text{--}50^\circ$ are assigned to ZnO particles in the vulcanizates [38].

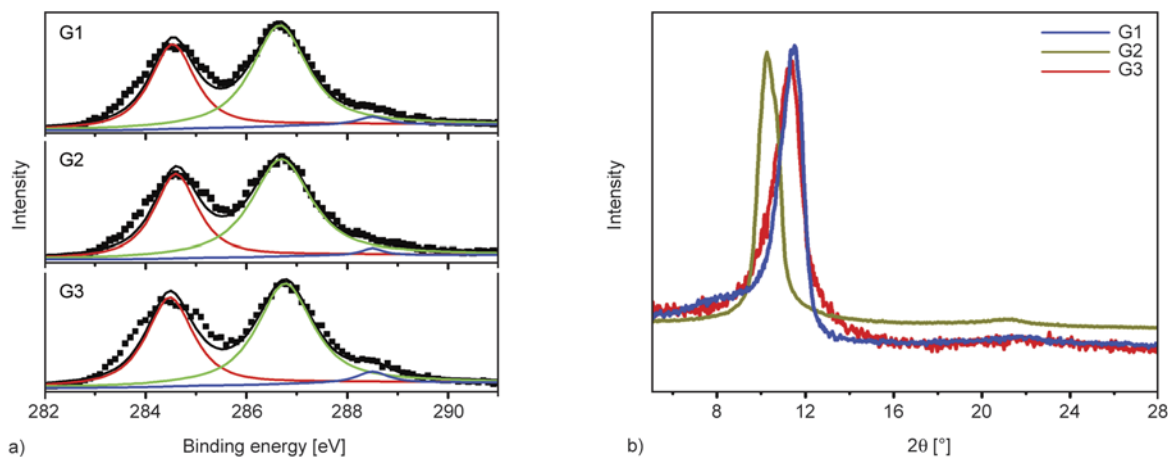


Figure 2. (a) XPS C1s spectra with carbon assignments; (b) XRD patterns of GO sheets of different size

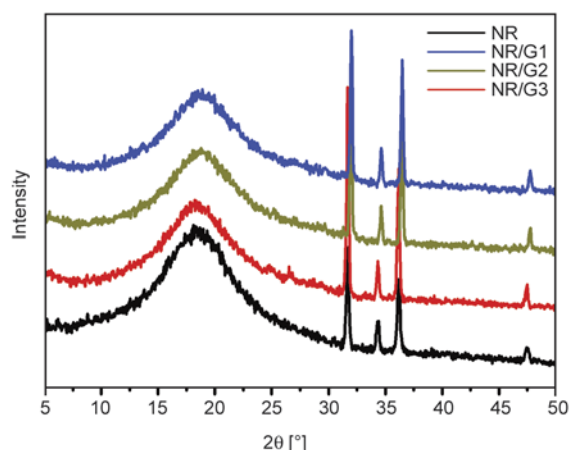


Figure 3. NR/GO nanocomposites with 2 phr GO of different size

All the samples show no obvious characteristic peaks of graphite or GO, indicating that GO sheets are homogeneous dispersed in the polymer matrix and did not show graphite-like ordered structure.

Figure 4 shows the SEM images of the tensile fractured surfaces and TEM images of the NR/GO nanocomposite with 2 phr GO with different size. From the SEM images, it can be seen that GO sheets are well dispersed in the matrix and show no obvious aggregates. The tensile fractured surfaces are rough and no cavities between GO sheets and NR are found. All these indicate strong interfacial interaction between GO and rubber. Furthermore, TEM was used to examine the dispersion of GO in nanocomposites. The dark spots in the pictures are probably the curing agents, since the amount of curing agents are higher than that of GO. Surprisingly, in the TEM images, the GO sheets did not preserve their original length before processing. The lateral sizes of GO sheets in the composites are ranged from dozens to hundreds of nanometers, which are much lower than their original sizes. We measured the size of GO in nanocomposites by carefully inspecting TEM images, this method is developed by Ruoff and coworkers [39, 40]. In the composites, the mean size of G1, G2 and G3 are 92.68, 164.39 and 323.74 nm, respectively. It is speculated that the milling process break down the GO sheets and lowered the average size of GO due to the dynamic shear force. This is well consistent with other studies [41–44]. It is observed that the G3 with large size show thicker sheets in the NR compared with the thickness of smaller GO sheets, which is likely due to restacking of the sheets during the coagulation process [39].

3.3. Effects of GO size on the mechanical properties of NR/GO nanocomposites

Typical stress-strain curves of NR/GO nanocomposites with 2 phr GO having different size are given in Figure 5a. It is evident that the stress of the composites at a given strain is significantly increased with the incorporation of GO and the improvement is more prominent in the composites filled with smaller GO size. Especially, the stress at 300% strain (modulus), which is an important indicator for the practical applications, of the composites with different GO loading and size are summarized in Figure 5b. It can be seen that the moduli of all the samples are increased with the addition of GO, and the moduli of the composites are consistently increased with increasing GO loading. The improvement may be explained by several reasons as follows: 1) GO have outstanding mechanical characteristics and higher specific surface area; 2) the distortions and the resultant defects of GO result in a rough and wrinkled topology on the nanoscale which ensure a strong rubber-to-filler interaction [45]; 3) the interactions between the rubber molecular chains and the GO nanoplatelets can provide additional entanglements or physical crosslinking and GO taking part in the vulcanization reaction can bring chemical crosslinking points according to the tube model [46]; 4) strain-induced crystallization as a substantial feature in mechanical reinforcement of NR specifically at high strain is significantly intensified in the presence of GO layers (as will discussed below) [47].

Comparing the modulus of the composites with different GO size, it is obvious that the GO with smaller size shows higher enhancements in the modulus. For example, with the incorporation of 2 phr G1, G2, and G3, the moduli of the corresponding composites increase by 73, 53, and 36%, respectively, with respect to the unfilled NR. Although it is commonly admitted that the graphene with larger size have higher reinforcement as it favors the stress transfer in the composites [20–22]. In this work, it was found that smaller GO sheets show better reinforcement effect. We proposed that properties of the composites are also related to the filler dispersion and interfacial interaction. Considering that the processing method, graphene and polymer types in our work are distinctly different from others', these contradictions can be understood.

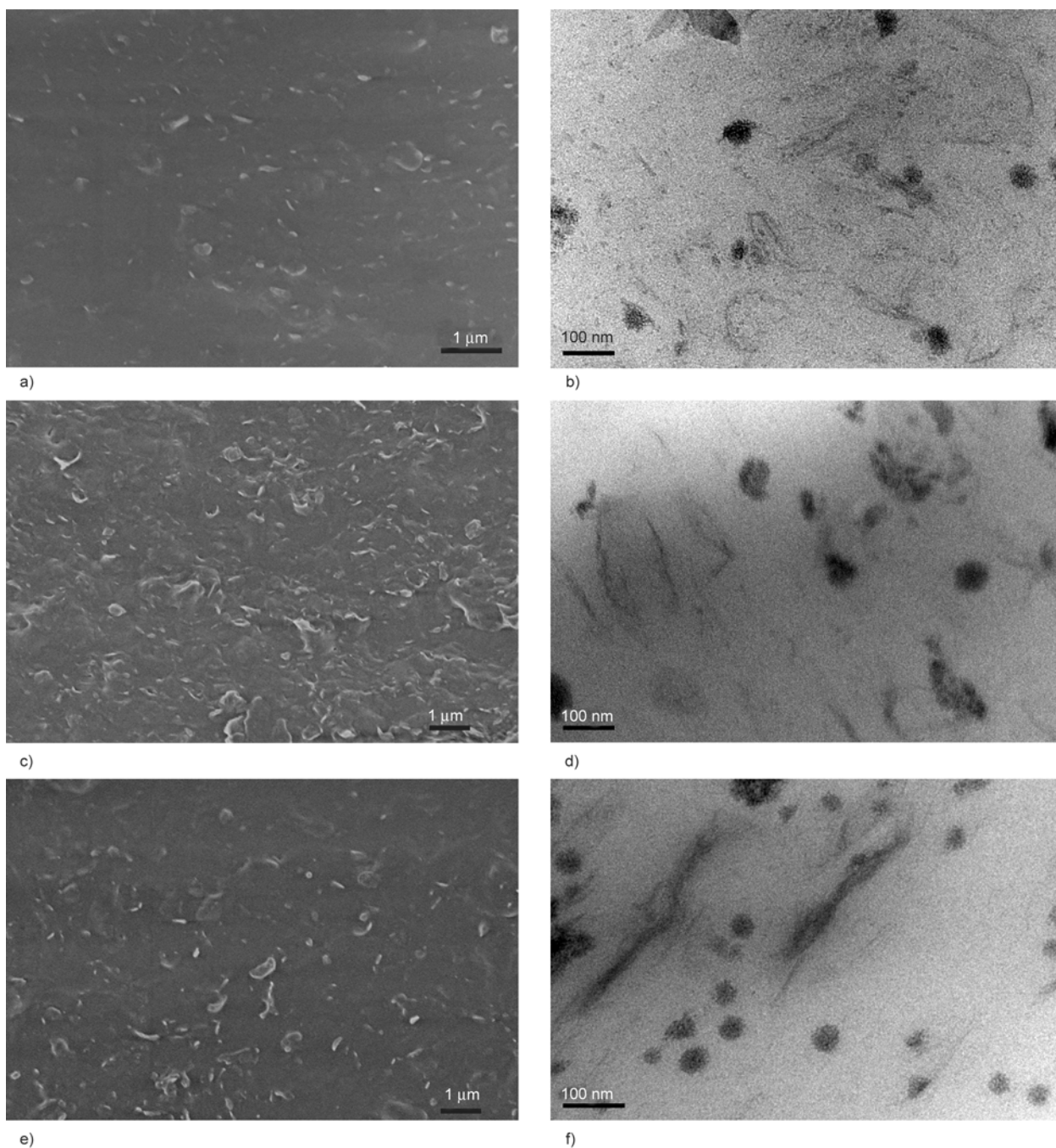


Figure 4. SEM images of the tensile fractured surfaces of (a) NR/G1, (c) NR/G2, (e) NR/G3, and TEM images of (b) NR/G1, (d) NR/G2, (f) NR/G3 nanocomposites with 2 phr GO

It is interesting to find that the elongation at break of NR/GO nanocomposite decreases with decreasing GO size. Previous studies also found that the addition of GO into rubber led to a decrease in the elongation at break of the composites, which is because the movement of the polymer chains is restricted by the interaction between the GO and polymer matrix [16, 48]. Therefore, in our work, it can be understood that GO with smaller size have more number of contacts with NR, which in turn leads to stronger restriction on the rubber chains.

The stress-strain curves are converted into Mooney-Rivlin plots according to Equation (3):

$$\sigma^* = \frac{\sigma}{\lambda - \lambda^{-2}} = 2C_1 + 2C_2\lambda^{-1} \quad (3)$$

where σ is the applied stress, λ is the extension ratio, and C_1 , C_2 are the Mooney–Rivlin (MR) constants related to the network and the flexibility of the network chains, respectively. The plots of reduced stress (σ^*) against the reciprocal of the extension ratio (λ) for NR/GO composites with 2 phr GO are

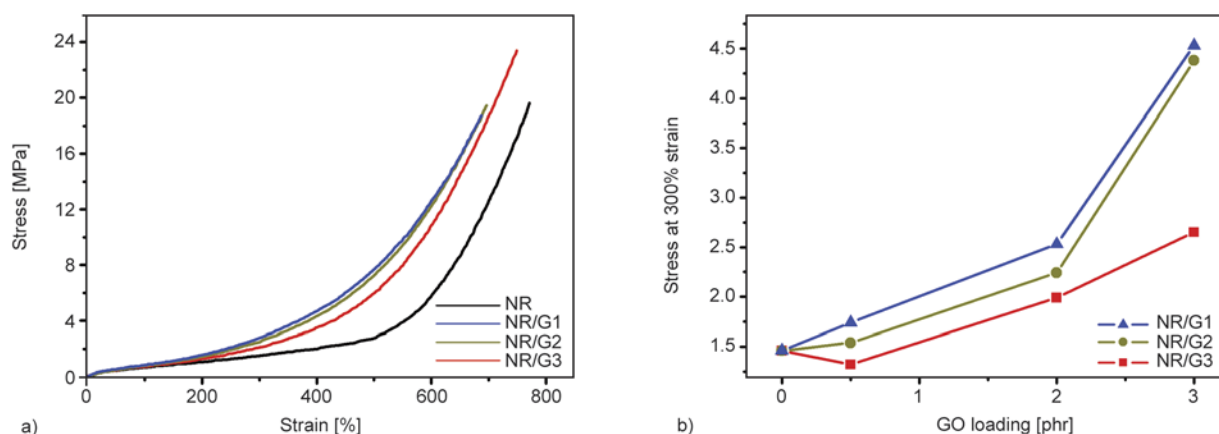


Figure 5. (a) Representative stress-strain curves of NR/GO nanocomposites with 2 phr GO; (b) the effect of GO loading on the stress at 300% strain

shown in Figure 6. It can be found that σ^* of all the samples show a large and abrupt upturn at low λ^{-1} ($\lambda^{-1} < 0.3$). Recent studies attributed the abrupt upturn to the strain-induced crystallization [17] and finite extensibility of the polymer chains [16, 49]. With addition of three types of GO, the abrupt upturn shifts to lower extension ratios. This indicates that

the addition of GO layers facilitates the crystallization of NR during stretching. The abrupt upturn in the curves shifts to lower extension ratio with decreasing the GO size. This means that GO with smaller size is more effective in accelerating the SIC of NR than larger ones, which will be discussed in detail later.

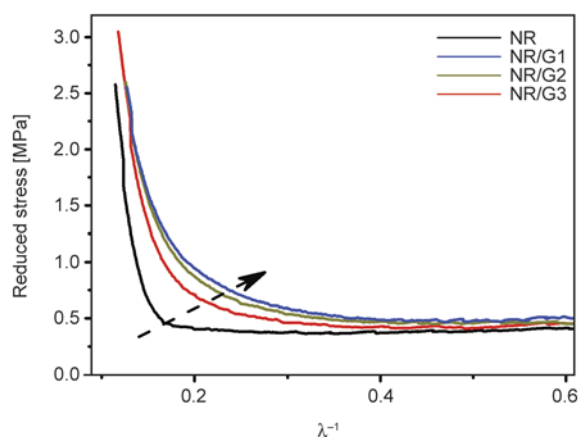


Figure 6. Reduced stress as function of λ^{-1} (Mooney–Rivlin plots) of NR/GO nanocomposites with 2 phr GO

In an attempt to compare the reinforcing efficiency of three types of GO on the performance of the composites, DMA measurements are performed. Figure 7 is the temperature dependence of the storage modulus (E') and loss factor ($\tan\delta$) of the NR/GO composites with 2 phr GO. The dynamic properties reflect the amount of the energy in the composite stored as elastic energy and the amount of energy dissipated during the strain process. These properties are highly dependent on the existence of fillers: dispersion within the matrix, volume fraction, geometrical characteristics, and load transfer from the filler to the matrix [50]. As illustrated in Figure 7a, G1 and G2 give an increase in E' in both the rubbery region and glassy region, G3 only in the

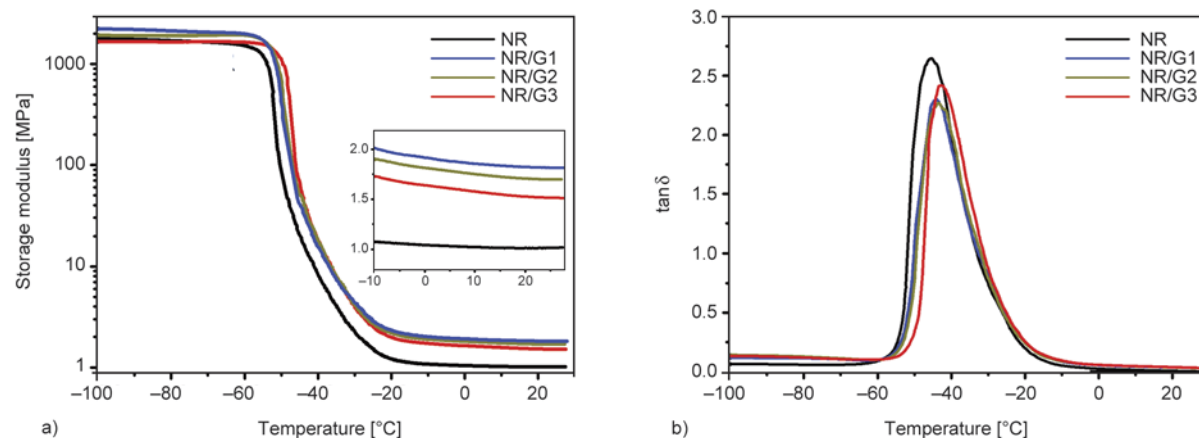


Figure 7. Storage modulus (a) and loss factor (b) versus temperature for NR and NR/GO nanocomposites with 2 phr GO

rubbery region. For instance, at 20°C the storage modulus of the NR and the composites with G1, G2 and G3 are 1.01, 1.82, 1.71 and 1.52 MPa, respectively. In the rubbery region, the storage modulus enhancement is in the order of the NR < NR/G3 < NR/G2 < NR/G1. The reinforcement can be explained by the relative stiffness of the filler and the matrix in rubbery and glassy phases [51, 52]. In the DMA test, the strain was only 1% and do not initiate strain-induced crystallization of NR. The storage modulus of the composite is mainly affected by the stress transfer from rubber to filler, which is in direct correlation with the interfacial interaction between the NR and GO sheets.

As observed from Figure 7b, the glass transition temperature (T_g) of the composites taken at the maximum value of the $\tan\delta$ are -45.5 , -44.2 , -43.5 , -42.4 °C for NR and the composites with G1, G2 and G3, respectively. The glass transition temperature (T_g) of the composites represents the mobility of polymer chains. The adsorption of polymer chains to the rigid particles can slow down the polymer dynamics, which consequently may increase the T_g of the polymer chains in filler-polymer interfaces. However, some published literatures show increases in the T_g of the bulk polymer chains upon the addition of GO or graphene [53, 54], while others report no obvious change in T_g [39, 47, 55] or even decrease in T_g [49]. A very recent study shows that only the covalent attachment of polymer chains onto graphene surface can produce significant restriction on the mobility of the bulk polymer and lead to an increase in the T_g [56]. In our work, the variation of T_g is in a very narrow region of 1–3°C, which may be considered to be essentially the same.

The maximum $\tan\delta$ values of NR decrease with the incorporation of GO. The decrease of $\tan\delta$ peak reflects that GO sheets have effectively immobilized NR chains near the polymer-particle interface due to favorable interfacial interactions with the NR matrix [39, 57]. Meanwhile, the maximum $\tan\delta$ values of the composites with G2 and G1 are lower than that of G3. This result indicates that GO with smaller size have stronger interfacial interaction with rubber. In general, when the GO mixed with rubber, a glassy layer in the vicinity of the GO sheets is formed by adsorbing rubber chains onto the GO surface [58]. Smaller GO sheets are thinner in the rubber matrix, which increases the contact area with rubber.

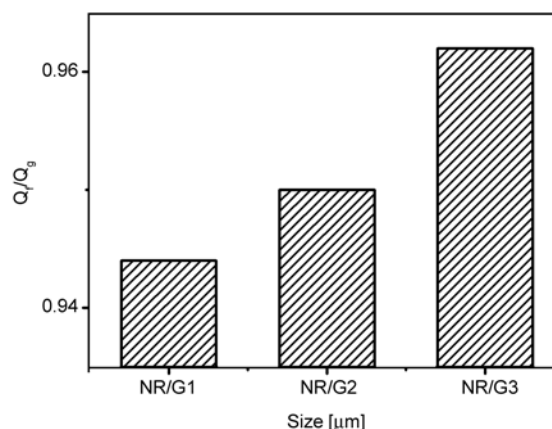


Figure 8. The effect of GO size on filler-rubber interaction of NR/GO composites with 2 phr GO

The effect of the GO size on the rubber-filler interaction in the NR/GO nanocomposites is shown in Figure 8. The value of Q_f/Q_g is increasing with increasing GO size. The lower Q_f/Q_g values mean a higher extent of the interaction between the filler and the rubber matrix. Because of the forming of glassy layer, there were less empty spaces or voids in the matrix, thus less solvent get absorbed and the Q_f/Q_g values would decrease [59]. The composite with G1 gave the lowest Q_f/Q_g value, which indicated strongest filler-rubber interaction.

Figure 9 displays the strain amplitude dependence of storage modulus (G') of NR/GO nanocomposites. Payne effect is mainly related to the breakdown of physical filler networks formed by filler-filler interactions and filler-rubber interactions upon application of oscillatory shear [16]. At low strain range, the applied shear stress is not able to break the network of GO, forming a plateau of nearly constant storage modulus; with further increase in strain

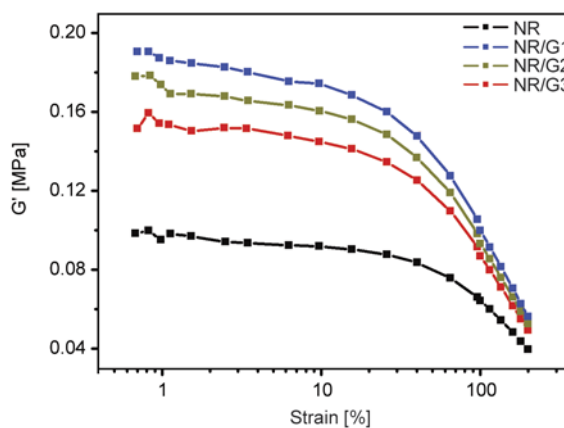


Figure 9. Storage modulus versus strain for NR/GO nanocomposites with 2 phr GO of different size

amplitude the filler-filler interaction destructs, leading to an abrupt decrease of modulus. The Payne effect is denoted by $\Delta G' = G_0 - G_\infty$ (we note G_0 the initial modulus at 0.68% strain and G_∞ the infinite modulus at 200% strain) [60, 61]. The $\Delta G'$ of the NR and the composites with G1, G2 and G3 are 52.35, 133.43, 131.11 and 117.84 KPa, respectively. The highest value of $\Delta G'$ appears in nanocomposite with G1, indicating highest Payne effect. In addition, the G' for NR/GO compounds also increase with the decreasing GO size. The increased G' is attributed to the hydrodynamic effect with the inclusion of rigid filler into the rubber. The NR/GO nanocomposite with G1 shows higher G' , which is due to the fact that the NR chains trapped or caged into the filler network formed glassy layer and can behave as ‘filler’ [61].

3.4. Effects of GO size on strain-induced crystallization of NR

NR can be subjected to crystallize under stretching, which is a unique characteristic for NR. The crys-

tallites act as additional cross-linking points in the network, which account for the obvious enhancements in the mechanical properties of NR. Therefore, it is of great importance to investigate the effect of GO size on the SIC of NR composites. In order to monitor the evolution of strain-induced crystallization, the XRD patterns of NR/GO composites with 2 phr GO at different strains are shown in Figure 10. The crystallinity index (X_c) is estimated according to Equation (4) [62]:

$$X_c = \frac{A_c}{A_c - A_a} \cdot 100\% \quad (4)$$

where A_c and A_a are the areas of crystalline and amorphous regions, respectively. The crystallinity index of NR and its composites with 2 phr GO at different strains are tabulated in Table 2.

The diffraction peaks near $2\theta = 14$ and 21° are assigned to the (200) and (120) plane reflections of NR, respectively. The samples did not show crystal diffraction peaks at the strain of $\alpha = 2$. However, at $\alpha = 3$, two crystalline peaks appear for NR/GO com-

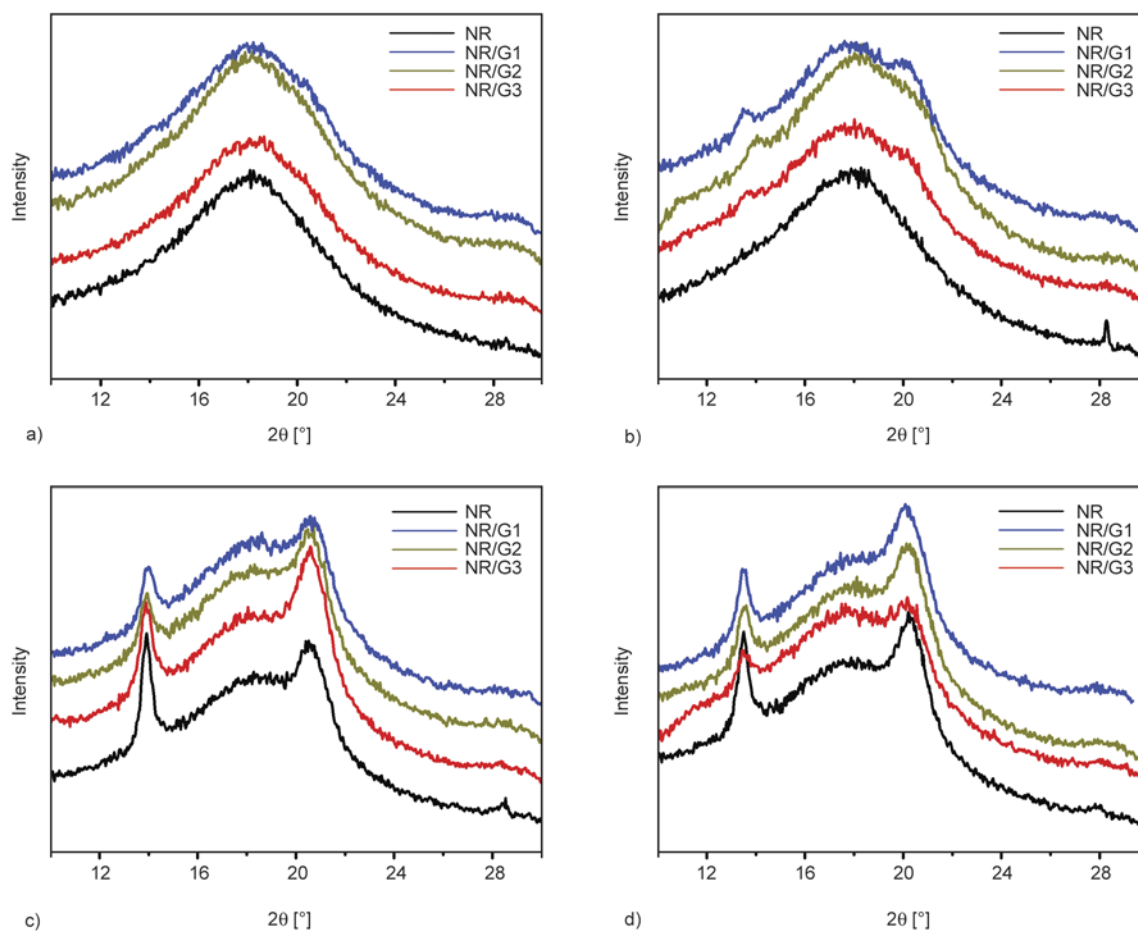


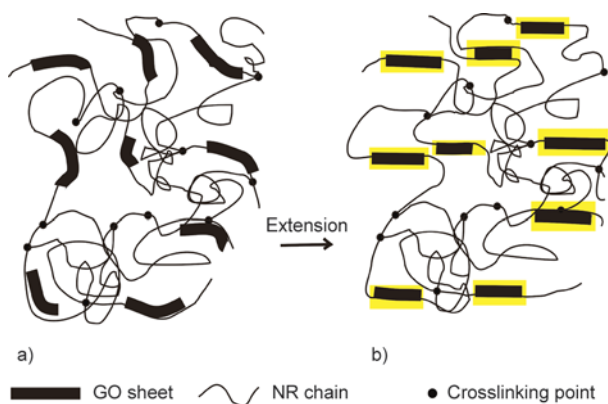
Figure 10. The XRD patterns of NR/GO composites with 2 phr GO at different strains (a) $\alpha = 2$, (b) $\alpha = 3$, (c) $\alpha = 4$, (d) $\alpha = 5$

Table 2. The crystallinity index of NR/GO composites with 2 phr GO at different strains

	$\alpha = 2$ [%]	$\alpha = 3$ [%]	$\alpha = 4$ [%]	$\alpha = 5$ [%]
NR	0	0	21.66	25.10
NR/G1	0	10.41	24.12	24.81
NR/G2	0	7.73	22.36	24.29
NR/G3	0	3.17	24.19	24.84

posites due to strain-induced crystallization, while pure NR still shows an amorphous peak. This implies that the inclusion of GO induces the earlier crystallization of NR, which may be ascribed to the strain amplification effect of the filler [63]. The composite with G1 shows higher crystallinity index than G2, G3 at $\alpha = 3$, revealing that the composite with G1 has a lower onset strain of crystallization. With increasing α to 4, pure NR starts to crystallize and the difference in crystallinity indexes among different samples are diminished. Furthermore, at α of 5, the crystallinity indexes of all samples are close, indicating that GO sheets could not increase the crystallinity index of NR but facilitate SIC at lower strains. This is well consistent with other studies concerning filler filled NR composites [11, 47].

For two-dimensional nanofillers, for example, nanoclay or graphene, they tend to orient and align parallel to the stretching direction at a very low strain ratio [9, 10, 47, 64]. During stretching, the NR chains in the glassy rubber will slip along the GO sheets and form stretching and parallel-arraying straight chain [46]. These early stretched network chains will be acted as crystals nuclei on the basis of the mechanism of crystallization of NR vulcanizate proposed by Tosaka *et al.* [65] and Toki *et al.* [4].

**Figure 11.** Orientation of GO sheets and NR chain duo to extension

Thus, the fact that more polymer chains can be stretched indicates that more nuclei can be formed [66]. As shown in Figure 11, in the initial state most of the GO sheets are dispersed in a random orientation state. Under extension, the NR chains in the glassy layer will slip along the GO sheets at low strain ratio and act as crystals nuclei. In this process, G1 layers having stronger interfacial interaction with NR facilitate alignment and nucleation of NR chains and promote an early onset of the strain-induced crystallization.

4. Conclusions

NR/GO nanocomposites with three different size GO were prepared through latex mixing method. Incorporation of a small amount of the GO sheets into the NR matrix resulted in a significant improvement on the modulus of the polymer. The enhancement of the modulus is strongly dependent on the size of the GO sheets incorporated. The G1 sheets with smaller size give a better reinforcement effect. GO sheets with smaller size have stronger interfacial interaction with NR and promote stress transfer and strain-induced crystallization, both of which lead to the improved modulus.

Acknowledgements

This work was supported by National Natural Science Foundation of China (51222301 and 51333003), the Research Fund for the Doctoral Program of Higher Education of China (20130172110001), Key Technologies R&D Program of Guangzhou City (2013J4300047), and the Fundamental Research Funds for the Central Universities (2014ZG0001).

References

- [1] Vuluga D., Thomassin J.-M., Molenberg I., Huynen I., Gilbert B., Jérôme C., Alexandre M., Detrembleur C.: Straightforward synthesis of conductive graphene/polymer nanocomposites from graphite oxide. *Chemical Communications*, **47**, 2544–2546 (2011). DOI: [10.1039/C0cc04623j](https://doi.org/10.1039/C0cc04623j)
- [2] Kim H., Abdala A. A., Macosko C. W.: Graphene/polymer nanocomposites. *Macromolecules*, **43**, 6515–6530 (2010). DOI: [10.1021/Ma100572e](https://doi.org/10.1021/Ma100572e)
- [3] Liu Q., Liu Z., Zhang X., Yang L., Zhang N., Pan G., Yin S., Chen Y., Wei J.: Polymer photovoltaic cells based on solution-processable graphene and P₃HT. *Advanced Functional Materials*, **19**, 894–904 (2009). DOI: [10.1002/adfm.200800954](https://doi.org/10.1002/adfm.200800954)

- [4] Toki S., Sics I., Ran S., Liu L., Hsiao B. S., Murakami S., Senoo K., Kohjiya S.: New insights into structural development in natural rubber during uniaxial deformation by *in situ* synchrotron X-ray diffraction. *Macromolecules*, **35**, 6578–6584 (2002).
DOI: [10.1021/ma0205921](https://doi.org/10.1021/ma0205921)
- [5] Trabelsi S., Albouy P-A., Rault J.: Crystallization and melting processes in vulcanized stretched natural rubber. *Macromolecules*, **36**, 7624–7639 (2003).
DOI: [10.1021/ma030224c](https://doi.org/10.1021/ma030224c)
- [6] Toki S., Hsiao B. S.: Nature of strain-induced structures in natural and synthetic rubbers under stretching. *Macromolecules*, **36**, 5915–5917 (2003).
DOI: [10.1021/Ma034729e](https://doi.org/10.1021/Ma034729e)
- [7] Bergström J. S., Boyce M. C.: Mechanical behavior of particle filled elastomers. *Rubber Chemistry and Technology*, **72**, 633–656 (1999).
DOI: [10.5254/1.3538823](https://doi.org/10.5254/1.3538823)
- [8] Fukahori Y.: The mechanics and mechanism of the carbon black reinforcement of elastomers. *Rubber Chemistry and Technology*, **76**, 548–566 (2003).
DOI: [10.5254/1.3547760](https://doi.org/10.5254/1.3547760)
- [9] Rezende C. A., Bragança F. C., Doi T. R., Lee L-T., Galembeck F., Boué F.: Natural rubber-clay nanocomposites: Mechanical and structural properties. *Polymer*, **51**, 3644–3652 (2010).
DOI: [10.1016/j.polymer.2010.06.026](https://doi.org/10.1016/j.polymer.2010.06.026)
- [10] Nie Y., Huang G., Qu L., Wang X., Weng G., Wu J.: New insights into thermodynamic description of strain-induced crystallization of peroxide cross-linked natural rubber filled with clay by tube model. *Polymer*, **52**, 3234–3242 (2011).
DOI: [10.1016/j.polymer.2011.05.004](https://doi.org/10.1016/j.polymer.2011.05.004)
- [11] Chenal J-M., Gauthier C., Chazeau L., Guy L., Bomal Y.: Parameters governing strain induced crystallization in filled natural rubber. *Polymer*, **48**, 6893–6901 (2007).
DOI: [10.1016/j.polymer.2007.09.023](https://doi.org/10.1016/j.polymer.2007.09.023)
- [12] Coleman J. N., Khan U., Blau W. J., Gun'ko Y. K.: Small but strong: A review of the mechanical properties of carbon nanotube-polymer composites. *Carbon*, **44**, 1624–1652 (2006).
DOI: [10.1016/j.carbon.2006.02.038](https://doi.org/10.1016/j.carbon.2006.02.038)
- [13] Zhu Y., Murali S., Cai W., Li X., Suk J. W., Potts J. R., Ruoff R. S.: Correction: Graphene and graphene oxide: Synthesis, properties, and applications. *Advanced Materials*, **22**, 5226 (2010).
DOI: [10.1002/adma.201090156](https://doi.org/10.1002/adma.201090156)
- [14] Dikin D. A., Stankovich S., Zimney E. J., Piner R. D., Dommett G. H. B., Evmenenko G., Nguyen S. T., Ruoff R. S.: Preparation and characterization of graphene oxide paper. *Nature*, **448**, 457–460 (2007).
DOI: [10.1038/Nature06016](https://doi.org/10.1038/Nature06016)
- [15] Bai X., Wan C., Zhang Y., Zhai Y.: Reinforcement of hydrogenated carboxylated nitrile-butadiene rubber with exfoliated graphene oxide. *Carbon*, **49**, 1608–1613 (2011).
DOI: [10.1016/j.carbon.2010.12.043](https://doi.org/10.1016/j.carbon.2010.12.043)
- [16] Kang H., Zuo K., Wang Z., Zhang L., Liu L., Guo B.: Using a green method to develop graphene oxide/elastomers nanocomposites with combination of high barrier and mechanical performance. *Composites Science and Technology*, **92**, 1–8 (2014).
DOI: [10.1016/j.compscitech.2013.12.004](https://doi.org/10.1016/j.compscitech.2013.12.004)
- [17] Moghaddam S. Z., Sabury S., Sharif F.: Dispersion of rGO in polymeric matrices by thermodynamically favorable self-assembly of GO at oil-water interfaces. *RSC Advances*, **4**, 8711–8719 (2014).
DOI: [10.1039/c3ra46342g](https://doi.org/10.1039/c3ra46342g)
- [18] Mao Y., Zhang S., Zhang D., Chan T. W., Liu L.: Enhancing graphene oxide reinforcing potential in composites by combined latex compounding and spray drying. *Materials Research Express*, **1**, 025009/1–025009/13 (2014).
DOI: [10.1088/2053-1591/1/2/025009](https://doi.org/10.1088/2053-1591/1/2/025009)
- [19] Wang Z., Liu J., Wu S., Wang W., Zhang L.: Novel percolation phenomena and mechanism of strengthening elastomers by nanofillers. *Physical Chemistry Chemical Physics*, **12**, 3014–3030 (2010).
DOI: [10.1039/b919789c](https://doi.org/10.1039/b919789c)
- [20] Khan U., May P., O'Neill A., Coleman J. N.: Development of stiff, strong, yet tough composites by the addition of solvent exfoliated graphene to polyurethane. *Carbon*, **48**, 4035–4041 (2010).
DOI: [10.1016/j.carbon.2010.07.008](https://doi.org/10.1016/j.carbon.2010.07.008)
- [21] Choi J. T., Kim D. H., Ryu K. S., Lee H-I., Jeong H. M., Shin C. M., Kim J. H., Kim B. K.: Functionalized graphene sheet/polyurethane nanocomposites: Effect of particle size on physical properties. *Macromolecular Research*, **19**, 809–814 (2011).
DOI: [10.1007/s13233-011-0801-4](https://doi.org/10.1007/s13233-011-0801-4)
- [22] Chatterjee S., Nafezarefi F., Tai N. H., Schlagenhaut L., Nüesch F. A., Chu B. T. T.: Size and synergy effects of nanofiller hybrids including graphene nanoplatelets and carbon nanotubes in mechanical properties of epoxy composites. *Carbon*, **50**, 5380–5386 (2012).
DOI: [10.1016/j.carbon.2012.07.021](https://doi.org/10.1016/j.carbon.2012.07.021)
- [23] Wang X., Jin J., Song M.: An investigation of the mechanism of graphene toughening epoxy. *Carbon*, **65**, 324–333 (2013).
DOI: [10.1016/j.carbon.2013.08.032](https://doi.org/10.1016/j.carbon.2013.08.032)
- [24] Gojny F. H., Wichmann M. H. G., Fiedler B., Schulte K.: Influence of different carbon nanotubes on the mechanical properties of epoxy matrix composites – A comparative study. *Composites Science and Technology*, **65**, 2300–2313 (2005).
DOI: [10.1016/j.compscitech.2005.04.021](https://doi.org/10.1016/j.compscitech.2005.04.021)
- [25] Song Y. S., Youn J. R.: Influence of dispersion states of carbon nanotubes on physical properties of epoxy nanocomposites. *Carbon*, **43**, 1378–1385 (2005).
DOI: [10.1016/j.carbon.2005.01.007](https://doi.org/10.1016/j.carbon.2005.01.007)
- [26] Fu S-Y., Feng X-Q., Lauke B., Mai Y-W.: Effects of particle size, particle/matrix interface adhesion and particle loading on mechanical properties of particulate-polymer composites. *Composites Part B: Engineering*, **39**, 933–961 (2008).
DOI: [10.1016/j.compositesb.2008.01.002](https://doi.org/10.1016/j.compositesb.2008.01.002)

- [27] Prolongo S. G., Jiménez-Suárez A., Moriche R., Ureña A.: Graphene nanoplatelets thickness and lateral size influence on the morphology and behavior of epoxy composites. *European Polymer Journal*, **53**, 292–301 (2014).
DOI: [10.1016/j.eurpolymj.2014.01.019](https://doi.org/10.1016/j.eurpolymj.2014.01.019)
- [28] Tang Z., Zeng C., Lei Y., Guo B., Zhang L., Jia D.: Fluorescent whitening agent stabilized graphene and its composites with chitosan. *Journal of Materials Chemistry*, **21**, 17111–17118 (2011).
DOI: [10.1039/C1jm13239c](https://doi.org/10.1039/C1jm13239c)
- [29] Lorenz O., Parks C. R.: The crosslinking efficiency of some vulcanizing agents in natural rubber. *Journal of Polymer Science*, **50**, 299–312 (1961).
DOI: [10.1002/pol.1961.1205015404](https://doi.org/10.1002/pol.1961.1205015404)
- [30] Zhang L., Liang J., Huang Y., Ma Y., Wang Y., Chen Y.: Size-controlled synthesis of graphene oxide sheets on a large scale using chemical exfoliation. *Carbon*, **47**, 3365–3368 (2009).
DOI: [10.1016/j.carbon.2009.07.045](https://doi.org/10.1016/j.carbon.2009.07.045)
- [31] Khan U., O’Neill A., Porwal H., May P., Nawaz K., Coleman J. N.: Size selection of dispersed, exfoliated graphene flakes by controlled centrifugation. *Carbon*, **50**, 470–475 (2012).
DOI: [10.1016/j.carbon.2011.09.001](https://doi.org/10.1016/j.carbon.2011.09.001)
- [32] Wang X., Bai H., Shi G.: Size fractionation of graphene oxide sheets by pH-assisted selective sedimentation. *Journal of the American Chemical Society*, **133**, 6338–6342 (2011).
DOI: [10.1021/ja200218y](https://doi.org/10.1021/ja200218y)
- [33] Pan S., Aksay I. A.: Factors controlling the size of graphene oxide sheets produced *via* the graphite oxide route. *ACS Nano*, **5**, 4073–4083 (2011).
DOI: [10.1021/nn200666r](https://doi.org/10.1021/nn200666r)
- [34] Zhou X., Liu Z.: A scalable, solution-phase processing route to graphene oxide and graphene ultralarge sheets. *Chemical Communications*, **46**, 2611–2613 (2010).
DOI: [10.1039/b914412a](https://doi.org/10.1039/b914412a)
- [35] Zhao J., Pei S., Ren W., Gao L., Cheng H-M.: Efficient preparation of large-area graphene oxide sheets for transparent conductive films. *ACS Nano*, **4**, 5245–5252 (2010).
DOI: [10.1021/nn1015506](https://doi.org/10.1021/nn1015506)
- [36] Aboutalebi S. H., Gudarzi M. M., Zheng Q. B., Kim J-K.: Spontaneous formation of liquid crystals in ultralarge graphene oxide dispersions. *Advanced Functional Materials*, **21**, 2978–2988 (2011).
DOI: [10.1002/adfm.201100448](https://doi.org/10.1002/adfm.201100448)
- [37] Lin X., Shen X., Zheng Q., Yousefi N., Ye L., Mai Y-W., Kim J-K.: Fabrication of highly-aligned, conductive, and strong graphene papers using ultralarge graphene oxide sheets. *ACS Nano*, **6**, 10708–10719 (2012).
DOI: [10.1021/nn303904z](https://doi.org/10.1021/nn303904z)
- [38] Premanathan M., Karthikeyan K., Jeyasubramanian K., Manivannan G.: Selective toxicity of ZnO nanoparticles toward Gram-positive bacteria and cancer cells by apoptosis through lipid peroxidation. *Nanomedicine: Nanotechnology, Biology and Medicine*, **7**, 184–192 (2011).
DOI: [10.1016/j.nano.2010.10.001](https://doi.org/10.1016/j.nano.2010.10.001)
- [39] Potts J. R., Shankar O., Du L., Ruoff R. S.: Processing–morphology–property relationships and composite theory analysis of reduced graphene oxide/natural rubber nanocomposites. *Macromolecules*, **45**, 6045–6055 (2012).
DOI: [10.1021/ma300706k](https://doi.org/10.1021/ma300706k)
- [40] Potts J. R., Shankar O., Murali S., Du L., Ruoff R. S.: Latex and two-roll mill processing of thermally-exfoliated graphite oxide/natural rubber nanocomposites. *Composites Science and Technology*, **74**, 166–172 (2013).
DOI: [10.1016/j.compscitech.2012.11.008](https://doi.org/10.1016/j.compscitech.2012.11.008)
- [41] Chen L., Pang X-J., Zhang Q-T., Yu Z-L.: Cutting of carbon nanotubes by a two-roller mill. *Materials Letters*, **60**, 241–244 (2006).
DOI: [10.1016/j.matlet.2005.08.024](https://doi.org/10.1016/j.matlet.2005.08.024)
- [42] Yue D., Liu Y., Shen Z., Zhang L.: Study on preparation and properties of carbon nanotubes/rubber composites. *Journal of Materials Science*, **41**, 2541–2544 (2006).
DOI: [10.1007/s10853-006-5331-7](https://doi.org/10.1007/s10853-006-5331-7)
- [43] Krause B., Boldt R., Pötschke P.: A method for determination of length distributions of multiwalled carbon nanotubes before and after melt processing. *Carbon*, **49**, 1243–1247 (2011).
DOI: [10.1016/j.carbon.2010.11.042](https://doi.org/10.1016/j.carbon.2010.11.042)
- [44] Fu S-Y., Chen Z-K., Hong S., Han C. C.: The reduction of carbon nanotube (CNT) length during the manufacture of CNT/polymer composites and a method to simultaneously determine the resulting CNT and interfacial strengths. *Carbon*, **47**, 3192–3200 (2009).
DOI: [10.1016/j.carbon.2009.07.028](https://doi.org/10.1016/j.carbon.2009.07.028)
- [45] Hernández M., del Mar Bernal M., Verdejo R., Ezquerro T. A., López-Manchado M. A.: Overall performance of natural rubber/graphene nanocomposites. *Composites Science and Technology*, **73**, 40–46 (2012).
DOI: [10.1016/j.compscitech.2012.08.012](https://doi.org/10.1016/j.compscitech.2012.08.012)
- [46] Xing W., Wu J., Huang G., Li H., Tang M., Fu X.: Enhanced mechanical properties of graphene/natural rubber nanocomposites at low content. *Polymer International*, **63**, 1674–1681 (2014).
DOI: [10.1002/pi.4689](https://doi.org/10.1002/pi.4689)
- [47] Ozbas B., Toki S., Hsiao B. S., Chu B., Register R. A., Aksay I. A., Prud’homme R. K., Adamson D. H.: Strain-induced crystallization and mechanical properties of functionalized graphene sheet-filled natural rubber. *Journal of Polymer Science Part B: Polymer Physics*, **50**, 718–723 (2012).
DOI: [10.1002/polb.23060](https://doi.org/10.1002/polb.23060)

- [48] Wang J., Jia H., Tang Y., Ji D., Sun Y., Gong X., Ding L.: Enhancements of the mechanical properties and thermal conductivity of carboxylated acrylonitrile butadiene rubber with the addition of graphene oxide. *Journal of Materials Science*, **48**, 1571–1577 (2012). DOI: [10.1007/s10853-012-6913-1](https://doi.org/10.1007/s10853-012-6913-1)
- [49] Tang Z., Wu X., Guo B., Zhang L., Jia D.: Preparation of butadiene–styrene–vinyl pyridine rubber–graphene oxide hybrids through *co*-coagulation process and *in situ* interface tailoring. *Journal of Materials Chemistry*, **22**, 7492–7501 (2012). DOI: [10.1039/c2jm00084a](https://doi.org/10.1039/c2jm00084a)
- [50] Zhao Y., Barrera E. V.: Asymmetric diamino functionalization of nanotubes assisted by BOC protection and their epoxy nanocomposites. *Advanced Functional Materials*, **20**, 3039–3044 (2010). DOI: [10.1002/adfm.201000942](https://doi.org/10.1002/adfm.201000942)
- [51] Affdl J. C. H., Kardos J. L.: The Halpin-Tsai equations: A review. *Polymer Engineering and Science*, **16**, 344–352 (1976). DOI: [10.1002/pen.760160512](https://doi.org/10.1002/pen.760160512)
- [52] Mori T., Tanaka K.: Average stress in matrix and average elastic energy of materials with misfitting inclusions. *Acta Metallurgica*, **21**, 571–574 (1973). DOI: [10.1016/0001-6160\(73\)90064-3](https://doi.org/10.1016/0001-6160(73)90064-3)
- [53] Potts J. R., Lee S. H., Alam T. M., An J., Stoller M. D., Piner R. D., Ruoff R. S.: Thermomechanical properties of chemically modified graphene/poly(methyl methacrylate) composites made by *in situ* polymerization. *Carbon*, **49**, 2615–2623 (2011). DOI: [10.1016/j.carbon.2011.02.023](https://doi.org/10.1016/j.carbon.2011.02.023)
- [54] Ramanathan T., Abdala A. A., Stankovich S., Dikin D. A., Herrera-Alonso M., Piner R. D., Adamson D. H., Schniepp H. C., Chen X., Ruoff R. S., Nguyen S. T., Aksay I. A., Prud'homme R. K., Brinson L. C.: Functionalized graphene sheets for polymer nanocomposites. *Nature Nanotechnology*, **3**, 327–331 (2008). DOI: [10.1038/nnano.2008.96](https://doi.org/10.1038/nnano.2008.96)
- [55] Zhan Y., Wu J., Xia H., Yan N., Fei G., Yuan G.: Dispersion and exfoliation of graphene in rubber by an ultrasonically-assisted latex mixing and *in situ* reduction process. *Macromolecular Materials and Engineering*, **296**, 590–602 (2011). DOI: [10.1002/mame.201000358](https://doi.org/10.1002/mame.201000358)
- [56] Liao K-H., Aoyama S., Abdala A. A., Macosko C.: Does graphene change T_g of nanocomposites? *Macromolecules*, **47**, 8311–8319 (2014). DOI: [10.1021/Ma501799z](https://doi.org/10.1021/Ma501799z)
- [57] Tang Z., Zhang L., Feng W., Guo B., Liu F., Jia D.: Rational design of graphene surface chemistry for high-performance rubber/graphene composites. *Macromolecules*, **47**, 8663–8673 (2014). DOI: [10.1021/ma502201e](https://doi.org/10.1021/ma502201e)
- [58] Vo L. T., Anastasiadis S. H., Giannelis E. P.: Dielectric study of poly(styrene-*co*-butadiene) composites with carbon black, silica, and nanoclay. *Macromolecules*, **44**, 6162–6171 (2011). DOI: [10.1021/ma200044c](https://doi.org/10.1021/ma200044c)
- [59] Somaratne M. C. W., Liyanage N. M. V. K., Walpalage S.: Contribution of hydrogen and/or covalent bonds on reinforcement of natural rubber latex films with surface modified silica. *Journal of Applied Polymer Science*, **131**, 40380/1–40380/9 (2014). DOI: [10.1002/app.40380](https://doi.org/10.1002/app.40380)
- [60] Ramier J., Gauthier C., Chazeau L., Stelandre L., Guy L.: Payne effect in silica-filled styrene–butadiene rubber: Influence of surface treatment. *Journal of Polymer Science Part B: Polymer Physics*, **45**, 286–298 (2007). DOI: [10.1002/polb.21033](https://doi.org/10.1002/polb.21033)
- [61] Fröhlich J., Niedermeier W., Luginsland H-D.: The effect of filler–filler and filler–elastomer interaction on rubber reinforcement. *Composites Part A: Applied Science and Manufacturing*, **36**, 449–460 (2005). DOI: [10.1016/j.compositesa.2004.10.004](https://doi.org/10.1016/j.compositesa.2004.10.004)
- [62] Che J., Burger C., Toki S., Rong L., Hsiao B. S., Amnuaypornsi S., Sakdapipanich J.: Crystal and crystallites structure of natural rubber and peroxide-vulcanized natural rubber by a two-dimensional wide-angle X-ray diffraction simulation method. II. Strain-induced crystallization versus temperature-induced crystallization. *Macromolecules*, **46**, 9712–9721 (2013). DOI: [10.1021/ma401812s](https://doi.org/10.1021/ma401812s)
- [63] Poompradub S., Tosaka M., Kohjiya S., Ikeda Y., Toki S., Sics I., Hsiao B. S.: Mechanism of strain-induced crystallization in filled and unfilled natural rubber vulcanizates. *Journal of Applied Physics*, **97**, 103529/1–103529/9 (2005). DOI: [10.1063/1.1900927](https://doi.org/10.1063/1.1900927)
- [64] Hernández M., Sanz A., Nogales A., Ezquerro T. A., López-Manchado M. A.: Structure and segmental dynamics relationship in natural rubber/layered silicate nanocomposites during uniaxial deformation. *Macromolecules*, **46**, 3176–3182 (2013). DOI: [10.1021/ma4002353](https://doi.org/10.1021/ma4002353)
- [65] Toki S., Sics I., Ran S. F., Liu L. Z., Hsiao B. S., Murakami S., Tosaka M., Kohjiya S., Poompradub S., Ikeda Y., Tsou A. H.: Strain-induced molecular orientation and crystallization in natural and synthetic rubbers under uniaxial deformation by in-situ synchrotron X-ray study. *Rubber Chemistry and Technology*, **77**, 317–335 (2004). DOI: [10.5254/1.3547826](https://doi.org/10.5254/1.3547826)
- [66] Qu L., Huang G., Liu Z., Zhang P., Weng G., Nie Y.: Remarkable reinforcement of natural rubber by deformation-induced crystallization in the presence of organophilic montmorillonite. *Acta Materialia*, **57**, 5053–5060 (2009). DOI: [10.1016/j.actamat.2009.07.007](https://doi.org/10.1016/j.actamat.2009.07.007)

Facilitating protein denaturation in organic solvent and the contribution to the promoting dispersion of graphite nanoplatelets in a polymer

T. Liu, Y. Wang, A. Eyley, Y. C. Chang, W. H. Zhong*

School of Mechanical and Materials Engineering Washington State University, WA 99164 Pullman, USA

Received 9 January 2015; accepted in revised form 19 February 2015

Abstract. Denatured proteins, natural macromolecules are very attractive for advanced nanocomposites owing to their multiple functional chemical groups. However, denaturation processes were only successfully conducted in an aqueous environment, limiting their broad applications in hydrophobic polymers. In this study, we report an effective approach of denaturing soy protein at nanoscale in an organic solvent. Further, the denatured soy protein was found to be able to infiltrate between the graphite nanoplatelet (GNP) layers to reduce the thickness of GNPs and improve the dispersion of the nanoparticles in either the suspension or the final polymeric nanocomposites. As a result, remarkable improvements in transparency and electrical conductivity have been achieved for the nanocomposites with the GNPs treated by the denatured soy protein.

Keywords: nanocomposites, soy protein, denaturation, biotreatment of nanofillers, organic solvent

1. Introduction

It is well known that, to create high-performance polymeric nanocomposites, dispersion of the nanofillers in the polymer matrix, and interfacial interactions between nanofillers and matrix are the two critical factors. Meanwhile, carbon nanofillers, including nanofibers (CNF), nanotubes (CNT), and graphitic nanoplatelets (GNP) are the most popular nanofillers employed to make polymeric nanocomposites [1, 2]. In order to improve the dispersion and interfacial interactions, numerous chemical approaches to the surface modification for carbon nanofillers have been intensely studied [3–8]. It is noted that chemical approaches are often performed via complicated processing procedures, even involving toxic chemicals.

Compared with the various chemical methods, biotreatment provides a more significant avenue to the

treatment of nanofillers in an environmentally friendly, simple and effective way. For the biotreatments such biomolecules as polysaccharides [9], albumin [10], enzymes [11], and deoxyribonucleic acid (DNA) [12], can be either covalently or non-covalently performed for the nanofillers. Proteins are full of polar groups such as amino acids constructing the polypeptide causing a variety of interactions and have been of great interest for making polymeric composites [13]. However, another significant application of them that has not been paid adequate attention is that they can be used as a ‘green’ functional agent to treat nanoparticles for effectively improving dispersion of nanoparticles thus improving the properties of the nanocomposites based on their various functional groups in protein structures. Strategies for harnessing these unique structures and functional groups are attractive for

*Corresponding author, e-mail: katie_zhong@wsu.edu
© BME-PT

fabrication of high-performance nanocomposites [14, 15].

Recently, soy protein, an abundant plant protein, showed great potential for application into biological functionalization of nanofillers [16–21]. The availability of various groups (such as amines, hydroxyls, etc.) along the soy protein molecules provides possibilities for modification of nanofillers via strong interactions, such as hydrogen bonding or even chemical bonding [18]. However, it should be pointed out that pristine soy proteins exist as big particles (around 30 μm [13]) united by strong internal interactions and cannot be directly used for the biotreatment. An effective way to break the native interactions and disentangle the soy protein structures for biotreatment is to effectively denature the pristine soy protein. To this end, aqueous solution with salts is usually used. At the same time, the polymer matrix for the composite has to be water-soluble in order to homogeneously mix the bio-treated nanofillers and the polymer solution. However, most of the polymers cannot be dissolved by aqueous solvents, which indicates that the biotreatment of nanofillers by denatured soy protein for polymeric nanocomposites can't be realized in aqueous systems. Thus far, biotreatment of nanofillers in non-aqueous environment, that is, in organic solvent, which has not been reported, will be critical for soy protein to be used to develop various nanocomposites for wide applications.

In this study, for the first time, we report a method that leads the pristine soy protein isolate (SPI) to be effectively denatured in a non-aqueous environment via the help of a denaturing agent, cetyl alcohol (CA). The biotreatment of nanofillers (GNP, for example) through use of the denatured SPI was also carried out in organic solvent, chloroform. The effects of the biotreatment on exfoliation and dispersion of graphite were characterized via confocal microscope and field emission scanning electron microscopy. The optical transmittance and electrical properties of the resulting polymeric nanocomposites were investigated through UV-visible spectrophotometer and Dielectric Analyzer, respectively. The results indicate that the denatured SPI can remarkably improve the GNP exfoliation and dispersion in the final nanocomposites. Compared with the sample without the biotreatment, the optical transmittance of the resulting nanocomposites with 1 wt%

of GNPs is increased by 3.2 times, and the electrical conductivity increases by 11 orders of magnitude (at 10^{-2} Hz).

2. Experimental section

2.1. Materials

Granule-shaped polycarbonate (PC, Lexan 101) as the matrix used in this study was kindly provided by SABIC Innovation Plastics Company, MA, USA. The graphitic nanoplatelets (GNPs) obtained from XG Science Inc., MI, USA, were pre-exfoliated with an average diameter of $\sim 5 \mu\text{m}$ and $\sim 5 \text{nm}$ in thickness. Soy protein isolate (SPI) was donated by ADM Co., IL, USA, and contained 4.8% moisture and 90.9% dry basis protein. Chloroform, obtained from Fisher Scientific, PA, USA, was used as the solvent for both PC and GNPs surface modification with SPI. Cetyl alcohol (1-Hexadecanol, 98%) as SPI denaturing agent was purchased from Alfa Aesar, MA, USA.

2.2. Preparation of nanocomposite films

The bio-modification of GNPs was accomplished by dispersing pristine GNPs (0.02 g) and SPI (0.02 g) in equal amounts in chloroform (5 mL) via 15 min high power probe ultrasonication (Branson 450). In order to assist SPI denaturation in chloroform, 0.05 M of cetyl alcohol (CA) was applied as surfactant. The mixture was then heated with oil-bath at 65°C for 4 h. The preparation procedure for the composite membranes starts by completely dissolving PC (2 g) in chloroform (10 mL) via spin mixing. Simultaneously, the pristine GNPs or SPI-treated GNPs with and without CA were mixed with PC-chloroform solution using room temperature bath-sonication for 10 min to obtain homogenous suspension. Finally, an aluminum mold was used to cast the composite solution on glass substrate. The thickness of all films was 0.04 mm. After completely evaporating the solvent, the composite film was taken off and dried at 50°C overnight to remove any moisture. Table 1 presents the descriptions of each composite film prepared in this study.

Table 1. Detailed description for each nanocomposite

Composite	Reinforcement	SPI denaturation agent
PC/GNP	Pristine GNPs	–
PC/GNP-CA	Pristine GNPs	–
PC/s-GNP	SPI treated GNPs	–
PC/s-GNP-CA	SPI treated GNPs	Cetyl alcohol

2.3. Characterizations

Confocal images were acquired using a ZEISS confocal microscope. The 488 nm line from an argon laser was used for excitation, and fluorescence emission was detected using a 510 nm band-pass filter. Images were recorded using a water immersion objective. Optical micrographs, imaged by Olympus BX51, were obtained of thin composite films. Field emission scanning electron microscopy (FESEM) images were taken using a FEI Quanta 200F. Both GNP particles and fracture surface of the composites was prepared to take SEM images. All composite samples were frozen in liquid nitrogen for 5 min prior to fracturing, and then sputter-coated with gold for electrical conductivity. Alternating current (AC) conductivity was obtained at ambient conditions using a Novocontrol Technologies Alpha-N high resolution Dielectric Analyzer. The sample thickness of the five nanocomposites (Table 1) was prepared for AC conductivity testing, which is ca. 200 μm . The difference in transparency of the nanocomposite film was described via UV-vis spectroscopy. The UV-visible spectrum was recorded on a Nicolet Evolution 300 UV-visible spectrophotometer (Thermo Fisher Scientific Inc., USA) using a quartz cell in the wavelength range of 200–700 nm.

3. Results and discussion

Denaturation of SPI is the first step for the biotreatment. The study on the realization of the denaturation of SPI in organic solvent is very rare. As one of the results from denaturation, the SPI particle size will change a lot after the denaturation. Since SPI can show green fluorescence under the illuminating light (excitation wavelength: 488 nm; emission wavelength: 510–530 nm), one can identify the change in particle size by confocal images obtained from confocal microscope. Figure 1a and 1b are the confocal images of the SPI particles after thermal treatment in chloroform without and with the addition of denaturing agent, cetyl alcohol (CA), respectively. By comparing the confocal images, one can find that the addition of CA can remarkably reduce the size of SPI, indicating that the SPI particles were well-denatured via the help of CA. At the same time, the distinct difference in particle size between poorly denatured and well-denatured SPI is further demonstrated by the laser scattering results as shown by the inserts in Figure 1a and 1b. Clearly, the well-denatured SPI with CA gives rise to a much more trans-

parent solution as compared with the poorly denatured SPI without the addition of CA. In addition to the above results in the solvent, the solid SPI particles were also characterized by SEM images. As shown in Figure 1c up and down, there is a big difference in the particle size for the poorly denatured (up) and well-denatured SPI particles (down). For the well-denatured protein, the SPI particles become nanoparticles (ca. 70 nm); while, the other one almost remains the same size as the pristine SPI (ca. 30 μm). Besides, Circular Dichroism (CD) technique was also applied to characterize the change in protein structures for the two samples. Ellipticity, defined as a differential absorbance between right-hand-polarized and left-hand-polarized light through a protein, is a common parameter to characterize the protein structures. For the structure analysis of protein, the wavelength of 190–250 nm can provide the information of secondary structures, including α -helix, β -sheet, and random coil. In comparison of the ellipticity at 220 nm in Figure 1d, which corresponds to an α -helical secondary structure, the lower ellipticity of the denatured SPI solution (green) indicates that the well-denatured SPI possesses unfolded and more randomized structures.

Since proteins are famous for their abundance in functional groups and structures, the denatured SPI with open structures should be promising for biotreatment of nanoparticles, such as GNPs. Figure 2 shows the FESEM and TEM images of the GNP samples treated by SPI with the two different denaturation states as described above. For the GNP sample treated by poorly denatured SPI (called as *s*-GNP), no notable interaction was detected by the SEM images as shown in Figure 2a and 2b. At the same time, lots of un-denatured SPI particles can be found as indicated in Figure 2a. Further, the bare surface of the GNP sheet (Figure 2b) and numerous graphene sheets overlapped together (insert in Figure 2b) indicate that the poorly denatured SPI cannot give rise to meaningful interaction with other nanoparticles. Additionally, the *s*-GNP suspension in chloroform was found to be precipitated in a few hours, as shown in the insert in Figure 2a. In comparison, significant interaction between the well-denatured SPI and GNP was confirmed. Firstly, it was difficult to find big protein particles in the GNP sample treated by the well-denatured SPI (called as *s*-GNP-CA) as shown in Figure 2c. Also, it was found that the denatured SPI nanoparticles can coat the

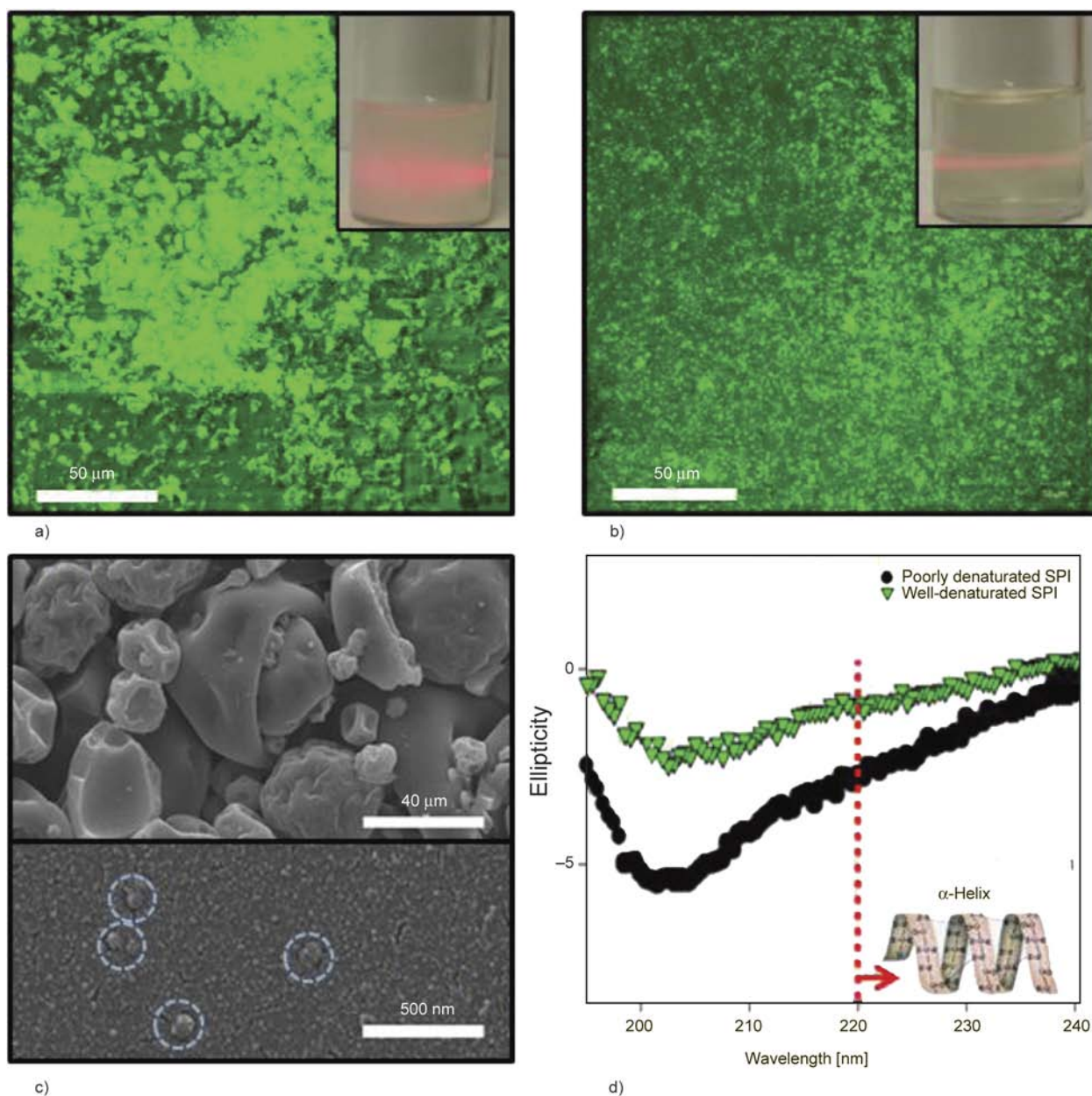


Figure 1. (a) and (b), confocal images of the poorly and well-denatured SPI particles in chloroform, respectively; the inserts are the laser scattering result for the corresponding suspension; (c) up and down, SEM images of the poorly and well-denatured SPI particles, respectively; (d) circular dichroism results for the two samples with different denaturation states

GNP surface very well as shown by the SEM image at high magnification (Figure 2d), which indicates a strong interaction between the denatured SPI and GNP. As a benefit from the strong interaction, a stable *s*-GNP-CA suspension was formed and can maintain for even several weeks (insert in Figure 2c). Finally, compared the TEM image of *s*-GNP (insert in Figure 2b), the improved transparency of GNP sheet can be found in *s*-GNP-CA (insert in Figure 2d), revealing that the thickness of GNP was reduced. These findings indicate that denatured SPI can be a very effective biotreatment agent for GNPs since

nanoscale SPI particles will provide much larger active surface area as well as more functional groups to interact with nanofillers. Although it needs further studies to learn the specific interactions, the variety of functional groups and interactions along the denatured protein chain should be the key for the SPI coating on the surface of GNPs. For example, molecular modeling results have shown that denatured protein may change its chain configuration accordingly to generate good interaction with GNPs [22]. Further, there are also residual groups on GNPs [23], which can provide extra spots for the interac-

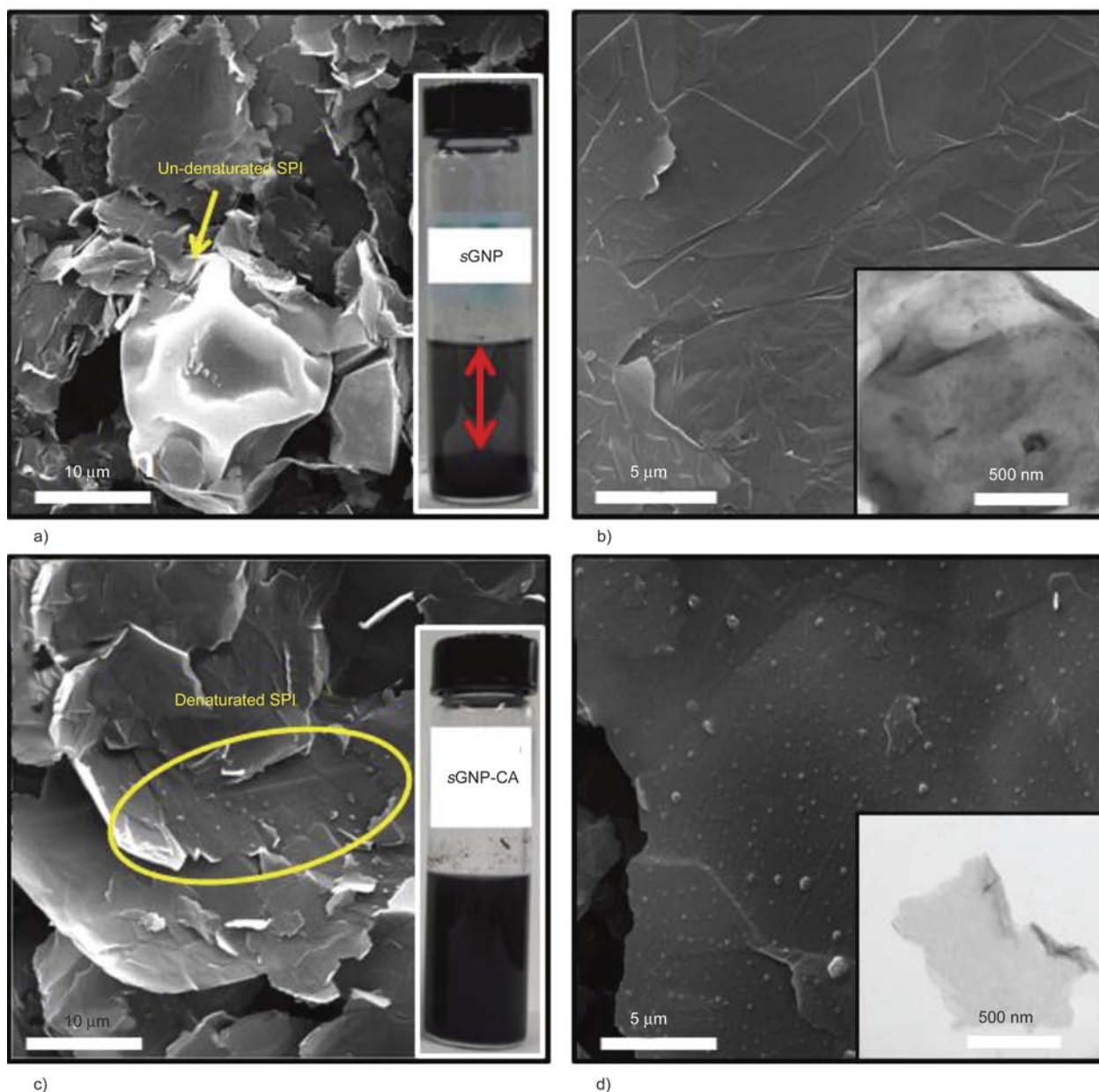


Figure 2. FESEM images of the GNP samples treated by the SPI samples: (a & b) treated by the poorly denatured SPI, (c & d) treated by the well-denatured SPI. Inserts in (a) and (c) are digital photos for the corresponding suspensions in chloroform, inserts in (b) and (d) are the corresponding TEM images for the treated GNPs.

tions with denatured protein. Based on Figure 2a–2d, one can conclude that the well-denatured SPI can generate strong interactions with other nanoparticles, such as GNPs.

To summarize the above results, one can conclude that, the denaturing agent, CA, is critical for the biotreatment of GNP via SPI. Firstly, it helps the denaturation of SPI in the organic solvent, chloroform, and reduces the SPI particle size into nanoscale. The polar group, hydroxyl, of CA should be one key for the SPI denaturation. It may form hydrogen bond with the possible polar groups on SPI and destroy the built-in interactions inside the pristine SPI parti-

cles in the organic solvent. Further, the unfolded SPI particles, that is, the denatured SPI particles provide various functional groups available for interactions with nanofillers [24]. Finally, the denatured SPI particles can coat the nanoparticle surface via some strong interactions, enabling the biotreatment of nanoparticles in an organic environment. Figure 3 further illustrates this biotreatment process via denatured SPI as described above.

As one significant application of the bio-treatment, we further studied the polymeric nanocomposites based on the *s*-GNP-CA. At the same time, other GNP samples were also studied for comparison.

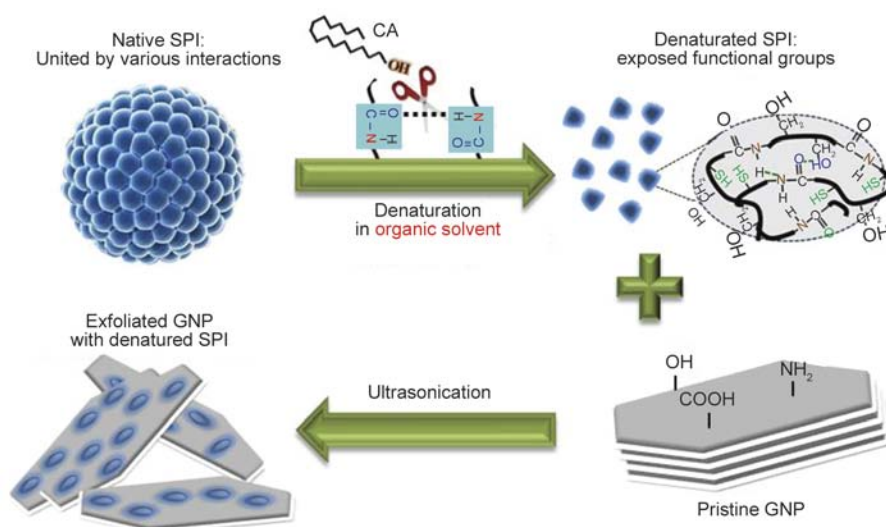


Figure 3. Schematic representation of the biotreatment of GNPs by the denatured SPI; the SPI particles can coat the surface of GNPs through the exposed functional groups on denatured SPI and the available polar groups on GNP [24]

Firstly, the dispersion quality of GNPs in the final nanocomposites has been investigated. The FESEM images for the dispersion of GNPs in the final nanocomposites are shown in Figure 4a–4d. It can be found that lots of GNP agglomerates or pristine GNP particles can be observed for the samples without the biotreatment by the denatured SPI (see Figure 4a–4c). For these samples, besides the observation of obvious gaps between the GNP and the polymer matrix (polycarbonate, PC), some GNP layers were

pulled out during the breaking, indicating poor interaction between the filler and the matrix. On the contrary, a much more homogenous dispersion of GNP was observed in Figure 4d for the sample with *s*-GNP-CA. Moreover, one can observe very thin GNP particles, few layers of graphene, and no gap between the PC matrix and *s*-GNP-CA can be found, indicating the biotreatment by the denatured SPI can contribute to some strong interactions between the polymer matrix and the GNP filler. These strong interac-

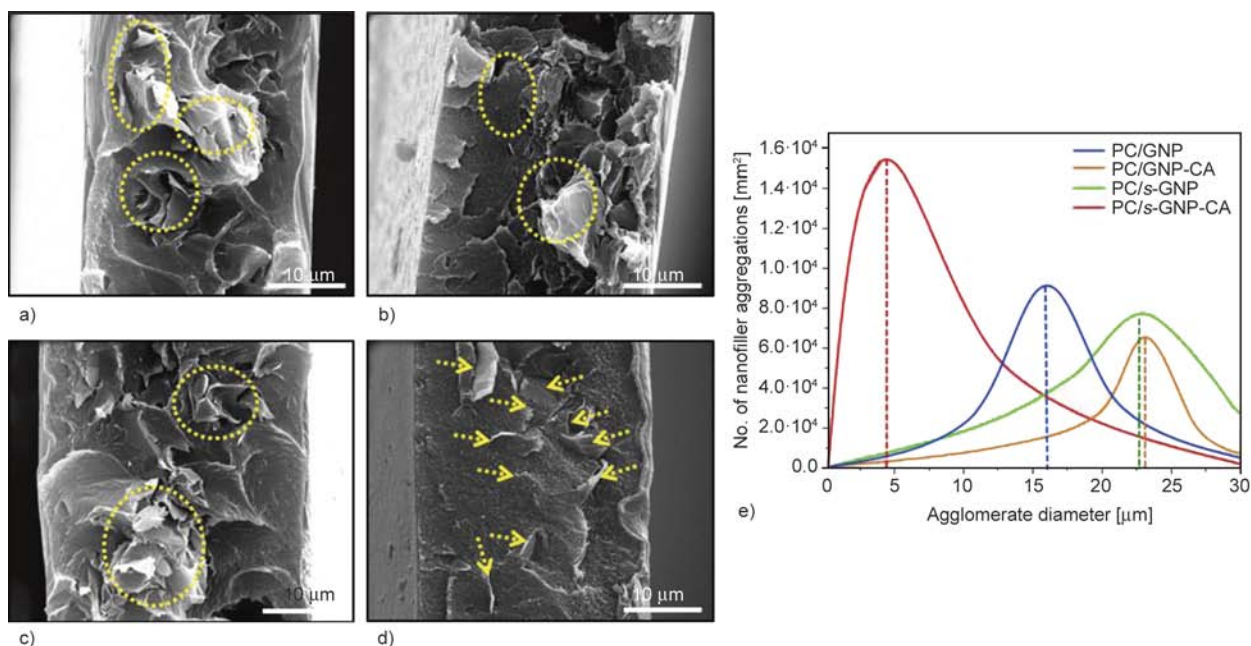


Figure 4. Comparison of the nanofiller dispersion in the nanocomposites with different GNPs. (a–d), SEM images of the fracture surface from nanocomposites with: (a) untreated GNPs, (b) CA treated GNPs, (c) *s*-GNPs, and (d) *s*-GNPs-CA (Scale bars: 10 μm). (e): quantitative analysis of nanofillers dispersion for all the nanocomposites, agglomerates in the size range below 30 μm. The GNP loading is 1 wt% for all nanocomposites.

tions finally give rise to better dispersion and even reduce the thickness of GNPs in the polymer matrix. In addition, the statistical analysis on nanofiller dispersion within the nanocomposites was performed via an in-house prepared MATLAB script, the software developed in our lab [25]. Figure 4e provides the size distributions of GNP aggregates in a range from several nanometers to 30 microns. The proportion of nanofiller aggregation with the size above 15 μm in PC/GNP, PC/GNP-CA, and PC/s-GNP are much higher than the nanocomposite with s-GNP-CA. In the size range below 10 μm , the contribution of the denatured SPI to the dispersion of GNP is more obvious as the PC/s-GNP-CA sample show the lowest level of filler aggregates, and the number density of aggregates decreased dramatically as the aggregate size increased.

The optical and electrical properties of the nanocomposites were also studied to demonstrate the advantages of the bio-treatment via denatured SPI. The transmittance spectra of all the above four nanocomposite films with thickness of ca. 40 μm are presented in Figure 5a. In specific, the transmittance, for example at 600 nm, is about only 19% for the composite film with the pristine GNP, which is almost opaque as shown in Figure 5a insert. The aggregation of the nanoparticles that being driven by the van der Waals attraction force should be the main reason for the poor transparency [26]. The transmittances at the same wavelength for PC/GNP-CA and PC/s-GNP are even lower than that of PC/GNP, especially for PC/s-GNP. This result can be explained as following. First, the un-denatured protein particles cannot improve the quality of GNP dispersion (Fig-

ure 4b, 4c); second, the big SPI particles themselves will further deteriorate the optical properties. In comparison, a dramatic increase in optical transparency can be achieved in the bio-treated composite, PC/s-GNP-CA. The transmittance is up to 62% at 600 nm wavelength. The significantly improved transparency should be contributed by two different factors related to the denatured SPI: a good GNP dispersion and the reduction of GNP thickness (Figure 4d) result in the translucency of the composite film. The high light transmittance of the nanocomposite shows its high potential in solar energy conversion applications, such as solar cells.

It is well-known that dispersion of conductive nanofillers in a polymer matrix is a vital factor determining electrical properties of the resultant nanocomposites. It has been demonstrated that the AC conductivity (σ) of a polymeric nanocomposite is a function of frequency when the filler loading is below the percolation threshold, and becomes frequency independent at a concentration level above the percolation threshold [27]. As shown in Figure 5b, the value of σ is strongly dependent on the frequency for pure PC due to its insulating nature. Similar behavior has been observed for PC/GNP, PC/GNP-CA and PC/s-GNP, indicating that the addition of pristine GNP, and the GNP treated by only CA or poorly denatured SPI all contribute little to improving the electrical conductivity mainly due to the poor filler dispersion. However, the bio-treated sample, PC/s-GNP-CA, shows a conductive property (the frequency independent behavior) mainly due to the improved GNP dispersion. In particular, the value of σ for PC/s-GNP-CA increases almost 11 orders of

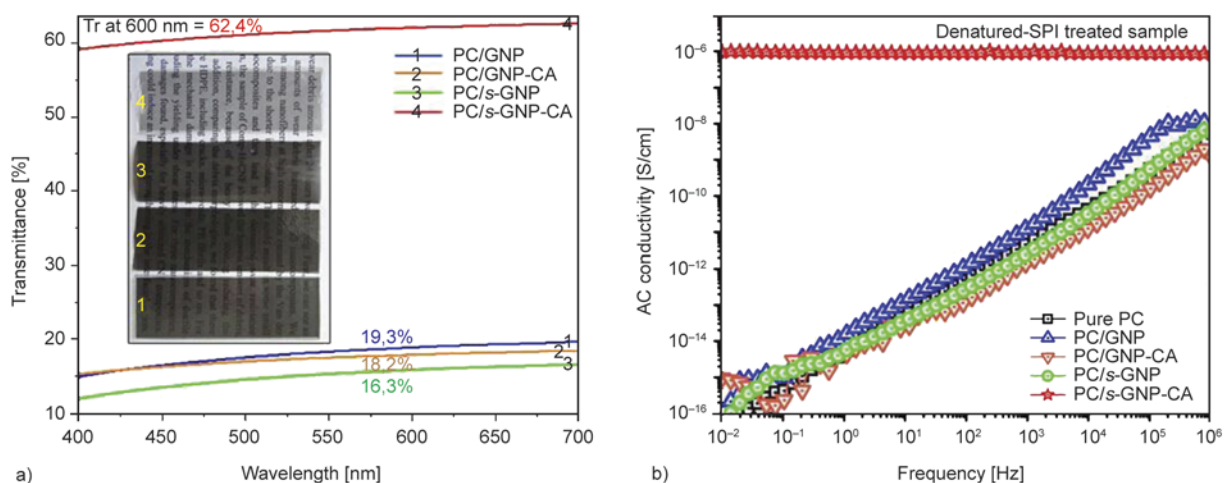


Figure 5. Properties of the nanocomposites with different GNPs: (a) optical properties as characterized by UV-vis spectroscopy; (b) AC conductive properties

magnitude (at 10^{-2} Hz) as compared to these of PC/GNP or the other two treated samples. With the same electrical conductivity improvement, the loading for PC/s-GNP-CA composite (1 wt%) is lower than the values reported in other studies (usually above 2 wt%) [28]. The good conductive and optical properties of the polymeric nanocomposite with GNP treated by the denatured SPI may make the nanocomposite very promising as flexible, transparent conductors, which are highly desired by flexible energy devices, such as flexible solar cells.

4. Conclusions

Soy protein was effectively denatured in a non-aqueous environment with a denaturing agent, cetyl alcohol. An effective biotreatment for nanofillers by the use of the denatured soy protein has been realized, for the first time to our knowledge, in an organic solvent. The studies demonstrate that soy protein denaturation led to homogenous nanoscale SPI particles (below 100 nm) in the organic solvent with the aid of the denaturing agent. The nano-scaled denatured SPI become an effective bio-treatment agent for nanoparticles, such as GNPs. When nanocomposites were fabricated with the bio-treated GNPs, it was found that the denatured SPI was able to infiltrate between GNP layers to reduce the thickness of GNPs, at the same time to notably improve the filler dispersion in the nanocomposites. As one example of the application of the denatured SPI, a PC/s-GNP-CA nanocomposite with good optical and electrical performances has also been shown in this study, which indicates that high-performance nanocomposites with the potential for photoelectric applications, such as polymer solar panels, can be fabricated based on the bio-treatment of nanoparticles via the denatured SPI. In a word, this study has laid foundation for development of a facile, cost-effective and environmentally friendly biotreatment of nanofillers in organic environment, which will remarkably extend the great potential of natural proteins for fabricating high-performance nanocomposites based on organic solution.

Acknowledgements

The authors appreciate the technical support from the Franceschi Microscopy & Imaging Center at Washington State University. The authors also gratefully acknowledge the support from NSF 1029940.

References

- [1] Liu T., Wang Y., Eyer A., Zhong W-H.: Synergistic effects of hybrid graphitic nanofillers on simultaneously enhanced wear and mechanical properties of polymer nanocomposites. *European Polymer Journal*, **55**, 210–221 (2014).
DOI: [10.1016/j.eurpolymj.2014.04.002](https://doi.org/10.1016/j.eurpolymj.2014.04.002)
- [2] Wildgoose G. G., Banks C. E., Leventis H. C., Compton R. G.: Chemically modified carbon nanotubes for use in electroanalysis. *Microchimica Acta*, **152**, 187–214 (2006).
DOI: [10.1007/s00604-005-0449-x](https://doi.org/10.1007/s00604-005-0449-x)
- [3] Lu J., Drzal L. T.: Microfibrillated cellulose/cellulose acetate composites: Effect of surface treatment. *Journal of Polymer Science Part B: Polymer Physics*, **48**, 153–161 (2010).
DOI: [10.1002/polb.21875](https://doi.org/10.1002/polb.21875)
- [4] Kunioka M., Ninomiya F., Funabashi M.: Biobased contents of organic fillers and polycaprolactone composites with cellulose fillers measured by accelerator mass spectrometry based on ASTM D6866. *Journal of Polymers and the Environment*, **15**, 281–287 (2007).
DOI: [10.1007/s10924-007-0071-6](https://doi.org/10.1007/s10924-007-0071-6)
- [5] Fernandes E. M., Pires R. A., Mano J. F., Reis R. L.: Bionanocomposites from lignocellulosic resources: Properties, applications and future trends for their use in the biomedical field. *Progress in Polymer Science*, **38**, 1415–1441 (2013).
DOI: [10.1016/j.progpolymsci.2013.05.013](https://doi.org/10.1016/j.progpolymsci.2013.05.013)
- [6] Kim J. T., Netravali A. N.: Physical properties of biodegradable films of soy protein concentrate/gelling agent blends. *Macromolecular Materials and Engineering*, **297**, 176–183 (2012).
DOI: [10.1002/mame.201100135](https://doi.org/10.1002/mame.201100135)
- [7] Mari S. A., Köster S., Bippes C. A., Yildiz O., Kühlbrandt W., Müller D. J.: pH-induced conformational change of the β -barrel-forming protein OmpG reconstituted into native *E. coli* lipids. *Journal of Molecular Biology*, **396**, 610–616 (2010).
DOI: [10.1016/j.jmb.2009.12.034](https://doi.org/10.1016/j.jmb.2009.12.034)
- [8] Ávila-Orta C. A., Cruz-Delgado V. J., Neira-Velázquez M. G., Hernández-Hernández E., Méndez-Padilla M. G., Medellín-Rodríguez F. J.: Surface modification of carbon nanotubes with ethylene glycol plasma. *Carbon*, **47**, 1916–1921 (2009).
DOI: [10.1016/j.carbon.2009.02.033](https://doi.org/10.1016/j.carbon.2009.02.033)
- [9] Numata M., Asai M., Kaneko K., Bae A-H., Hasegawa T., Sakurai K., Shinkai S.: Inclusion of cut and as-grown single-walled carbon nanotubes in the helical superstructure of schizophyllan and curdlan (β -1,3-glucans). *Journal of the American Chemical Society*, **127**, 5875–5884 (2005).
DOI: [10.1021/ja044168m](https://doi.org/10.1021/ja044168m)
- [10] Shen J., Shi M., Yan B., Ma H., Li N., Hu Y., Ye M.: Covalent attaching protein to graphene oxide via diimide-activated amidation. *Colloids and Surfaces B: Biointerfaces*, **81**, 434–438 (2010).
DOI: [10.1016/j.colsurfb.2010.07.035](https://doi.org/10.1016/j.colsurfb.2010.07.035)

- [11] Liu Y., Yu D., Zeng C., Miao Z., Dai L.: Biocompatible graphene oxide-based glucose biosensors. *Langmuir*, **26**, 6158–6160 (2010). DOI: [10.1021/la100886x](https://doi.org/10.1021/la100886x)
- [12] Zheng M., Jagota A., Semke E. D., Diner B. A., Mclean R. S., Lustig S. R., Richardson R. E., Tassi N. G.: DNA-assisted dispersion and separation of carbon nanotubes. *Nature Materials*, **2**, 338–342 (2003). DOI: [10.1038/nmat877](https://doi.org/10.1038/nmat877)
- [13] Zhang J., Jiang L., Zhu L., Jane J-L., Mungara P.: Morphology and properties of soy protein and polylactide blends. *Biomacromolecules*, **7**, 1551–1561 (2006). DOI: [10.1021/bm050888p](https://doi.org/10.1021/bm050888p)
- [14] Liao Y., Farrell T. P., Guillen G. R., Li M., Temple J. A. T., Li X-G., Hoek E. M. V., Kaner R. B.: Highly dispersible polypyrrole nanospheres for advanced nanocomposite ultrafiltration membranes. *Materials Horizons*, **1**, 58–64 (2014). DOI: [10.1039/C3MH00049D](https://doi.org/10.1039/C3MH00049D)
- [15] Liu D., Zhu C., Peng K., Guo Y., Chang P. R., Cao X.: Facile preparation of soy protein/poly(vinyl alcohol) blend fibers with high mechanical performance by wet-spinning. *Industrial and Engineering Chemistry Research*, **52**, 6177–6181 (2013). DOI: [10.1021/ie400521a](https://doi.org/10.1021/ie400521a)
- [16] Bhattacharyya S., Sinturel C., Salvetat J. P., Saboungi M-L.: Protein-functionalized carbon nanotube-polymer composites. *Applied Physics Letters*, **86**, 113104/1–113104/3 (2005). DOI: [10.1063/1.1883725](https://doi.org/10.1063/1.1883725)
- [17] Nepal D., Geckeler K. E.: Proteins and carbon nanotubes: Close encounter in water. *Small*, **3**, 1259–1265 (2007). DOI: [10.1002/smll.200600511](https://doi.org/10.1002/smll.200600511)
- [18] Karajanagi S. S., Yang H., Asuri P., Sellitto E., Dordick J. S., Kane R. S.: Protein-assisted solubilization of single-walled carbon nanotubes. *Langmuir*, **22**, 1392–1395 (2006). DOI: [10.1021/la0528201](https://doi.org/10.1021/la0528201)
- [19] Wu Y., Hudson J. S., Lu Q., Moore J. M., Mount A. S., Rao A. M., Alexov E., Ke P. C.: Coating single-walled carbon nanotubes with phospholipids. *The Journal of Physical Chemistry B*, **110**, 2475–2478 (2006). DOI: [10.1021/jp057252c](https://doi.org/10.1021/jp057252c)
- [20] Bandyopadhyaya R., Nativ-Roth E., Regev O., Yerushalmi-Rozen R.: Stabilization of individual carbon nanotubes in aqueous solutions. *Nano Letters*, **2**, 25–28 (2002). DOI: [10.1021/nl010065f](https://doi.org/10.1021/nl010065f)
- [21] Ji J-Y., Lively B., Zhong W-H.: Soy protein-assisted dispersion of carbon nanotubes in a polymer matrix. *Materials Express*, **2**, 76–82 (2012). DOI: [10.1166/mex.2012.1055](https://doi.org/10.1166/mex.2012.1055)
- [22] Zhang Y., Zhao W., Yang R., Ahmed M. A., Hua X., Zhang W., Zhang Y.: Preparation and functional properties of protein from heat-denatured soybean meal assisted by steam flash-explosion with dilute acid soaking. *Journal of Food Engineering*, **119**, 56–64 (2013). DOI: [10.1016/j.jfoodeng.2013.05.008](https://doi.org/10.1016/j.jfoodeng.2013.05.008)
- [23] Li B., Olson E., Perugini A., Zhong W-H.: Simultaneous enhancements in damping and static dissipation capability of polyetherimide composites with organosilane surface modified graphene nanoplatelets. *Polymer*, **52**, 5606–5614 (2011). DOI: [10.1016/j.polymer.2011.09.048](https://doi.org/10.1016/j.polymer.2011.09.048)
- [24] Abbasi S., Carreau P. J., Derdouri A.: Flow induced orientation of multiwalled carbon nanotubes in polycarbonate nanocomposites: Rheology, conductivity and mechanical properties. *Polymer*, **51**, 922–935 (2010). DOI: [10.1016/j.polymer.2009.12.041](https://doi.org/10.1016/j.polymer.2009.12.041)
- [25] Lively B., Zhong W-H.: An efficient quantified stereological macrodispersion analysis approach for determining microscale influences on nanocomposite material properties. *Macromolecular Materials and Engineering*, **298**, 221–234 (2013). DOI: [10.1002/mame.201200086](https://doi.org/10.1002/mame.201200086)
- [26] Lu C., Zu Y., Yam V. W-W.: Specific postcolumn detection method for HPLC assay of homocysteine based on aggregation of fluorosurfactant-capped gold nanoparticles. *Analytical Chemistry*, **79**, 666–672 (2007). DOI: [10.1021/ac061513c](https://doi.org/10.1021/ac061513c)
- [27] Liu T., Wood W., Li B., Lively B., Zhong W-H.: Electrical and dielectric sensitivities to thermal processes in carbon nanofiber/high-density polyethylene composites. *Science and Engineering of Composite Materials*, **18**, 51–60 (2011). DOI: [10.1515/secm.2011.007](https://doi.org/10.1515/secm.2011.007)
- [28] Li J., Vaisman L., Marom G., Kim J-K.: Br treated graphite nanoplatelets for improved electrical conductivity of polymer composites. *Carbon*, **45**, 744–750 (2007). DOI: [10.1016/j.carbon.2006.11.031](https://doi.org/10.1016/j.carbon.2006.11.031)

Non-isothermal cure and exfoliation of tri-functional epoxy-clay nanocomposites

F. Shiravand, J. M. Hutchinson*, Y. Calventus

Centre for Research in NanoEngineering, and Departament de Màquines i Motors Tèrmics, ETSEIAT, Universitat Politècnica de Catalunya, 08222 Terrassa, Barcelona, Spain

Received 27 November 2014; accepted in revised form 25 February 2015

Abstract. The non-isothermal cure kinetics of polymer silicate layered nanocomposites based on a tri-functional epoxy resin has been investigated by differential scanning calorimetry. From an analysis of the kinetics as a function of the clay content, it can be concluded that the non-isothermal cure reaction can be considered to consist of four different processes: the reaction of epoxy groups with the diamine curing agent; an intra-gallery homopolymerisation reaction which occurs concurrently with the epoxy-amine reaction; and two extra-gallery homopolymerisation reactions, catalysed by the onium ion of the organically modified clay and by the tertiary amines resulting from the epoxy-amine reaction. The final nanostructure displays a similar quality of exfoliation as that observed for the isothermal cure of the same nanocomposite system. This implies that the intra-gallery reaction, which is responsible for the exfoliation, is not significantly inhibited by the extra-gallery epoxy-amine cross-linking reaction.

Keywords: nanocomposites, thermosetting resins, thermal properties, exfoliation, epoxy resin

1. Introduction

Polymer layered silicate (PLS) nanocomposites based on thermosetting polymers, such as epoxy resin, are interesting as a new class of material. In comparison with the unreinforced epoxy resin, these nanocomposites can exhibit significant improvements in mechanical properties, such as an increase in the modulus, tensile strength and impact strength, and in thermal properties such as flame retardance. As a consequence of the enhancement in these properties, they can find increased use in a wide range of industrial areas, from adhesives to coatings, and from microelectronic applications to high performance aerospace composite systems [1–7].

The procedure for the fabrication of epoxy-clay nanocomposites is based on *in-situ* polymerisation. Although this procedure is apparently simple, involving the mixing of the resin, clay and curing agent and

effecting a suitable cure schedule, it transpires that the nanostructure and properties of the cured nanocomposite are very much dependent on the detailed conditions of the whole fabrication procedure, which includes, for example, the method of mixing the components as well as the curing process itself [4, 6]. The curing process, which may involve isothermal or non-isothermal (dynamic) cure schedules, or a combination or sequence of either of these, may be monitored and characterised by thermal analysis techniques, from which a number of kinetic parameters may be obtained. These parameters and other details of the cure process can be related to the nanostructure development, and hence thermal analysis is a useful tool in the study of these PLS nanocomposites [8–20].

Most of the studies of the cure reaction of epoxy PLS nanocomposites have concentrated on the iso-

*Corresponding author, e-mail: hutchinson@mmt.upc.edu
© BME-PT

thermal or non-isothermal cure of bi-functional epoxy resin systems, typically diglycidyl ether of bisphenol-A (DGEBA); for example, only reference 13 of those cited immediately above (references 8 to 20) does not use DGEBA. Considerably less attention has been paid to the isothermal and/or non-isothermal cure behaviour of PLS nanocomposites based upon high-functionality epoxy resins, though there are exceptions, such as the study of tri- and tetra-functional epoxy resin systems [21] and our own earlier investigations of a tri-functional epoxy resin nanocomposite system based upon triglycidyl p-amino phenol (TGAP) [22, 23]. Strangely, Becker *et al.* [21] found that the DGEBA resin resulted in better exfoliation than for the resins of higher functionality, which is exactly contrary to our own experience. We found that, in the isothermal cure of TGAP-based nanocomposites, two distinct reactions occurred: the first of these reactions was very rapid and could be associated with the homopolymerisation reaction of the resin within the clay galleries, while the second reaction represented the cross-linking reaction of the TGAP with the curing agent, diaminodiphenyl sulphone (DDS) [22]. These TGAP systems resulted in significantly better exfoliation of the cured nanocomposite, as observed by both small angle X-ray scattering (SAXS) and transmission electron microscopy (TEM), in comparison with earlier studies of DGEBA-based nanocomposites [16–18, 20]. We attributed this to the beneficial occurrence, in the TGAP system, of the intra-gallery reaction before the bulk cross-linking reaction, whereas the homopolymerisation reaction in the DGEBA system does not occur until after the major part of the bulk cross-linking reaction has occurred, which inhibits any further separation of the clay layers from taking place.

This earlier work was related to the isothermal cure behaviour of TGAP/hardener/clay systems. Not only were the kinetic parameters and activation energy determined for each of these two reactions, intra- and extra-gallery, but also the effect of the cure temperature on the thermal properties and final nanostructure was studied [23]. It transpires that the first reaction, which takes place within the clay galleries and promotes the exfoliation of the clay, is enhanced at higher cure temperature, and hence higher isothermal cure temperatures give rise to increased exfo-

liation in the cured nanocomposite. This result is in agreement with the observations of Becker *et al.* [21], who concluded that higher cure temperatures were found to improve clay delamination, as well as increasing the toughness and modulus in the case of both DGEBA- and TGAP-based materials. In order to further clarify the process of exfoliation in these TGAP-based systems, the goal of the present paper is to investigate the non-isothermal (dynamic) cure behaviour of the same system for comparison with the isothermal cure behaviour, to obtain the kinetic parameters and activation energy, and to analyse the quality of the final nanostructure.

2. Experimental

2.1. Materials

The epoxy resin (TGAP), with trade name Araldite MY0510 (Huntsman Advanced Materials, Huntsman Corporation, Texas 77380, USA) and an epoxy equivalent between 95–106 g/eq, the curing agent, 4,4-diamino diphenyl sulphone (DDS), with trade name Aradur 976-1 (Sigma-Aldrich Quimica SL, Madrid, Spain), and the organically modified montmorillonite (MMT), with trade name Nanomer I.30E (Nanocor Inc., Arlington Heights, IL, USA), consisting of 70–75 wt% montmorillonite and 25–30 wt% octadecylamine, with a cation exchange capacity of 92 meq/100 g, were used without further purification. First, TGAP and MMT were mixed mechanically in various proportions of MMT: 0, 2, 5 and 10 wt%. The curing agent, DDS, was added to the resin-clay mixture in a proportion of 52 wt%, which corresponds to a slight excess of epoxy, as is recommended by the manufacturer. Stoichiometric ratios were calculated based on the amine hydrogen equivalent weight (AHEW). The mixture was finally degassed under vacuum at room temperature.

2.2. Calorimetry

Small sample quantities (6–10 mg) were taken from this preparation and placed in sealed aluminium pans, ready for the curing experiments that were carried out using a conventional differential scanning calorimeter (DSC), DSC821e (Mettler-Toledo AG, Schwerzenbach, Switzerland). This instrument is equipped with a robot for sample placement in the furnace, with intra-cooling for sub-ambient temperatures, and with STAR^e software for data evaluation. The DSC was calibrated with indium for both

heat flow and temperature, and the experiments were performed under a flow of dry nitrogen gas at 50 mL/min.

All the samples were cured non-isothermally from 0 to 290°C at different heating rates, β : 2, 5 and 10°C/min. The glass transition temperature, T_g , of the fully cured nanocomposite was determined from a second non-isothermal scan, from 50 to 300°C at 10°C/min heating rate. It is worth pointing out that the T_g of the non-isothermally cured nanocomposites is significantly lower than that for the isothermally cured nanocomposites, as a consequence of the difference in network structure. Therefore, whereas the determination of the T_g of the isothermally cured nanocomposites required the use of a temperature modulated technique, TOPEM [24], the T_g of the non-isothermally cured samples can be measured in the conventional way from the step change in the heat flow during the second scan in the DSC.

Although isothermal cure experiments were not performed for this work, comparison is made between the isothermal and the non-isothermal cure kinetics in order to clarify the reactions involved in the non-isothermal cure. For completeness, therefore, the isothermal cure procedure is also described here. The two systems involved are TGAP/DDS without any clay, cured isothermally at 150°C for 4 h, and the nanocomposite system with 5 wt% clay, TGAP/DDS/MMT(5 wt%), cured isothermally at 165°C for 2 h. The procedure in each case was to heat the DSC furnace to the required isothermal temperature and then to insert the freshly prepared sample into the DSC by robot and immediately start the cure experiment. These isothermal experiments were followed by a second (non-isothermal) scan in the DSC, from 50 to 300°C, and in TOPEM, from 100 to 290°C, in order to determine the residual heat of reaction and the glass transition temperature of the fully cured nanocomposite, respectively.

2.3. Nanostructure characterisation

The final nanostructure was observed for bulk samples which had been cured in an air-circulating oven in which the temperature was increased linearly with time at a rate of 10°C/min. The nanostructural characterisation was made by SAXS and TEM. X-ray diagrams were obtained using a Bruker D8 Advanced diffractometer (Bruker Corporation, Billerica, Mass, USA), measurements being taken

in a range of 2θ from 1 to 8° with copper K α radiation ($\lambda = 0.1542$ nm); for this, powder samples were obtained by ball-milling (Retsch model MM 400, Retsch GmbH, Haan, Germany) the bulk samples using 20 mm diameter steel balls and a frequency of 20 Hz for a period of 4 minutes. The TEM studies were carried out on a high resolution microscope (Jeol-2010, Jeol Ltd, Tokyo, Japan) at 200 kV accelerating voltage with high resolution imaging and with 0.23 nm point resolution; for this, sections of approximately 50 nm thickness were cut from the bulk sample by ultra-microtomy.

3. Kinetic analysis

The kinetic model for the time dependence of the degree of cure, α , for a non-isothermal curing process with a constant heating rate can be described by the following Equation (1):

$$\frac{d\alpha}{dt} = k(T)f(\alpha) \quad (1)$$

where $k(T)$ is the rate constant, which depends on the temperature, T , and $f(\alpha)$ is a function of the kinetic model. The rate constant $k(T)$ can be further expressed by the Arrhenius equation (Equation (2)):

$$k(T) = A \exp\left(-\frac{E}{RT}\right) \quad (2)$$

where E is the activation energy, A is the pre-exponential factor, and R is the universal gas constant. In this paper, the autocatalytic model in which the initial cure rate is zero, known as the Sesták-Berggren equation, is chosen for the $f(\alpha)$ function, as shown in Equation (3):

$$f(\alpha) = \alpha^m(1 - \alpha)^n \quad (3)$$

where m and n are the reaction orders.

In the DSC experiments, the heat flow, ϕ , that is measured and which results from the curing reaction is assumed to be proportional to the rate of cure according to Equation (4):

$$\phi = \left(\frac{d\alpha}{dt}\right) \Delta H_{\text{tot}} \quad (4)$$

where ΔH_{tot} is the total heat of cure of the reaction, obtained from the total area under the non-isothermal cure curve.

The usual approach in the kinetic analysis is to determine the activation energy by a direct method, and subsequently to determine $\ln(A)$ and the kinetic

parameters of the function $f(\alpha)$. There has been considerable discussion in the literature about the numerous methods for the evaluation of the kinetic parameters, and in particular of the activation energy [25]. For example, Starink [26] gives an extensive comparison of methods for the analysis of constant heating rate experiments, and concludes that so-called ‘Type B’ methods, such as those due to Ozawa [27] and Vyazovkin [28, 29], in which some approximations of the temperature integral are made, are often to be preferred to those methods (Type A), such as the Friedman isoconversional method, which make no such approximations, in particular as a consequence of uncertainty in the application of a baseline to the experimental data. Accordingly, here we adopt the most commonly used Type B method, the Kissinger method [30, 31], for the determination of the activation energy. This method is based upon the determination, as a function of the heating rate β , of the temperature, T_p , at which the heat flow passes through a maximum. The approximation made here is that the degree of conversion is a constant value at this peak, independent of the heating rate, and leads to a linear relationship between $\ln(\beta/T_p^2)$ and the reciprocal of T_p , from which the activation energy, E , is obtained.

Once the activation energy has been determined, the other kinetic parameters can be obtained from the DSC curves by the method suggested by Málek [32], which involves the calculation of two functions, $y(\alpha)$ and $z(\alpha)$, defined by Equations (5) and (6) for non-isothermal cure:

$$y(\alpha) = \phi \cdot \exp x = \Delta H_{\text{tot}} A f(\alpha) \quad (5)$$

$$z(\alpha) = \phi T^2 = C f(\alpha) g(\alpha) \quad (6)$$

where $x = E/RT$ is a dimensionless quantity, $C = \Delta H_{\text{tot}} \beta / RT$, and $g(\alpha) = \int d\alpha / f(\alpha)$ between the limits of 0 and α . The functions $y(\alpha)$ and $z(\alpha)$ are invariant with respect to the heating rate and are sensitive to small changes in the kinetic model $g(\alpha)$. In practice, the $y(\alpha)$ and $z(\alpha)$ functions are normalised between 0 and 1 for convenience.

4. Results and discussion

4.1. DSC study of the TGAP/DDS system

As a starting point and reference with which to compare the dynamic cure behaviour of the TGAP clay nanocomposite, we begin by describing the cure kinetics of the system without clay, namely the

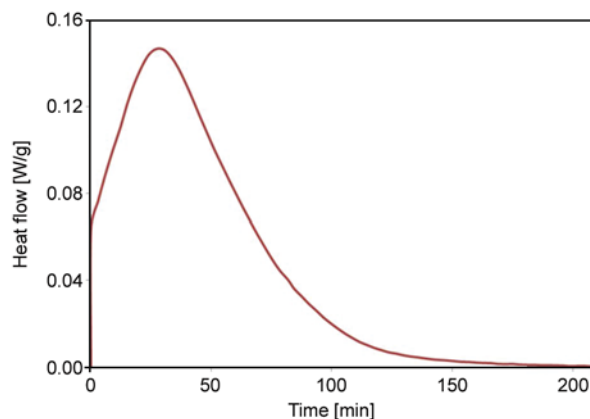


Figure 1. Isothermal DSC curve for TGAP/DDS system at 150°C

TGAP/DDS system. In the isothermal cure of TGAP/DDS studied earlier [24], a single exothermic peak appears, as shown in Figure 1, which is related to the cross-linking reaction of TGAP/DDS. In contrast, during a dynamic scan of the same system, as shown in Figure 2, the cure curve exhibits both a peak and a shoulder, which shift to higher temperature for faster heating rates. It is clear that the non-isothermal cure process consists of two overlapping reactions: the first is the main reaction, and is attributed to the cross-linking reaction between the TGAP and DDS; the second, which appears as a shoulder on the high temperature flank of the main peak, could be attributed to a number of different reactions, and is discussed further after examining the total heat of reaction.

The total heat of the reaction, represented by the area under both the first and second peaks, and determined as the average from the non-isothermal scans at the three different heating rates, is found to

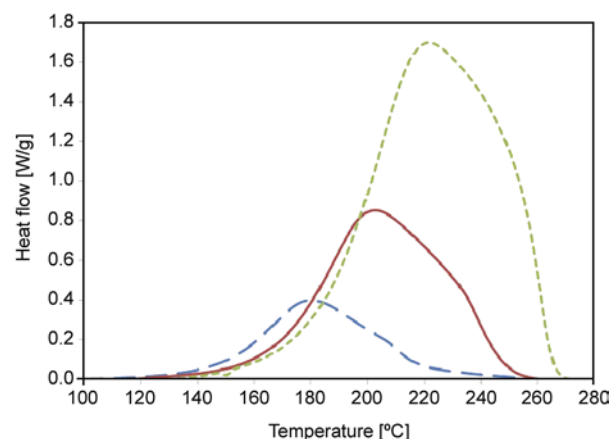


Figure 2. Non-isothermal DSC cure curve for TGAP/DDS system from 0–280°C with different heating rates as indicated: long dash, 2°C/min; full line, 5°C/min; short dash, 10°C/min

be 98.5 kJ/ee. Frigione and Calò [33] quote a range of values, from 94.6 to 96.8 kJ/ee, for the non-isothermal cure of the same TGAP epoxy with diamino diethyltoluene as the curing agent, with heating rates from 5 to 15°C/min, while Varley *et al.* [34] quote a value of 110.5 kJ/ee for the non-isothermal cure of TGAP with DDS. The result presented here, 98.5 kJ/ee, clearly lies between the values quoted by these other authors. There are several reasons why there appears to be a range of values for the heat of reaction of TGAP. Frigione and Calò [33] use an epoxy equivalent of 101 g/ee, from the manufacturer's literature, and a stoichiometric ratio of epoxy:amine, whereas Varley *et al.* [34] determine the epoxy equivalent by titration as 106 g/ee and use a molar ratio epoxy:amine of 1:0.9, implying a slight excess of epoxy. Whereas previously we determined the epoxy equivalent by titration as 95 g/ee [24], which is at the lower end of the range of values 95 to 106 g/ee given in the manufacturer's literature, in the present work we found that some homopolymerisation of the epoxy resin had taken place, presumably initiated by the N in the TGAP chemical structure, resulting in a slight increase in the glass transition temperature of the resin. Accordingly, for the determination of the heat of reaction in units of kJ/ee we also use the value of 106 g/ee together with the molar ratio of 1:0.9 for the epoxy:amine mixture.

We discuss now the composite peak that appears in the non-isothermal scan of TGAP/DDS, which can be deconvoluted into two separate exothermic peaks by means of the PeakFit program (PF version v4, Jandel Scientific software, Systat Software Inc., San Jose, California, USA). Similar observations were made by Frigione and Calò [33], who found a pronounced shoulder in the last part of the dynamic exotherm peak, which they attributed to 'diffusional processes taking place at higher conversions', and which they were unable to fit using an autocatalytic model based upon the Equation (7) [35, 36]:

$$\frac{d\alpha}{dt} = (k_1 + k_2\alpha^m)(1 - \alpha)^n \quad (7)$$

where k_1 and k_2 represent the temperature dependent rate coefficients for the reaction catalysed by proton donors initially present in the system and those that are produced during cure, respectively. Here, the fit obtained using the asymmetric double sigmoidal function (ADL) shows quite good agree-

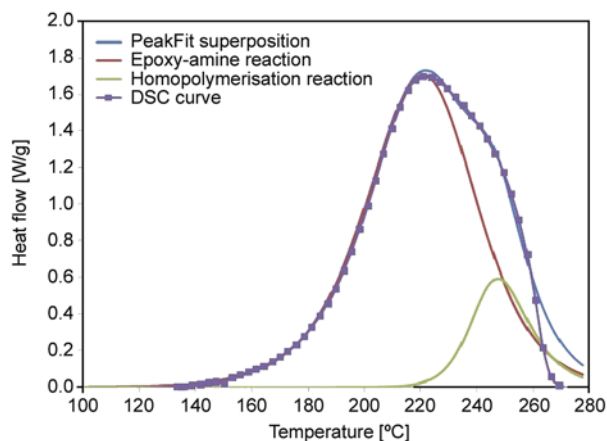


Figure 3. Deconvoluted peaks for non-isothermal cure of TGAP/DDS system at 10°C/min: squares, original DSC curve; red curve, first reaction, epoxy-amine cross-linking; green curve, second reaction, homopolymerisation; blue curve, PeakFit superposition

ment with the experimental data, a typical example being shown in Figure 3 for a heating rate of 10°C/min. It is noticeable, however, that the abrupt decrease in the experimentally measured heat flow at the end of the reaction, at temperatures higher than about 260°C, is not well modelled by the PeakFit programme, even though the fit using the ADL function shown here was better than that obtained using any of the other available functions.

We now consider the following possibilities for the appearance of such a composite peak.

- The first peak is due to the reaction of the epoxy groups with primary amines, whereas the second is due to reactions with secondary amines. The argument here would be that the reactivity of primary and secondary amines is significantly different. It should be noted that DDS, particularly in respect of the secondary amines, is less reactive than other aromatic amines.
- For some reason the TGAP/DDS cross-linking reaction during non-isothermal cure results in a topological network structure which inhibits, at some degree of cure, the further reaction of the TGAP with the DDS. For this reason, higher temperatures are required in order to provide sufficient mobility to the reacting species, whereupon a further reaction occurs. This argument is similar to that put forward by Frigione and Calò [33], which was based upon the need for diffusional processes to take place at higher temperatures.
- The cure process begins with the reaction of epoxy groups with primary amines. This reac-

tion produces secondary amines which themselves react with the epoxy to produce tertiary amines, which in turn act as an initiator of epoxy homopolymerisation. These tertiary amines act in conjunction with the nitrogen of the TGAP and the alcohol groups formed by the reaction of the TGAP with the DDS to provide a strong driving force for homopolymerisation. Possibly in combination also with topological constraints, as proposed in (b) above, this would promote epoxy homopolymerisation as the preferred reaction mechanism.

In order to distinguish between these various possibilities, some further information is required, which is afforded by the determination of the glass transition temperature of the fully cured system, $T_{g\infty}$. The $T_{g\infty}$ for the non-isothermally cured sample of TGAP/DDS can be determined from a second DSC scan, and the results are presented in Figure 4. As is often observed, the glass transition temperature of the sample that has been cured non-isothermally is lower than that of a sample cured isothermally, which was determined in earlier work by means of the temperature modulated DSC technique TOPEM to be around 256°C [24]. Here, though, the $T_{g\infty}$ of the non-isothermally cured system is very much lower, and decreases with increasing heating to reach a value as low as 206°C at 10°C/min heating rate. This observation needs to be consistent with the possible explanation for the presence of a composite reaction curve, as shown in Figures 2 and 3, as discussed immediately above.

Possibility (a) does not present any obvious reason for why the $T_{g\infty}$ should decrease with increasing heating rate, as primary and secondary amines would be expected to lead to similar network structures in the cured system. Nor does possibility (b) explain this

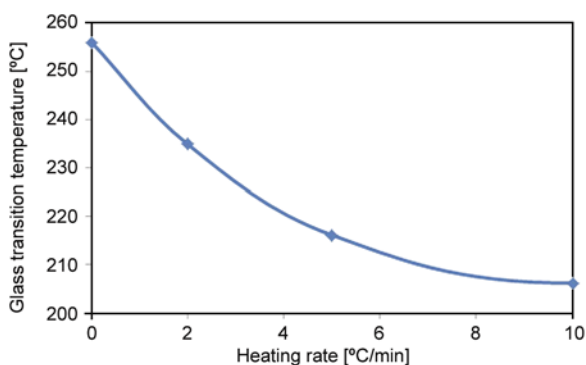


Figure 4. Glass transition temperature of the non-isothermally cured TGAP/DDS system as a function of the heating rate

observation if the effect of the topological constraint is simply to delay the secondary amine reaction. On the other hand, possibility (c) implies that the network structure would indeed be different, as more homopolymerisation would occur the higher is the heating rate. The asymmetric shape of the second deconvoluted peak in Figure 3 might result from the gradually increasing contribution from the homopolymerisation reaction as the tertiary amines are progressively created. Since homopolymerisation is associated with a reduced cross-link density, and hence with a reduction in $T_{g\infty}$, we believe that the second peak in the composite non-isothermal curing reaction occurs as a consequence of homopolymerisation.

We now examine the corresponding behaviour of the same system in which clay is now incorporated.

4.2. DSC study of the TGAP/DDS/MMT system

A typical isothermal cure curve, obtained by DSC, for the TGAP/DDS/MMT system is shown in Figure 5, for the particular case of cure at 165°C. As can be seen, there are clearly two exothermic peaks, distinctly different from the single exothermic reaction seen for isothermal cure of the system without clay shown in Figure 1; the first rapid peak is attributed to the TGAP homopolymerisation within the clay galleries (intra-gallery reaction), while the main broad peak is related to the cross-linking reaction between TGAP and DDS in the bulk of the sample (extra-gallery reaction). The justification for assigning the first peak to a homopolymerisation reaction catalysed by the organically modified clay has been given earlier [22, 23]. One might therefore anticipate, for the non-isothermal cure of the TGAP/DDS/MMT system, more complex reaction kinetics than has

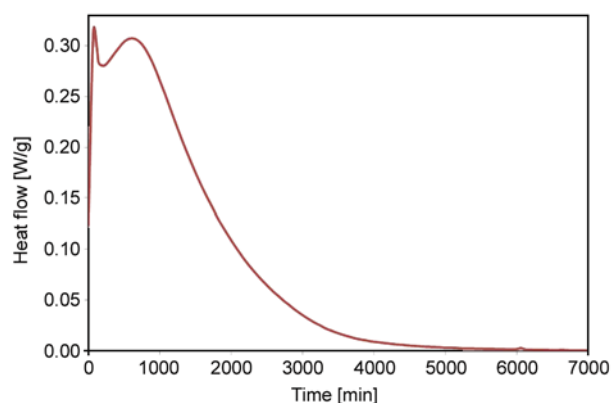


Figure 5. Isothermal DSC scan of the TGAP/DDS/MMT(5 wt%) system at 165°C

been shown above for the TGAP/DDS system without clay, where the TGAP/DDS reaction is accompanied by an epoxy homopolymerisation reaction catalysed by the tertiary amines. This is indeed found to be the case.

A typical non-isothermal cure curve for the TGAP/DDS/MMT system is shown in Figure 6. Although the appearance of these curves is very similar to that of the non-isothermal cure curves for the system without clay shown in Figures 2 and 3, when they are deconvoluted by the same PeakFit program software there appear three distinctly separate peaks, rather than two, as shown in Figure 7 for the particular case of the heating rate of 10°C/min.

The assignment of the reactions associated with each of these peaks is now considered. In order to distinguish between them, the heat of reaction is determined for each deconvoluted peak, denominated 1st, 2nd and 3rd peak in order of increasing temperature. The average values, ΔH_{av} , are determined from the cure curves for the three different heating rates used, for which no significant dependence of heat of reaction on heating rate was observed.

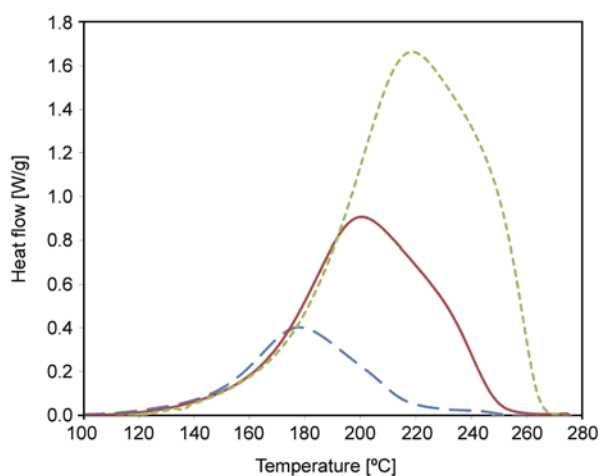


Figure 6. Non-isothermal DSC cure curve for TGAP/DDS/MMT(5 wt%) system from 0°C to 280°C for different heating rates: blue long dash, 2°C/min; red full line, 5°C/min; green short dash, 10°C/min

Table 1. Average heat of reaction, ΔH_{av} [kJ/ee], for the total reaction and for each peak after deconvolution of the non-isothermal cure curve for the TGAP/DDS/MMT system

MMT content	0	2	5	10
	[wt%]			
ΔH_{av} (1 st peak)	74.0	88.5	80.0	71.0
ΔH_{av} (2 nd peak)	–	6.2	14.0	19.0
ΔH_{av} (3 rd peak)	24.5	7.3	7.6	8.5
ΔH_{av} (total heat)	98.5	102.0	101.6	98.5

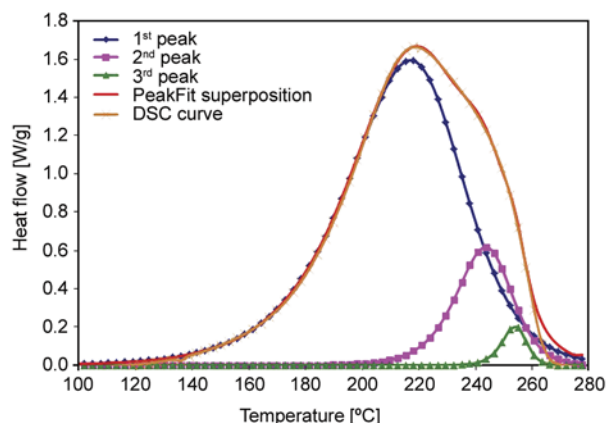


Figure 7. Deconvolution, using PeakFit program, of non-isothermal DSC scans (indicated by brown crosses) of TGAP/MMT/DDS system with 5 wt% MMT at 10°C/min heating rate, into three peaks: 1st peak, blue rhombus; 2nd peak, cyan squares; 3rd peak, green triangles. The full red line shows the overall fit.

The results are presented in Table 1 as a function of the MMT content, where the heats of reaction are given in units of kJ/ee calculated using an epoxy equivalent of 106 g/eq. Each of the three peaks is now considered in turn.

The 1st peak is clearly the most intense and occurs at the lowest temperature, with a maximum at just less than 220°C for the heating rate of 10°C/min, for example, and is attributed principally to the cross-linking reaction of the TGAP and the DDS. This can be justified by comparison with the system without clay, for which the 1st peak occurred also at about 220°C for the same heating rate of 10°C/min, the slight reduction in the peak temperature for the system with clay being attributed to the catalytic effect of the organically modified MMT, observed earlier in epoxy-clay nanocomposites based upon DGEBA epoxy resin [16, 17]. However, the isothermal cure for the TGAP/DDS/MMT system showed that there is a very rapid intra-gallery homopolymerisation reaction that occurs before the cross-linking reaction (see Figure 5). Furthermore, comparison of the heats of reaction given in Table 1 shows that the introduction of a small amount of clay (less than or equal to 5 wt%) into the system considerably increases the heat of reaction of this 1st peak. We believe, therefore, that this first peak includes both the cross-linking reaction and the intra-gallery homopolymerisation reaction.

It is interesting to examine further the effect of clay content on the heat of reaction of the 1st peak. The

heat of reaction first increases, from 74.0 to 88.5 kJ/ee for a clay content of 2 wt%, and thereafter decreases with increasing clay content. Such a reduction in the heat of reaction with increasing clay content (here from 2 to 10 wt%) has been observed in much of our earlier work on epoxy/clay systems [16, 17, 20, 37], and can be attributed either to the effect of the stoichiometry of the reaction or to the fact that the heat of reaction for homopolymerisation is smaller than that for the epoxy-amine reaction [17, 38, 39]. The initial increase in the heat of reaction for the clay content of 2 wt% may be explained on the basis of stoichiometry, as follows. During the non-isothermal cure, the cross-linking reaction of the 1st peak is accompanied by a homopolymerisation reaction, which consumes epoxy groups without any reaction with the DDS. For 0 wt% clay in the system TGAP/DDS, there is a slight excess of epoxy, and hence the cross-linking reaction occurs in conditions that are not stoichiometric, for which reason the heat of reaction will be smaller than it would be in stoichiometric conditions. As the clay content is increased, the contribution of the homopolymerisation reaction increases, and consequently the cross-linking reaction associated with the 1st peak will move first into stoichiometric conditions, with a concomitant increase in the heat of reaction, and then into conditions of excess DDS, which would result in a decrease of the heat of reaction with increasing clay content. We believe that the results presented in Table 1 indicate that stoichiometric conditions for the cross-linking reaction occur when the clay content is between 0 and 5 wt%, possibly close to 2 wt%.

In addition to this effect, it must also be borne in mind that the heat of reaction for homopolymerisation is smaller than that for the epoxy-amine reaction [17, 38, 39]. As a consequence, there is a significant reduction in the heat of reaction as the clay content is increased beyond 2 wt%, and in fact to such an extent that for 10 wt% MMT the heat of reaction is even less than that for the system without clay. This result may also be taken to indicate that the amount of intra-gallery homopolymerisation that takes place is greatest for the highest clay loading; this observation will be considered later when the nanostructure of these nanocomposites is discussed. Considering now the 2nd peak, Table 1 shows that the heat of reaction for this peak increases systematically with clay content. This is further illustrated in Figure 8, where it can be confirmed that the heat of

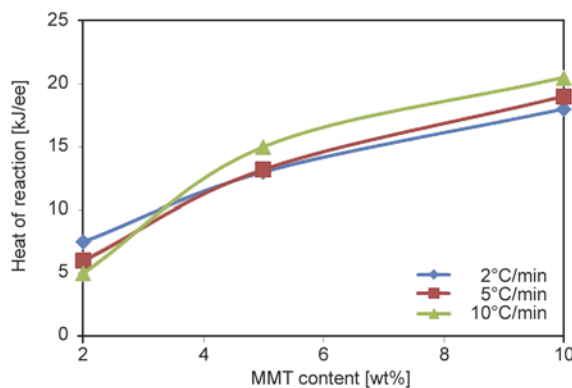


Figure 8. Dependence on MMT content of the heat of reaction corresponding to the 2nd peak for different heating rates: 2°C/min, blue rhombus; 5°C/min, red squares; 10°C/min, green triangles.

reaction is essentially independent of heating rate. The presence of MMT therefore clearly enhances this 2nd reaction. Examination of Figure 7 shows that the 2nd reaction begins at about the temperature of the maximum of the 1st peak, and since the intra-gallery reaction has therefore already largely occurred simultaneously with the cross-linking reaction in the 1st peak, we attribute the 2nd peak to an extra-gallery epoxy homopolymerisation reaction catalysed by the organically modified MMT.

The 3rd peak shows a dramatic decrease in the heat of reaction simply as a result of the presence of clay, with no significant or systematic dependence on the clay content. This peak is assigned to the extra-gallery epoxy homopolymerisation reaction, initiated by tertiary amines. The strong reduction in the heat of reaction corresponding to this peak when the clay is added may be attributed mainly to the epoxy homopolymerisation that is now taking place within the clay galleries, leaving fewer epoxy groups to react in the extra-gallery regions.

4.3. Kinetic analysis of the TGAP/DDS/MMT system

The separation of the composite peak into the three peaks corresponding to the reactions discussed above allows also the determination of, amongst other things, their individual activation energies. By applying the Kissinger method, the activation energy for each of these reactions has been found, and the results are given in Table 2 for comparison with the Kissinger values of the activation energy obtained for the composite curves without deconvolution.

Considering first the TGAP/DDS system without clay, for which the non-isothermal cure curves at 2,

Table 2. Kinetic parameters for non-isothermal cure of the TGAP/DDS/MMT system

MMT content	0	2	5	10
	[wt%]			
1st peak: cross-linking + intra-gallery homopolymerisation				
E [kJ/mol]	74	77	72	80
A [s ⁻¹]	$4.0 \cdot 10^5$	$1.7 \cdot 10^6$	$6.4 \cdot 10^5$	$4.4 \cdot 10^6$
m	0.5	0.4	0.5	0.2
n	1.6	1.6	1.5	1.7
$m+n$	2.1	2.0	2.0	1.9
2nd peak: extra-gallery homopolymerisation, catalysed by MMT				
E [kJ/mol]	–	93	79	62
3rd peak: extra-gallery homopolymerisation, catalysed by tertiary amine				
E [kJ/mol]	82	106	97	97

5 and 10 K/min are shown in Figure 2, the Kissinger activation energy corresponding to these three heating rates is found as 60.1 kJ/mol. This is somewhat larger than the value of 50.9 kJ/mol quoted by Varley *et al.* [34] for the same TGAP/DDS system, but the explanation for this apparent discrepancy lies in the range of heating rates and in the averaging process associated with the Kissinger method. Varley *et al.* [34] use a range of heating rates from 2 to 30 K/min for their evaluation of the activation energy, whereas our value of 60.1 kJ/mol is obtained for a more limited range, covering the slower heating rates. When we extend the range of heating rates to include also 20 and 30 K/min, the average activation energy is found to be 50.4 kJ/mol, in very close agreement with Varley *et al.* [34]. The dependence of $\ln(\beta/T_p^2)$ on the reciprocal of T_p is clearly not linear over the whole range of heating rates, and the reason for this is that the overall cure curves, such as those shown in Figure 2 for the TGAP/DDS system, consist of more than a single reaction, each reaction having a different activation energy. It is therefore not very meaningful to evaluate the Kissinger activation energy, as the value will depend on which reaction is predominant in determining the peak temperature according to the range of heating rates used.

The same considerations apply also to the TGAP/DDS/MMT system, for which the non-isothermal cure curves for the 5 wt% clay content are shown in Figure 6, for heating rates of 2, 5 and 10 K/min. Using this range of heating rates, the Kissinger activation energy is found as 63.8 kJ/mol, whereas the inclusion of the higher heating rates of 20 and 30 K/min gives a value of 56.5 kJ/mol. In general, the observed reduction in the Kissinger activation

energy as the range of heating rates is extended to higher values is consistent with the activation energies found for the deconvoluted peaks and shown in Table 2: the activation energies for the 2nd and 3rd peaks are higher than those for the 1st peak; at lower heating rates, where the different reactions overlap in the approximate range of their peak temperatures, the 2nd and 3rd reactions significantly influence the composite peak temperature; on the other hand, at higher heating rates the 2nd and 3rd peaks are more separated from the 1st peak, because their activation energies are higher, and hence the composite peak temperature becomes associated principally with the 1st peak, and hence with a lower activation energy.

Considering in more detail the activation energies for the various peaks indicated in Table 2, we note the following characteristics. The significantly higher activation energies for both the 2nd and 3rd peaks in comparison with that for the 1st peak, is consistent with their assignment as homopolymerisation reactions. The 3rd peak in particular has a very high activation energy, which would be anticipated for a thermally catalysed homopolymerisation reaction. For the 2nd peak, attributed here to an extra-gallery homopolymerisation reaction catalysed by the onium ion of the organically modified MMT, the activation energy is somewhat lower than that for the 3rd peak, and there is a noticeable decrease in the activation energy with increasing MMT content, consistent with a catalytic effect of the MMT, as has been noted before [22, 23].

After determining the activation energies, the kinetic exponents m and n in Equation (3) for the 1st peak, which is a combination of the epoxy-amine cross-linking reaction and the intra-gallery homopolymerisation reaction, can be evaluated by Malek's method [32] using the TAS software. The average values for these parameters are included in Table 2. Typically, m must be less than 1 and the sum of the reaction orders ($m+n$) should be around 2 or 3, conditions which are met by these results. It is interesting, however, to compare these values with those found for the isothermal cure of both the same TGAP/DDS/MMT system and the TGAP/DDS system without any clay [23]. For the former system, containing 5 wt% MMT, for which the epoxy-amine cross-linking reaction could be deconvoluted from the rapid intra-gallery homopolymerisation reaction, there was some variation of the values of the

parameters m and n depending on the isothermal cure temperature, the average values being $m = 0.6 \pm 0.2$ and $n = 2.1 \pm 0.4$, while for the latter system, without clay, the values were $m = 0.8$ and $n = 2.6$ approximately. The isothermal cure of the TGAP/DDS system is therefore seen to be highly autocatalytic, which can be understood in terms of the production of secondary amines by the reaction of the epoxy with primary amines. In the TGAP/DDS/MMT system, on the other hand, the isothermal cross-linking reaction appears to be less autocatalytic, which we might infer to be an effect of the presence of the clay. For the non-isothermal cure of this TGAP/DDS/MMT system, for which the results are presented in Table 2, the further reduction in the values of m and n for the 1st reaction, which is attributed to the combination of the epoxy-amine cross-linking reaction in the presence of clay and the intra-gallery homopolymerisation reaction, is consistent with this scenario.

4.4. Nanostructural analysis

An improvement in the degree of exfoliation of the nanostructure of the cured nanocomposite can be achieved by promoting the intra-gallery homopolymerisation reaction such that it occurs before the extra-gallery cross-linking reaction. This was shown clearly in earlier work with this same TGAP/DDS/MMT system [22, 23], where for isothermal cure the intra-gallery reaction at least partially preceded the epoxy-amine cross-linking reaction. In contrast, for the isothermal cure of PLS nanocomposites based upon DGEBA epoxy, the occurrence of the intra-gallery homopolymerisation reaction after, rather than before, the cross-linking reaction results in a very poorly exfoliated nanocomposite [17]. During the non-isothermal cure of the system studied here, a composite peak appears for which the 1st peak represents the contribution from the combination of the TGAP-amine cross-linking reaction and the intra-gallery homopolymerisation reaction catalysed by the onium ion of the modified MMT, both reactions occurring simultaneously. As this composite peak cannot be deconvoluted into the separate contributions of the epoxy-amine reaction and the homopolymerisation reaction, it is not clear from the reaction kinetics how the nanostructure might develop. Accordingly, nanostructural characterisation is required in order to identify whether or not a high degree of exfoliation is obtained for this system when

it is cured non-isothermally. We recall that, from a consideration of the effect of the clay content on the heat of reaction for the 1st peak, shown in Table 1, it was concluded that the greatest amount of intra-gallery reaction occurs for the sample containing 10 wt% MMT. Consequently, we examine by SAXS and TEM the nanostructure of non-isothermally cured samples containing 10 wt% MMT. The SAXS diffractogram is shown in Figure 9, which should be compared with the scattering observed for the organically modified MMT alone, which gives a marked peak at an angle of 4.2° corresponding to a d-spacing of 2.1 nm [16], and for the same nanocomposite systems cured isothermally [23], for which the diffractograms were qualitatively identical to that shown in Figure 9 for the non-isothermally cured sample. In Figure 9 there remains no evidence of the strong scattering of the MMT; instead it can be seen that, after the initial rapid fall corresponding to the background scattering, there are no scattering peaks evident within the range of angles covered here, implying that there is no regular layer stacking with a d-spacing less than about 8 nm. The same observation, namely the lack of scattering peaks in the low angle range, was also made for the nanocomposite systems with 2 and 5 wt% clay contents; the diffractograms for these samples were qualitatively identical to that in Figure 9, the only difference being in the intensity, which depends on the clay content. These non-isothermally cured samples would therefore appear to be exfoliated, but this conclusion must be corroborated by TEM observations. The TEM micrographs are shown in Figure 10, at various magnifications. The lowest magnification can be seen in Figures 10a and 10b, where portions

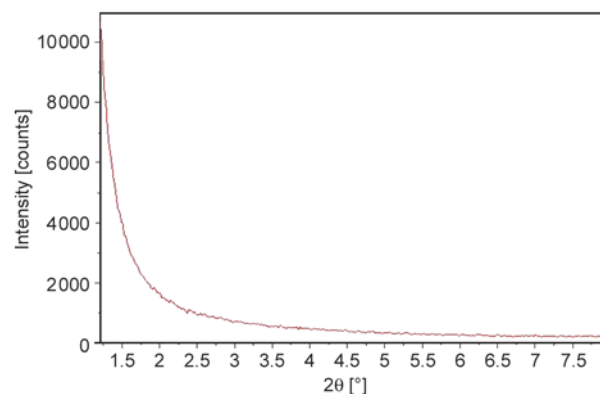


Figure 9. SAXS diffractogram for the TGAP/DDS/MMT (10 wt%) sample cured non-isothermally at $10^\circ\text{C}/\text{min}$

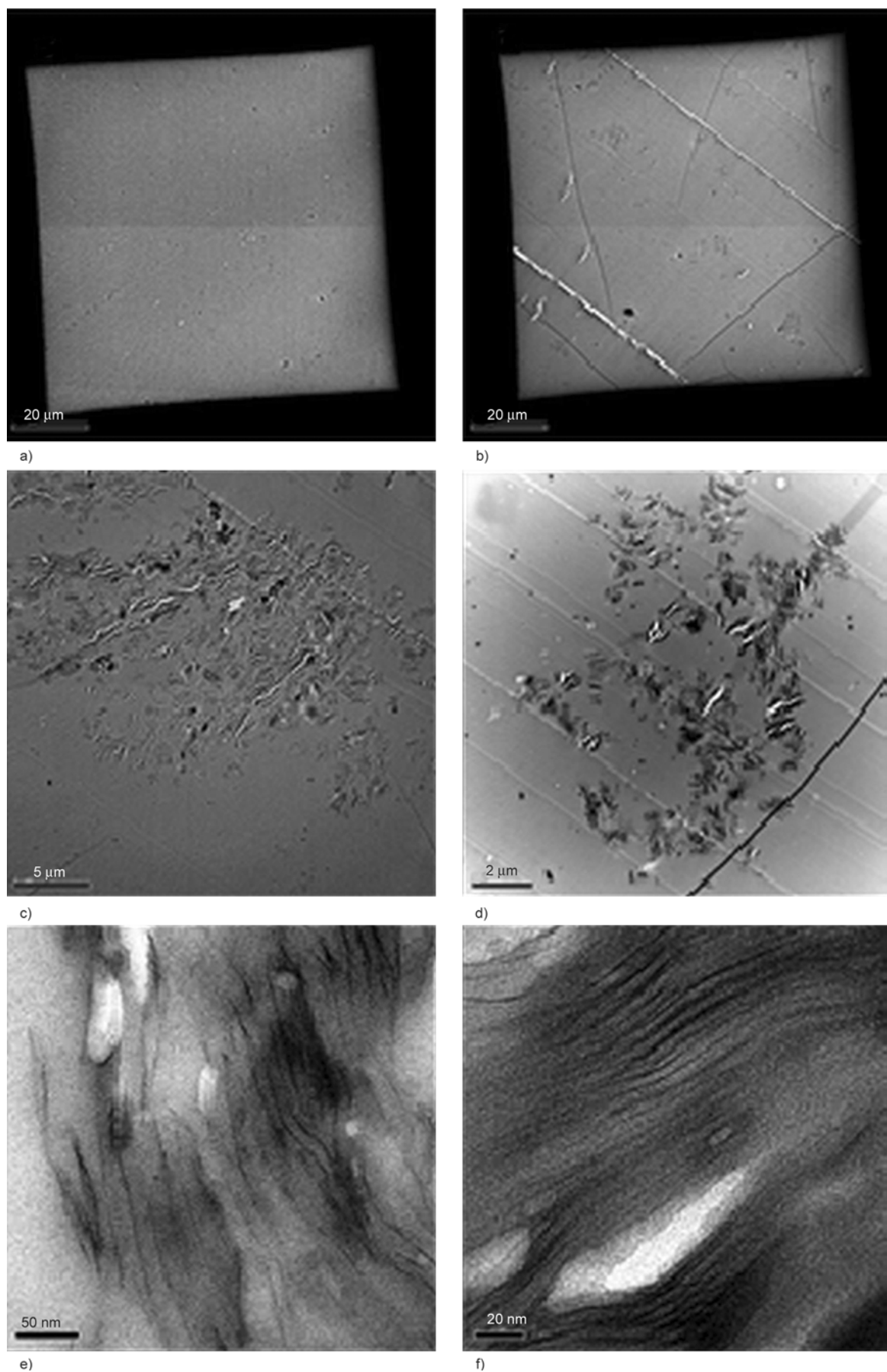


Figure 10. TEM images for the TGAP/DDS/MMT (10 wt%) system cured non-isothermally at 10°C/min. The scale bars are: (a) 20 μm; (b) 20 μm; (c) 5 μm; (d) 2 μm; (e) 50 nm; (f) 20 nm.

of two different ultra-microtomed sections of the same sample are each framed by a single grid of the support; these images, which are typical of the whole sample, indicate that in some areas there are no clay agglomerations visible (Figure 10a), while in other areas a number of clay agglomerations can be seen (Figure 10b), the largest here being between 5 and 10 μm in size, but in other areas some agglomerations may be as large as 20 to 25 μm in size. At higher magnifications (Figures 10c and 10d), typical agglomerations are seen to be composed of ‘islands’ with a relatively high density of clay layers, these ‘islands’ being separated and surrounded by the epoxy matrix, presumably containing well distributed and exfoliated clay layers. Any one of these ‘islands’, at even higher magnification, such as that shown in Figure 10e, can be seen to consist of a number of clay layers separated by distances of, typically, between 10 and 20 nm, which represents a significant degree of exfoliation. Nevertheless, there are regions in which some clay layers retain their original layer stacking, albeit with an increased layer separation. Figure 10f shows one such region, where many clay layers can be seen in register, with a spacing of only 4 to 5 nm between them; this region clearly does not represent a well exfoliated nanostructure. Nevertheless, the overall nanostructure evident from these TEM micrographs is similar to that observed for the isothermal cure of the same nanocomposite system [23]. We infer from this that the combination of the epoxy-amine cross-linking reaction and the intra-gallery homopolymerisation reaction which constitutes the 1st peak in the non-isothermal cure of the TGAP/DDS/MMT system retains the relationship between these two reactions that was evident in the isothermal cure, namely that the intra-gallery reaction is not significantly inhibited by the epoxy-amine cross-linking reaction in the extra-gallery regions.

Although only the sample with 10 wt% clay content has been studied here by TEM, as it was expected to give the greatest amount of intra-gallery reaction, we believe that the similarity of nanostructure evidenced by TEM between isothermally and non-isothermally cured samples could be extended also to the lower clay contents of 2 and 5 wt%. We base this on the SAXS results, which were obtained for all three clay contents, and which show that in all cases there is no indication of any diffraction peak in the low angle range, as well as on the following argument.

In many ways, the 10 wt% sample can be considered to be the most ‘problematic’, and hence a good degree of exfoliation would be anticipated for the 2 and 5 wt% samples if it is, as shown in Figures 9 and 10, present in the 10 wt% sample. The reason for this is that the initial dispersion of the clay in the epoxy is an important factor in the nanostructure development, and this dispersion improves as the clay content decreases. If there are significant agglomerations present, then the epoxy cannot penetrate to the clay in the heart of these agglomerations, and hence the intra-gallery reaction will not occur there. Figure 10 shows that some agglomerations clearly remain, but they are not nearly as large as in some other epoxy-clay systems, and their effect is apparently not to inhibit the intra-gallery homopolymerisation reaction, inasmuch as Table 1 shows that the heat of reaction decreases significantly for the 10 wt% sample (as a result of homopolymerisation having a lower heat of reaction) while Figure 9 shows that there is no layer stacking that would occur if the epoxy could not enter the galleries. It is concluded from this that if the relative rates of intra- and extra-gallery reactions for the 10 wt% sample are such that the latter does not inhibit the former, then the same would be true, and even more so, for the lower clay contents of 2 and 5 wt%.

5. Conclusions

In the non-isothermal cure of the TGAP/DDS/MMT system, the composite curve can be deconvoluted into three separate peaks corresponding to three different reactions, in contrast to isothermal cure for which there are only two contributions. These three peaks are: (i) a combination of the epoxy-amine cross-linking reaction and an intra-gallery homopolymerisation reaction; (ii) an extra-gallery homopolymerisation reaction which is catalysed by the organically modified MMT; and (iii) another extra-gallery homopolymerisation reaction, which is catalysed by tertiary amines. But the important distinction between the isothermal and non-isothermal cure kinetics is that, for non-isothermal cure, the intra-gallery reaction occurs concurrently with the epoxy-amine cross-linking reaction taking place in the extra-gallery regions, in contrast to isothermal cure for which the epoxy-amine cross-linking reaction takes place after the intra-gallery reaction. This distinction between the two cure schedules has been related to differences in the kinetics of isothermal

and non-isothermal cure. Despite these differences between the isothermal and non-isothermal cure kinetics, however, it appears that the final nanostructure resulting from the two cure schedules is very similar when examined by SAXS and TEM. Just as for isothermal cure, no scattering peak can be detected by SAXS for the non-isothermally cured nanocomposites. Nevertheless, the TEM images show, similarly to the isothermally cured samples, the existence of some clay agglomerations which consist of a number of clay layers with a d-spacing typically in the range from 10 to 20 nm. Hence, the final nanostructure presents a good quality of exfoliation, similar to that observed previously for samples which were cured isothermally. This implies that the intra-gallery homopolymerisation reaction, which is a necessary stage in the exfoliation process, is not significantly inhibited by the epoxy-amine cross-linking reaction occurring simultaneously in the extra-gallery regions.

Acknowledgements

The authors are grateful to Huntsman Corporation for the epoxy resin and curing agent and to Nanocor Inc. for the organically modified clay. This work was supported financially by MINECO Projects MAT2011-27039-C03 and MAT2014-53706-C3-3-R. F.S. is grateful for a grant from the Agència de Gestió d'Ajuts Universitaris i de Recerca (AGAUR), FI-DGR 2011.

References

- [1] LeBaron P. C., Wang Z., Pinnavaia T. J.: Polymer-layered silicate nanocomposites: An overview. *Applied Clay Science*, **15**, 11–29 (1999). DOI: [10.1016/S0169-1317\(99\)00017-4](https://doi.org/10.1016/S0169-1317(99)00017-4)
- [2] Alexandre M., Dubois P.: Polymer-layered silicate nanocomposites: Preparation, properties and uses of a new class of materials. *Materials Science and Engineering R: Reports*, **28**, 1–63 (2000). DOI: [10.1016/S0927-796X\(00\)00012-7](https://doi.org/10.1016/S0927-796X(00)00012-7)
- [3] Ray S. S., Okamoto M.: Polymer/layered silicate nanocomposites: A review from preparation to processing. *Progress in Polymer Science*, **28**, 1539–1641 (2003). DOI: [10.1016/j.progpolymsci.2003.08.002](https://doi.org/10.1016/j.progpolymsci.2003.08.002)
- [4] Becker O., Simon G. P., Dusek K.: Epoxy layered silicate nanocomposites. *Advances in Polymer Science*, **179**, 29–82 (2005). DOI: [10.1007/b107204](https://doi.org/10.1007/b107204)
- [5] Karak N.: Polymer (epoxy) clay nanocomposites. *Journal of Polymer Materials*, **23**, 1–20 (2006).
- [6] Hussain F., Hojjati M., Okamoto M., Gorga R. E.: Review article: Polymer-matrix nanocomposites, processing, manufacturing, and application: An overview. *Journal of Composite Materials*, **40**, 1511–1575 (2006). DOI: [10.1177/0021998306067321](https://doi.org/10.1177/0021998306067321)
- [7] Pavlidou S., Papaspyrides C. D.: A review on polymer-layered silicate nanocomposites. *Progress in Polymer Science*, **33**, 1119–1198 (2008). DOI: [10.1016/j.progpolymsci.2008.07.008](https://doi.org/10.1016/j.progpolymsci.2008.07.008)
- [8] Wang M. S., Pinnavaia T. J.: Clay-polymer nanocomposites formed from acidic derivatives of montmorillonite and an epoxy resin. *Chemistry of Materials*, **6**, 468–474 (1994). DOI: [10.1021/cm00040a022](https://doi.org/10.1021/cm00040a022)
- [9] Butzloff P., D'Souza N. A., Golden T. D., Garrett D.: Epoxy + montmorillonite nanocomposite: Effect of composition on reaction kinetics. *Polymer Engineering and Science*, **41**, 1794–1802 (2001). DOI: [10.1002/pen.10876](https://doi.org/10.1002/pen.10876)
- [10] Kornmann X., Lindberg H., Berglund L. A.: Synthesis of epoxy-clay nanocomposites. Influence of the nature of the curing agent on structure. *Polymer*, **42**, 4493–4499 (2001). DOI: [10.1016/S0032-3861\(00\)00801-6](https://doi.org/10.1016/S0032-3861(00)00801-6)
- [11] Xu W., Bao S., Shen S., Wang W., Hang G., He P.: Differential scanning calorimetry study on the curing behaviour of epoxy resin/diethylenetriamine/organic montmorillonite nanocomposite. *Journal of Polymer Science Part B: Polymer Physics*, **41**, 378–386 (2003). DOI: [10.1002/polb.10365](https://doi.org/10.1002/polb.10365)
- [12] Becker O., Simon G. P., Varley R. J., Halley P. J.: Layered silicate nanocomposites based on various high-functionality epoxy resins: The influence of an organoclay on resin cure. *Polymer Engineering and Science*, **43**, 850–862 (2003). DOI: [10.1002/pen.10070](https://doi.org/10.1002/pen.10070)
- [13] Chen C., Curliss D.: Preparation, characterization, and nanostructural evolution of epoxy nanocomposites. *Journal of Applied Polymer Science*, **90**, 2276–2287 (2003). DOI: [10.1002/app.12901](https://doi.org/10.1002/app.12901)
- [14] Ton-That M-T., Ngo T-D., Ding P., Fang G., Cole K. C., Hoa S. V.: Epoxy nanocomposites: Analysis and kinetics of cure. *Polymer Engineering and Science*, **44**, 1132–1141 (2004). DOI: [10.1002/pen.20106](https://doi.org/10.1002/pen.20106)
- [15] Ivankovic M., Brnardic I., Ivankovic H., Mencer H. J.: DSC study of the cure kinetics during nanocomposite formation: Epoxy/poly(oxypropylene) diamine/organically modified montmorillonite system. *Journal of Applied Polymer Science*, **99**, 550–557 (2006). DOI: [10.1002/app.22488](https://doi.org/10.1002/app.22488)
- [16] Román F., Montserrat S., Hutchinson J. M.: On the effect of montmorillonite in the curing reaction of epoxy nanocomposites. *Journal of Thermal Analysis and Calorimetry*, **87**, 113–118 (2007). DOI: [10.1007/s10973-006-7830-9](https://doi.org/10.1007/s10973-006-7830-9)

- [17] Montserrat S., Román F., Hutchinson J. M., Campos L.: Analysis of the cure of epoxy based layered silicate nanocomposites: Reaction kinetics and nanostructure development. *Journal of Applied Polymer Science*, **108**, 923–938 (2008). DOI: [10.1002/app.27297](https://doi.org/10.1002/app.27297)
- [18] Pustkova P., Hutchinson J. M., Román F., Montserrat S.: Homopolymerization effects in polymer layered silicate nanocomposites based upon epoxy resin: Implications for exfoliation. *Journal of Applied Polymer Science*, **114**, 1040–1047 (2009). DOI: [10.1002/app.30697](https://doi.org/10.1002/app.30697)
- [19] Xu Y., Peng H., Wang X., Su S.: Comparative study of different polymerically-modified clays on curing reaction and thermal properties of epoxy resin. *Thermochimica Acta*, **516**, 13–18 (2011). DOI: [10.1016/j.tca.2011.01.004](https://doi.org/10.1016/j.tca.2011.01.004)
- [20] Román F., Calventus Y., Colomer P., Hutchinson J. M.: Identification of nanostructural development in epoxy polymer layered silicate nanocomposites from the interpretation of differential scanning calorimetry and dielectric spectroscopy. *Thermochimica Acta*, **541**, 76–85 (2012). DOI: [10.1016/j.tca.2012.05.001](https://doi.org/10.1016/j.tca.2012.05.001)
- [21] Becker O., Cheng Y-B., Varley R. J., Simon G. P.: Layered silicate nanocomposites based on various high-functionality epoxy resins: The influence of cure temperature on morphology, mechanical properties, and free volume. *Macromolecules*, **36**, 1616–1625 (2003). DOI: [10.1021/ma0213448](https://doi.org/10.1021/ma0213448)
- [22] Hutchinson J. M., Shiravand F., Calventus Y.: Intra- and extra-gallery reactions in tri-functional epoxy polymer layered silicate nanocomposites. *Journal of Applied Polymer Science*, **128**, 2961–2970 (2013). DOI: [10.1002/app.38452](https://doi.org/10.1002/app.38452)
- [23] Shiravand F., Hutchinson J. M., Calventus Y.: Influence of the isothermal cure temperature on the nanostructure and thermal properties of an epoxy layered silicate nanocomposite. *Polymer Engineering and Science*, **54**, 51–58 (2014). DOI: [10.1002/pen.23540](https://doi.org/10.1002/pen.23540)
- [24] Hutchinson J. M., Shiravand F., Calventus Y., Fraga I.: Isothermal and non-isothermal cure of a tri-functional epoxy resin (TGAP): A stochastic TMDSC study. *Thermochimica Acta*, **529**, 14–21 (2012). DOI: [10.1016/j.tca.2011.11.008](https://doi.org/10.1016/j.tca.2011.11.008)
- [25] Vyazovkin S., Burnham A. K., Criado J. M., Pérez-Maqueda L. A., Popescu C., Sbirrazzuoli N.: ICTAC Kinetics Committee recommendations for performing kinetic computations on thermal analysis data. *Thermochimica Acta*, **520**, 1–19 (2011). DOI: [10.1016/j.tca.2011.03.034](https://doi.org/10.1016/j.tca.2011.03.034)
- [26] Starink M. J.: The determination of activation energy from linear heating rate experiments: A comparison of the accuracy of isoconversion methods. *Thermochimica Acta*, **404**, 163–176 (2003). DOI: [10.1016/S0040-6031\(03\)00144-8](https://doi.org/10.1016/S0040-6031(03)00144-8)
- [27] Ozawa T.: A new method of analyzing thermogravimetric data. *Bulletin of the Chemical Society of Japan*, **38**, 1881–1886 (1965). DOI: [10.1246/bcsj.38.1881](https://doi.org/10.1246/bcsj.38.1881)
- [28] Vyazovkin S.: Evaluation of activation energy of thermally stimulated solid-state reactions under arbitrary variation of temperature. *Journal of Computational Chemistry*, **18**, 393–402 (1997). DOI: [10.1002/\(SICI\)1096-987X\(199702\)18:3<393::AID-JCC9>3.0.CO;2-P](https://doi.org/10.1002/(SICI)1096-987X(199702)18:3<393::AID-JCC9>3.0.CO;2-P)
- [29] Vyazovkin S.: Modification of the integral isoconversional method to account for variation in the activation energy. *Journal of Computational Chemistry*, **22**, 178–183 (2001). DOI: [10.1002/1096-987X\(20010130\)22:2<178::AID-JCC5>3.0.CO;2-#](https://doi.org/10.1002/1096-987X(20010130)22:2<178::AID-JCC5>3.0.CO;2-#)
- [30] Kissinger H. E.: Variation of peak temperature with heating rate in differential thermal analysis. *Journal of Research of the National Bureau of Standards*, **57**, 217–221 (1956).
- [31] Kissinger H. E.: Reaction kinetics in differential thermal analysis. *Analytical Chemistry*, **29**, 1702–1706 (1957). DOI: [10.1021/ac60131a045](https://doi.org/10.1021/ac60131a045)
- [32] Málek J.: The kinetic analysis of non-isothermal data. *Thermochimica Acta*, **200**, 257–269 (1992). DOI: [10.1016/0040-6031\(92\)85118-F](https://doi.org/10.1016/0040-6031(92)85118-F)
- [33] Frigione M., Calò E.: Influence of an hyperbranched aliphatic polyester on the cure kinetic of a trifunctional epoxy resin. *Journal of Applied Polymer Science*, **107**, 1744–1758 (2008). DOI: [10.1002/app.27277](https://doi.org/10.1002/app.27277)
- [34] Varley R. J., Hodgkin J. H., Hawthorne D. G., Simon G. P.: Toughening of a trifunctional epoxy system. II. Thermal characterization of epoxy/amine cure. *Journal of Applied Polymer Science*, **60**, 2251–2263 (1996). DOI: [10.1002/\(SICI\)1097-4628\(19960620\)60:12<2251::AID-APP24>3.0.CO;2-8](https://doi.org/10.1002/(SICI)1097-4628(19960620)60:12<2251::AID-APP24>3.0.CO;2-8)
- [35] Smith I. T.: The mechanism of the crosslinking of epoxide resins by amines. *Polymer*, **2**, 95–108 (1961). DOI: [10.1016/0032-3861\(61\)90010-6](https://doi.org/10.1016/0032-3861(61)90010-6)
- [36] Ryan M. E., Dutta A.: Kinetics of epoxy cure: A rapid technique for kinetic parameter estimation. *Polymer*, **20**, 203–206 (1979). DOI: [10.1016/0032-3861\(79\)90222-2](https://doi.org/10.1016/0032-3861(79)90222-2)
- [37] Hutchinson J. M., Montserrat S., Román F.: Nanostructure development and cure kinetics in epoxy-based PLS nanocomposites. *Journal of Nanostructured Polymers and Nanocomposites*, **4**, 13–20 (2008).
- [38] Klute C. H., Viehmann W.: Heat of polymerization of phenyl glycidyl ether and of an epoxy resin. *Journal of Applied Polymer Science*, **5**, 86–95 (1961). DOI: [10.1002/app.1961.070051313](https://doi.org/10.1002/app.1961.070051313)
- [39] Dell’Erba I. E., Williams R. J. J.: Homopolymerization of epoxy monomers initiated by 4-(dimethylamino)pyridine. *Polymer Engineering and Science*, **46**, 351–359 (2006). DOI: [10.1002/pen.20468](https://doi.org/10.1002/pen.20468)

Liquid crystalline polymer nanocomposites reinforced with in-situ reduced graphene oxide

D. Pedrazzoli¹, A. Dorigato^{1*}, T. Conti¹, L. Vanzetti², M. Bersani², A. Pegoretti¹

¹University of Trento, Department of Industrial Engineering and INSTM Research Unit, Via Sommarive 9, 38123 Povo (Trento), Italy

²MiNALab Laboratory, Bruno Kessler Foundation, Via Sommarive 18, 38123 Povo (Trento), Italy

Received 1 December 2014; accepted in revised form 25 February 2015

Abstract. In this work liquid-crystalline polymer (LCP) nanocomposites reinforced with *in-situ* reduced graphene oxide are investigated. Graphene oxide (GO) was first synthesized by the Hummers method, and the kinetics of its thermal reduction was assessed. GO layers were then homogeneously dispersed in a thermotropic liquid crystalline polymer matrix (Vectran[®]), and an *in-situ* thermal reduction of GO into reduced graphene oxide (rGO) was performed. Even at low rGO amount, the resulting nanocomposites exhibited an enhancement of both the mechanical properties and the thermal stability. Improvements of the creep stability and of the thermo-mechanical behavior were also observed upon nanofiller incorporation. Furthermore, *in-situ* thermal reduction of the insulating GO into the more electrically conductive rGO led to an important surface resistivity decrease in the nanofilled samples.

Keywords: nanocomposites, mechanical properties, liquid-crystalline polymer

1. Introduction

Since its discovery in 2004, graphene, a one-atom-thick planar sheet of sp²-bonded carbon atoms densely packed in a honeycomb crystal lattice, has generated intensive research activity in several areas of science and engineering due to its unique combination of superior mechanical, thermal and electrical properties [1, 2]. Graphene is a very promising filler for the preparation of polymer nanocomposites, with enhanced mechanical [3, 4] and functional [5–9] properties. On the other hand, dispersion of graphene layers in a polymer matrix is still a difficult task [10]. Graphene oxide (GO) has recently attracted much attention due to its peculiar structure and properties which favor its dispersion in a wide variety of polymeric matrices, including polar polymers [11–13]. From a structural point of view, GO consists of a planar sheet of covalently bonded carbon

atoms bearing various oxygen functional groups (e.g. hydroxyl, epoxide, and carbonyl groups) making it hydrophilic and easily dispersible in water as single sheets, to form stable colloidal suspensions [14–17]. Therefore the dispersion of GO in synthetic polymer matrices is an easier task since intercalated or fully exfoliated structures can be obtained [18–20]. GO can be reduced into graphene through chemical (e.g. by using hydrazine or hydrazine derivatives [21–23]) or thermal processes [24–27]. At the actual state of the art, the easiest way to produce bulk quantities of graphene is based on the reduction of GO [28–30]. Thermal reduction of GO has been reported to be very effective in restoring the graphene structure [31, 32], but elevated temperatures (i.e. from 300 to 1000°C) are usually required to achieve a complete GO reduction in a reasonable time. When thermally stable polymer matrices are

*Corresponding author, e-mail: andrea.dorigato@ing.unitn.it

considered, an *in-situ* thermal reduction of GO nanoplatelets within the polymer matrix can be performed [24, 33, 34]. At this aim, a liquid crystalline polymer (LCP) matrix, known as Vectran[®], was chosen for the present research, because of its extremely high thermal stability and excellent mechanical properties [35].

In particular, thermotropic main chain LCP copolyesters represent a class of high-tech polymers which combine high mechanical performances with low density, resulting in outstanding specific properties [35–38]. Their typical applications include electronic devices, fiber optic coupling discs, automotive components, and sport equipment. Because the crystalline order between LCP polymer chains is maintained even at elevated temperatures, it is of great interest to determine how GO layers will disperse in LCP, and how the mechanical properties and electrical conductivity of the resulting materials will be modified. To the best of our knowledge, only limited studies are available on the effect of carbonaceous nanofillers on the physical and mechanical properties of LCPs [39–42].

Noteworthy, multifunctional materials such as LCP nanocomposites offer a great potential to enhance not only the mechanical and thermal properties with respect to the unmodified polymer, but also functional properties including high electrical and thermal conductivity, providing the opportunity to be used in different fields such as automotive, electronic packaging, aerospace, energy storage, etc. [43].

Therefore, the objective of this research is to prepare Vectran-based nanocomposites reinforced with *in-situ* thermally reduced graphene oxide, and to assess the effect played by filler incorporation on the thermal, mechanical and electrical properties of the resulting materials.

2. Experimental part

2.1. Materials

Commercially available Vectran[®] NT fibers having a linear density of 750 denier and 150 filaments/yarn and a circular cross-section with an average diameter of $25.5 \pm 2.1 \mu\text{m}$ [38] were provided by Kuraray America Inc. (Fort Mill, USA). This special type of LCP is a thermotropic copolyester obtained by polycondensation of p-Hydroxybenzoic acid (HBA) and 6-hydroxy-2-naphthoic acid (HNA) in the molar ratio 73:27 (Figure 1). Graphite powder (particle size $<20 \mu\text{m}$) was purchased from Sigma-Aldrich.

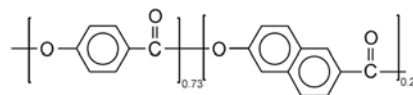


Figure 1. Chemical structure of Vectran NT[®] repeating unit

All other reagents with analytical grade purity were used without further treatments.

2.2. Sample preparation

GO was obtained from graphite powder by a modified Hummers method [44, 45]. GO powder was then dispersed in distilled water by sonication (Hielscher UP400S, 30 minutes) and centrifuged at 4000 rpm for 15 min in order to remove unexfoliated graphite oxide and process residuals. A brownish homogeneous suspension of GO with concentration up to 10 mg/mL was obtained.

Vectran fibers were first dried in a vacuum oven at 80°C for 1 h. and then solved in a mixture (70/30) of chloroform and pentafluorophenol. A solution with a polymer concentration of 1 wt% was obtained after stirring for 24 h. GO was dispersed in chloroform by sonication for 30 min at a concentration lower than $1.2 \text{ mg} \cdot \text{mL}^{-1}$ (as determined by thermogravimetric analysis). Vectran/GO solutions were then prepared by mixing the chloroform/GO suspension with a solution of Vectran fibers in chloroform/pentafluorophenol by stirring for 15 min and subsequent bath sonication (Elma Transsonic T460/H, Singen-Germany) for 15 min. The solution was then cast and left at room temperature for 24 h to let the chloroform evaporate. Finally, the remaining solution was mixed with dichloromethane for 24 h at room temperature with subsequent drying in vacuum at 80°C for 24 h. This final step was necessary to remove pentafluorophenol and chloroform residuals. In order to accomplish the *in-situ* thermal reduction of GO into reduced GO (rGO), a thermal treatment was performed on the Vectran nanocomposites in a vacuum oven (pressure of 25 mbar) at 290°C (heating rate of $1.5^\circ\text{C} \cdot \text{min}^{-1}$) for 4 h. Thin films of Vectran nanocomposites were then obtained by a three-step thermoforming process by using a Carver hot press (Wabash, USA). Specifically, the material was first heated on a polytetrafluoroethylene mold at 320°C (heating rate of $5^\circ\text{C} \cdot \text{min}^{-1}$) and kept at this temperature for 5 min. During the second step, forming of the nanocomposite films was performed by applying a pressure of 0.2 MPa for 5 min. The materials were then cooled down to 200°C at a cooling

rate of $5^{\circ}\text{C}\cdot\text{min}^{-1}$ and were kept at this temperature for 15 minutes, in order to obtain a complete solidification of the material. After removing the applied pressure, a further annealing was performed at 290°C for 3.5 h (heating rate of $5^{\circ}\text{C}\cdot\text{min}^{-1}$), in order to relax the residual stresses accumulated during the compression molding stage and to favor a slow recrystallization of the samples [40]. In this way, nanocomposite films with thickness of about $250\ \mu\text{m}$ were produced with an rGO content of 1, 3 and 5 wt%. The unfilled matrix was denoted as VECTRAN, while nanocomposites were designated indicating the matrix and the filler amount. For instance, a sample filled with 5 wt% of rGO was indicated as VECTRAN_rGO5%.

In order to investigate the kinetics of the filler reduction, neat GO films with a thickness of about $43\ \mu\text{m}$ were also obtained by casting a water/GO suspension and drying it at room temperature under vacuum for 24 h. The resulting films were then thermally treated at various temperatures and for different times under vacuum at a heating rate of $1.5^{\circ}\text{C}\cdot\text{min}^{-1}$. Untreated GO was simply indicated as GO, while thermally treated samples were denoted indicating the treatment temperature and duration. For instance, GO_300°C×4 h denotes a GO film treated at 300°C for 4 h.

2.3. Experimental methodologies

X-ray diffraction (XRD) analyses were performed on the GO films by a Rigaku® 3D Max X-ray diffractometer (Kent, England) in Bragg-Brentano geometry operating at the $\text{Cu K}\alpha_1$ wavelength ($0.154059\ \text{nm}$), applying a voltage of 40 kV and a current of 30 mA. The samples were scanned in a 2θ range between 5 and 45° at a 2θ step of 0.05° .

X-ray photoelectron spectroscopy (XPS) analyses were carried out on GO films by using a XPS ESCA 200 Scienta spectrometer (VG Scienta, Uppsala, Sweden), adopting a monochromatic $\text{AlK}\alpha$ radiation ($h\nu = 1486.6\ \text{eV}$) with emission angle of 90° and at a pressure of 10–10 mbar.

Electrical resistance was assessed under the four-point configuration according to ASTM D4496-04 standard, in order to evaluate the surface resistivity of untreated GO and rGO films thermally treated at 180, 220, 260 and 300°C for 4 h. Electrical measurements were carried out at room temperature and under vacuum applying a potential of 2 V by an electrical generator Isotech IPS 330DD (Champaign,

United States), while current and voltage were monitored through Isotech IDM67 multimeters. Surface resistivity measurements were also performed on Vectran/rGO nanocomposites in a two-point resistance configuration, by applying a voltage of 50 V through an electrometer Keithley 6517A (Cleveland, USA) and reading the resistance value after 60 s.

Thermogravimetric analysis (TGA) measurements were carried out by a thermobalance TA Instruments Q5000 (Waters LLC, New Castle, USA) at a heating rate of $5^{\circ}\text{C}\cdot\text{min}^{-1}$ from 50 to 900°C under a nitrogen flow of $25\ \text{mL}\cdot\text{min}^{-1}$ on samples of about 5 mg. Cryogenic fracture surfaces of Vectran nanocomposites were observed at various magnifications by using a field emission-scanning electron microscope (FESEM) Zeiss Supra 40 (Berlin, Germany) at acceleration voltages between 1 and 1.5 kV. Before the observation, a thin gold coating was deposited on the surface of the samples in order to minimize electrostatic charging effects.

Uniaxial tensile tests were performed with an Instron® 4502 (Norwood, USA) tensile machine, on rectangular specimens 25 mm long, 2.5 mm wide and 0.25 mm thick. Tests were carried out at a cross-head speed of $1\ \text{mm}\cdot\text{min}^{-1}$ and setting a gauge length of 10 mm. At least five specimens were tested for each sample. According to ISO 527 standard, the elastic modulus was determined as a secant value between deformation levels of 0.05 and 0.25%.

Creep tests were carried out in tensile mode on a dynamic mechanical analyzer (DMA) TA Instruments Q800 (Waters LLC, New Castle) at a constant stress (σ_0) of 4 MPa for 1 h at 30°C . Rectangular specimens, 2 mm long, 2.5 mm wide and 0.25 mm thick, were tested at a gage length of 10.4 mm. The same apparatus and testing configuration was also adopted to determine dynamic mechanical thermal analysis (DMTA) thermograms in a temperature range from -100 to 200°C , at a heating rate of $3^{\circ}\text{C}\cdot\text{min}^{-1}$ and a test frequency of 1 Hz.

3. Results and discussion

3.1. Characterization of GO and rGO

3.1.1. X-ray diffraction analyses

XRD spectra of graphite, untreated GO and rGO treated at 180 and 300°C for 4 hours are reported in Figure 2 along with fitting lines. Noteworthy, the GO sample reduced at 90°C for 4 h manifested an XRD spectrum (not reported for brevity) practically coincident with that of untested GO. Therefore, the sam-

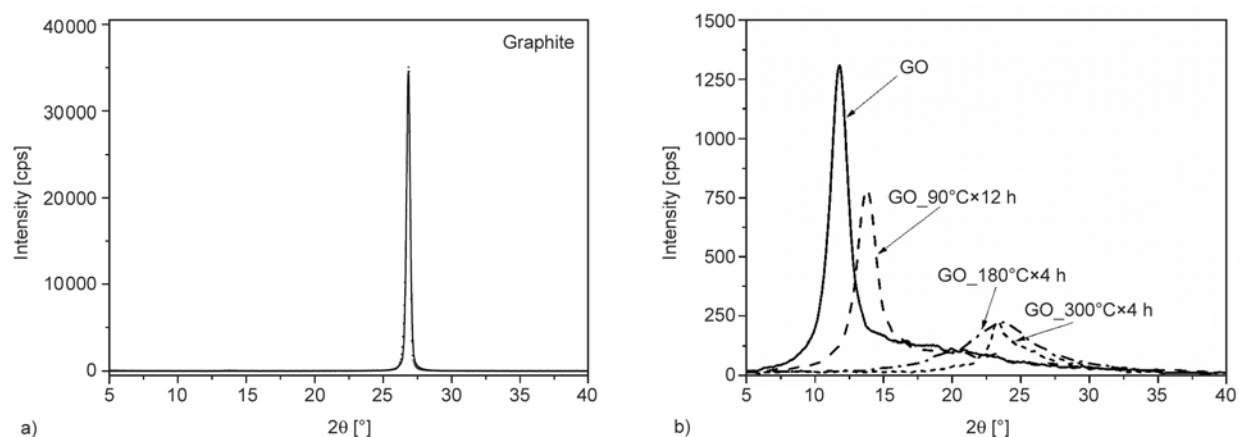


Figure 2. XRD spectra of graphite and of reduced graphene oxide: (a) graphite and (b) untreated GO, GO reduced for 4 h at 180 and 300°C. Noteworthy, the GO sample reduced at 90°C was treated for 12 h in order to obtain a significantly different XRD spectrum.

Table 1. XRD parameters of pristine graphite, untreated GO and rGO samples

Sample	d_{002}^a [Å]	D_{002}^b [Å]	N_{GP}^c [-]
Graphite	3.32	279.67	84.2
GO	7.51	55.88	7.4
GO_90°C×4 h	6.42	50.37	7.8
GO_180°C×4 h	3.69	14.48	3.9
GO_300°C×4 h	3.76	13.82	3.7

^aspacing between graphene layers.

^bsize of crystals formed by graphene layers.

^cExfoliation degree, i.e. D_{002}/d_{002} .

ple was exposed at 90°C for a longer time (12 h) in order to obtain a significantly different XRD spectrum.

The diffractogram of graphite powder shows a strong peak at $2\theta = 26.5^\circ$ (Figure 2a) which correspond to the spacing between graphene layers (i.e. (022) crystal orientation [46]). Moreover, according to Bragg's law and Scherer's equation, the distance between the graphene layers (d_{002}) and their size (D_{002}) were determined to correspond to 3.32 and 279.67 Å, respectively (Table 1). In particular, the distance between the graphene layers is in good agreement with the value commonly reported in the literature (3.35 Å), while the high value of N_{GP} evidences an extended packing of graphene layers.

GO shows an intense peak at $2\theta = 11.7^\circ$ (Figure 2b), indicating a much larger interlamellar distance and crystal size when compared to pristine graphite. However, reduced GO samples manifest a less intense peak shifted towards higher values of 2θ . In particular, the intensity and position of the peak are proportional to the temperature of treatment, indicating a progressive exfoliation of the GO occurring

upon thermal treatment, as evidenced by the decreasing N_{GP} values. Moreover, the reduced d_{002} observed for reduced GO samples can be attributed to the release of water molecules and loss of oxygen functional groups (i.e. epoxy, hydroxyl and carboxyl).

3.1.2. X-ray photoelectron spectroscopy

XPS chemical analyses were performed in order to evaluate the oxidation reduction level of films of both untreated GO and rGO thermally treated at various temperatures and annealing times. A survey and the C_{1s} and O_{1s} core levels were collected for each sample. In the used analytical conditions the sampling depth on these samples is around 10 nm.

The core lines of C_{1s} and O_{1s} are reported in Figure 3, respectively. It is possible to observe that the carbon core level lineshape of untreated sample shows three well defined peaks. The peak at higher energy corresponds to C–C/C–H bonds, the second peak, located around 287.2 eV, is related to C=O bonds and it is the more intense peak in the untreated sample. A further peak (C–O–O–H) is also present at higher energy. In the annealed samples the C_{1s} core level lineshapes present an evident modification. In fact for both reported samples the C–C/C–H around a factor 3 and peak corresponding to oxidized carbon is strongly reduced. The thermal reduction is evident for both the samples but it is more pronounced when the annealing temperature is raised up to 300°C. The O_{1s} core level spectra point out the same behavior. Specifically, the untreated sample exhibits a single peak with a characteristic energy of C=O bonds. With annealing it is possible to observe a strong intensity reduction and a peak enlargement proba-

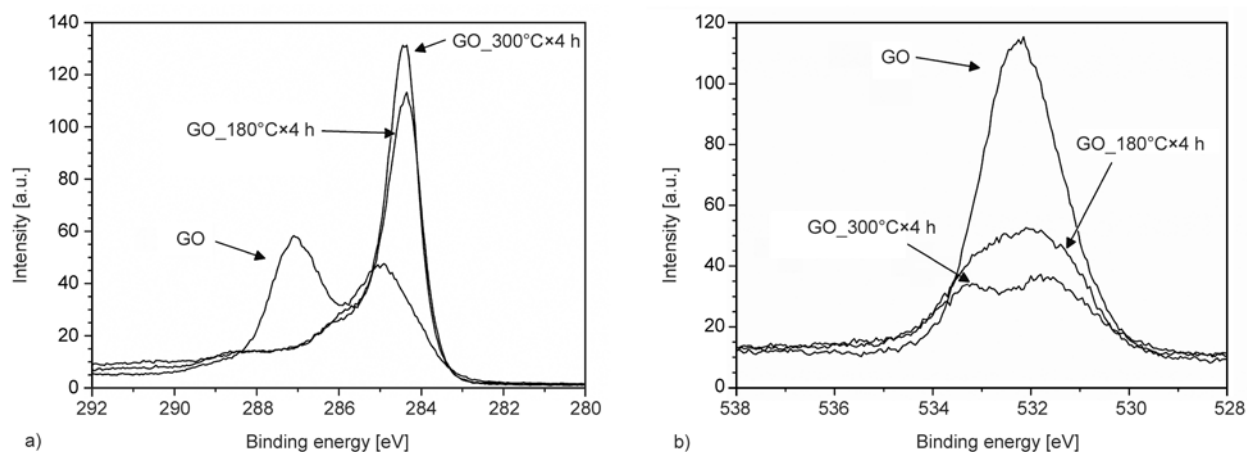


Figure 3. Comparison of core level (a) C_{1s} peak and (b) O_{1s} peak acquired during XPS analysis on untreated GO, GO reduced at 180 and 300°C for 4 h

Table 2. XPS parameters: oxygen (O) and carbon (C) content evaluated in untreated GO and GO reduced at 180 and 300°C for 4 h

Sample	O content [%]	C content [%]	C:O ratio
GO	30.7	69.3	2.26:1
GO_180°C×4 h	19.0	81.0	4.27:1
GO_300°C×4 h	13.6	86.4	6.35:1

bly due to the formation of suboxide compound. An estimation of the surface elemental composition based on XPS atomic sensitivity factors is reported in Table 2. These data confirm the progressive thermal reduction of GO with also a remarkable difference between the annealed samples.

3.1.3. Surface resistivity

Surface resistivity measurements were performed both on untreated and thermally-treated GO films to evaluate the efficacy of the thermal reduction performed for 4 h at 180, 220, 260 and 300°C, and the main results are summarized in Table 3. In accordance to the literature data [23, 27], untreated GO is characterized by a relatively high surface resistivity (i.e. $\sim 10^{12}$ Ω/sq). However, the resistivity decreases by more than ten orders of magnitude after a thermal treatment at 180°C for 4 h (Table 3), indicating

Table 3. Surface resistivity of untreated GO and GO reduced at different temperatures for 4 h

Sample	Surface resistivity [Ω/sq]
GO	$2.33 \cdot 10^{12}$
GO_180°C×4 h	$6.72 \cdot 10^1$
GO_220°C×4 h	$5.64 \cdot 10^1$
GO_260°C×4 h	$4.57 \cdot 10^1$
GO_300°C×4 h	$3.40 \cdot 10^1$

an effective removal of most of the oxidized functional groups which allows the material to re-establish the sp^2 configuration and to increase its surface conductivity [24]. At higher treatment temperatures a further slight resistivity decrease down to $\sim 3.4 \cdot 10^1$ Ω/sq can be observed.

3.1.4. Thermogravimetric analysis

The oxidation treatment of graphite introduced large amount of oxygenated moieties on lamellae surface, therefore the thermogravimetric curve of GO films (reported in Figure 4) is characterized by various degradative steps, each of them representing a specific event. A first step (S_1) occurring between 50 and 140°C is attributed to the release of moisture adsorbed on the GO surfaces. Moreover, a second step (S_2) observable in the temperature range of 140 to 200°C is characterized by the maximum degradation rate (total mass loss ~ 25 wt% for neat GO), that indicates the loss of oxygen containing functional groups (i.e. epoxy, hydroxyl and carboxyl) upon reduction. A third step (S_3) can be detected between 200 and 300°C, and can be attributed to the further loss of epoxide groups. Finally, the steps S_4 and S_5 occur in a temperature range of 300 to 560°C and 560 to 800°C, respectively, and can be attributed to the further loss of hydroxyl, carboxyl and ketone groups [47]. The TGA curve relative to GO films treated at 90°C for 12 h shows a lower mass loss during the first step due to the partial moisture evaporation occurring during the thermal treatment. Moreover, GO films treated at 180 and 300°C for 4 h evidence a significantly lower mass loss taking place upon the reduction steps S_2 and S_3 , concurrently with a reduced degradation rate, indicating that GO has been

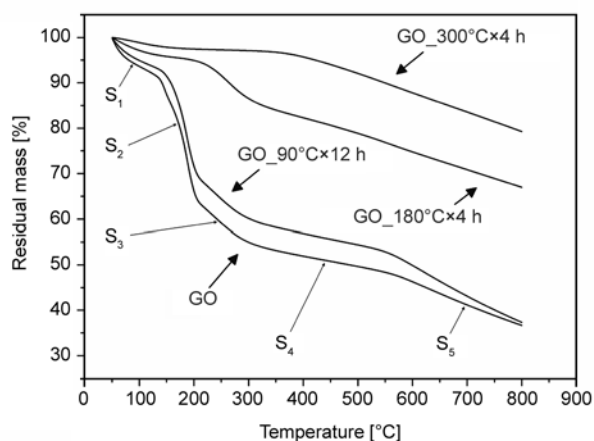


Figure 4. TGA curves of untreated GO, GO dried at 90°C for 12 h and GO reduced at 180 and 300°C for 4 h (nitrogen environment, heating rate = 5°C·min⁻¹)

reduced to a much higher extent during the previous thermal treatment. Therefore, the TGA analyses performed on GO films indicate that (i) the thermal reduction performed at temperatures as high as 180 and 300°C is able to reduce GO to a very high extent (as confirmed by the surface resistivity results presented earlier) and (ii) a thermal treatment performed on Vectran_rGO nanocomposites at around 300°C should be appropriate to greatly reduce GO and limit the matrix degradation.

3.2. Characterization of Vectran/rGO nanocomposites

3.2.1. Microstructure

SEM micrographs of the cryofractured surfaces of Vectran_rGO nanocomposites were acquired in order to assess the dispersion of GO lamellae achieved during the nanocomposite preparation. Figure 5a shows a micrograph of the unfilled matrix, evidencing the peculiar fibrillar morphology of Vectran [48, 49]. Because this morphology is preserved also when the nanofiller is present in the polymer matrix, the evaluation of the filler dispersion and distribution within the matrix is a rather difficult task for filler amount of 1 wt% (Figure 5b). However, micrometric-size structures with lamellar morphology can be recognized in the sample at filler loading of 5 wt% (Figure 5c), probably attributable to the adsorption of polymeric chains onto the planar filler surfaces.

3.2.2. Thermal degradation behavior

TGA analyses were performed in order to investigate the thermal degradation behavior both under inert and oxidative environment (nitrogen and air fluxes, respectively). According to the information reported

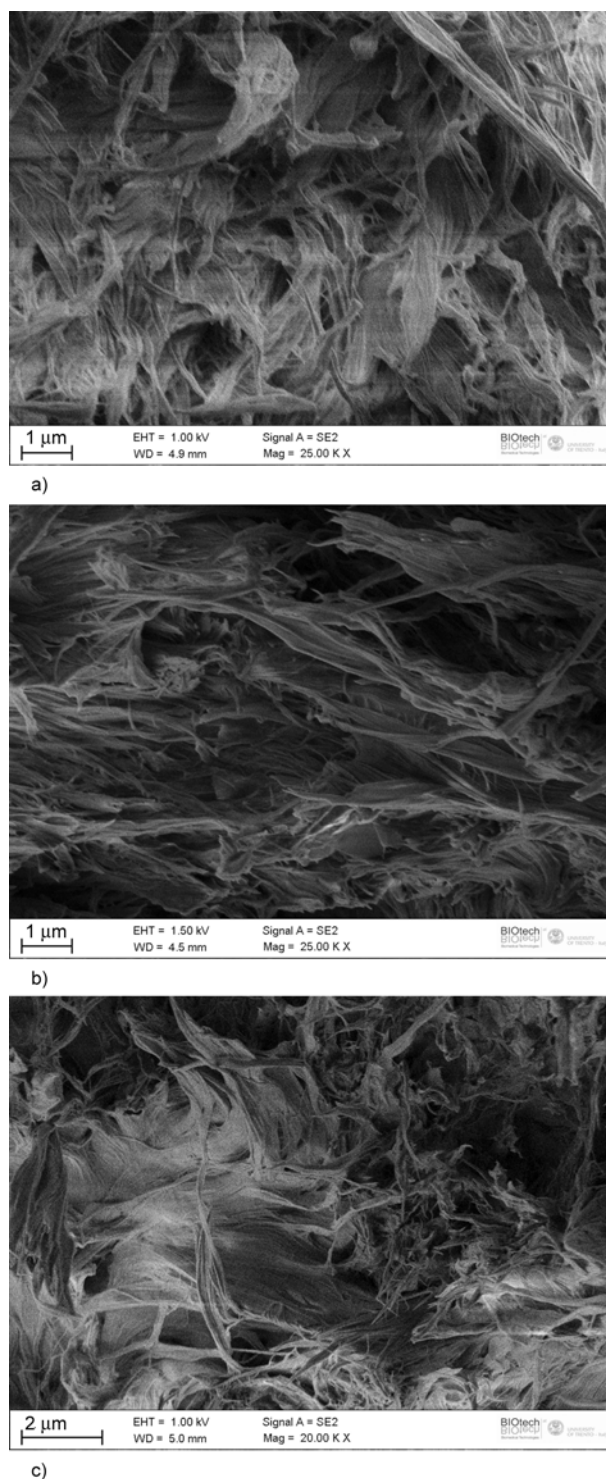


Figure 5. SEM micrographs of cryofractured surfaces of VECTRAN (a) and Vectran/rGO nanocomposites with a filler amount of (b) 1 wt%, (c) 5 wt%

in the open scientific literature, the degradation products of Vectran mostly consist of CO₂, while aromatic compounds are supposed to evolve more intensively starting from 460°C. Finally, phenolic groups, aryl ester groups and ketone groups should be released above 500°C [50]. TGA curves under inert environment (not reported for brevity) display a sin-

Table 4. TGA results of Vectran and Vectran/rGO nanocomposites (nitrogen environment, heating rate = $5^{\circ}\text{C}\cdot\text{min}^{-1}$)

Sample	$T_{d,onset}^a$ [$^{\circ}\text{C}$]	$T_{d,max}^b$ [$^{\circ}\text{C}$]	Residual mass [%]
VECTRAN	489	501	38.5
VECTRAN_rGO1%	492	502	42.9
VECTRAN_rGO3%	499	505	44.0
VECTRAN_rGO5%	498	506	44.3

^aOnset degradation temperature.^bMaximum degradation rate temperature.

gle degradation step occurring at temperatures higher than 450°C , with a shift towards higher temperature for Vectran_rGO nanocomposites. As documented in Table 4, this shift corresponds to an increase of both the onset degradation temperature and the maximum degradation rate with the filler content. Therefore, filler incorporation results in a better thermal stability of the nanocomposites. In fact, exposure to elevated temperatures may cause the formation of filler agglomerates on the surface of the molten polymer, thus creating a protective barrier that may hinder the volatilization of molecular species formed during the thermal degradation process [51]. This could be also the reason why residual mass of nano-filled samples is higher than that of neat Vectran (see Table 4). Quite differently from TGA analyses conducted in inert environment, two main mass losses can be distinguished on TGA curves under oxidative conditions (Figure 6a), characterized by a distinct peak observable on the derivative mass plot (Figure 6b). The first degradation step occurring at temperatures over 475°C is mainly due to evolution of CO_2 , while the second degradation step recorded at temperatures above 525°C is characterized by the evolution of both CO_2 and CO [50] until complete

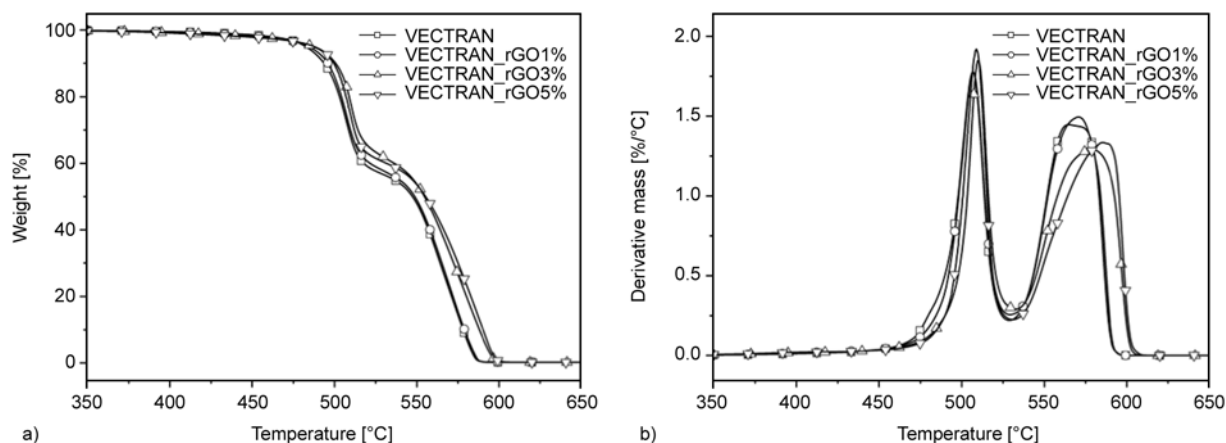
material's degradation, and no residual mass is recorded above 600°C . Most importantly, not only the onset temperature but also the temperature of maximum degradation rate of both degradation steps significantly increased with the filler content, evidencing the beneficial effect of filler incorporation on the degradation behavior of the material. Noteworthy, the TGA analyses on Vectran and relative nanocomposites confirm that no significant degradation occurs during the process of *in-situ* reduction of GO (as performed at 320°C for 5 min followed by annealing at 290°C for 3.5 h, see Paragraph 2.2).

3.2.3. Surface resistivity

Neat Vectran exhibits very high surface resistivity value typical for an insulating polymer (i.e. $\sim 10^{13} \Omega/\text{sq}$). Vectran_rGO composites show a remarkable decrease of the surface resistivity down to $3.7 \cdot 10^7 \Omega/\text{sq}$ with a filler content of only 3 wt% (Table 5). Since the resistivity decreases less than one order of magnitude as the filler amount rises from 3 to 5 wt%, a percolation threshold can be estimated between 1 and 3 wt%. Therefore, resistivity data clearly evidence that GO reduction can effectively take place also in a solid polymer matrix at a relatively mild temperature. Specifically, the selected treatment temperature is supposed to be higher

Table 5. Surface resistivity of Vectran and Vectran/rGO nanocomposites

Sample	Surface resistivity [Ω/sq]
VECTRAN	$3.85 \cdot 10^{13}$
VECTRAN_rGO1%	$2.40 \cdot 10^{13}$
VECTRAN_rGO3%	$3.74 \cdot 10^7$
VECTRAN_rGO5%	$2.09 \cdot 10^7$

**Figure 6.** (a) TGA curves and (b) derivative TGA curves of VECTRAN and Vectran/rGO nanocomposites (air environment, heating rate = $5^{\circ}\text{C}\cdot\text{min}^{-1}$)

enough to favor diffusive phenomena and the reaction kinetics. Concurrently, no significant matrix degradation occurs during treatment, as confirmed by TGA analyses.

3.2.4. Mechanical response

The typical stress-strain curves obtained under ramp tensile tests are reported in Figure 7, while the main parameters measurable from these tests are summarized in Table 6. The nanofiller induces an increase of the elastic modulus, with an improvement of 22% for the system filled with 1 wt% of GO compared to unfilled Vectran. The reinforcing effect provided by nanofiller incorporation could be explained by the reduction of macromolecules mobility constrained within filler agglomerates [52, 53]. Moreover, it has also been proved that the formation of a certain fraction of constrained matrix in proximity of the filler surfaces (i.e. interphase region) can significantly contribute to the stiffening effect [54]. Incorporation of a filler amount of 3 wt% results in further increase of the material stiffness. However, the progressive nanofiller agglomeration at elevated filler amounts leads to a decrease of the strain at break. On the other hand, the tensile strength does not seem to be appreciably affected by the presence of the nanofiller.

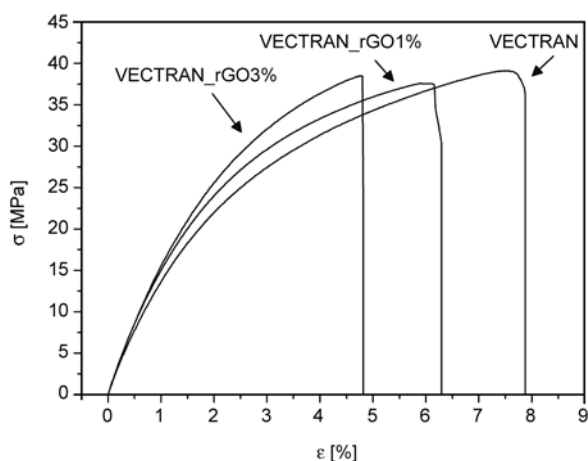


Figure 7. Stress/strain curves of VECTRAN and Vectran/rGO nanocomposites

Table 6. Quasi-static tensile properties of Vectran and Vectran/rGO nanocomposites

Sample*	Tensile modulus [MPa]	Tensile strength [MPa]	Strain at break [%]
VECTRAN	1483±76	42.7±3.9	7.7±1.2
VECTRAN_rGO1%	1805±50	41.2±2.6	6.4±1.7
VECTRAN_rGO3%	1851±21	40.2±3.7	4.8±0.7

*The sample VECTRAN_rGO5% was not tested due to problems with the specimens' preparation.

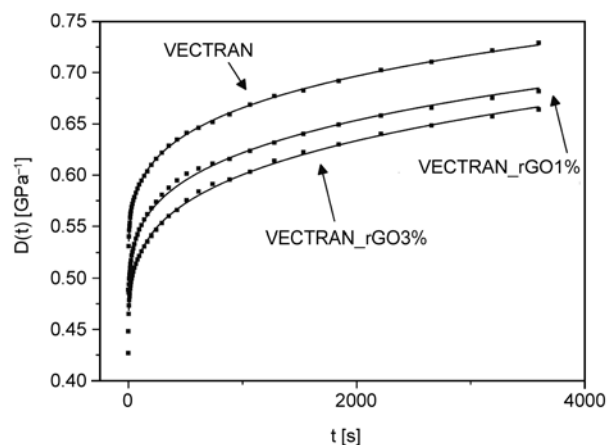


Figure 8. Creep compliance ($D(t)$) of VECTRAN and Vectran/rGO nanocomposites ($T = 30^\circ\text{C}$, $\sigma_0 = 4 \text{ MPa}$). Experimental data were fitted applying the Findley model [55] (continuous lines).

In Figure 8 the isothermal (30°C) creep compliance curves under a constant stress of 4 MPa are reported for both unfilled Vectran and relative nanocomposites. Noteworthy, an accurate fit of the experimental data was achieved applying the Findley model [55] (continuous lines). According to these results, nanofiller incorporation results in an improved creep stability with respect to the neat Vectran. In particular, the elastic component of the creep compliance was significantly reduced, while only a slight effect can be noticed on the viscoelastic component.

A further investigation on the viscoelastic behavior of the prepared samples was carried out through DMTA analyses. The storage (E') modulus increases with the filler loading (Figure 9a) over the whole range of testing temperatures. The enhancement of the thermo-mechanical properties upon nanofiller introduction can be explained considering three factors: the high intrinsic stiffness of the nanofiller, the good level of filler dispersion within the matrix and the degree of filler-matrix interfacial interaction [56]. However, while the first factor seems to have a significant impact on the stiffness of the prepared nanocomposites, the second factor was not properly investigated due to difficulties in the morphological analysis. The filler-matrix interfacial interactions can be further investigated by an accurate analysis of $\tan\delta$ plots. In particular, $\tan\delta$ plots show three distinct peaks attributed to the material's characteristic α , β and γ relaxations (Figure 9b). The α relaxation is associated to the thermal relaxation of the whole polymeric chains corresponding to the glass transition temperature (T_g). In the specific case of LCP, this relaxation is attributed to the transition from

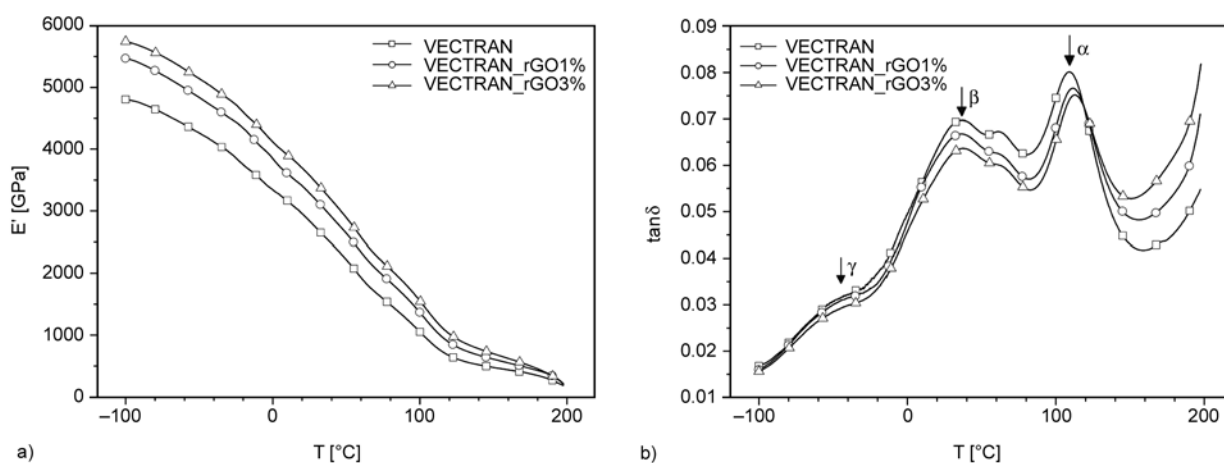


Figure 9. DMA tests on VECTRAN and Vectran/rGO nanocomposites (frequency =1 Hz): (a) storage modulus (E'), (b) loss factor ($\tan \delta$).

a quenched nematic phase to a thermally relaxed nematic phase. On the other hand, β and γ relaxations are associated to the C–O chemical bonds distributed along the polymeric chains, specifically the rotation of naphthalene and phenylene rings, respectively [40]. The filler incorporation results in a slight increase of T_g (from 109 to 113°C for VECTRAN and VECTRAN_GO3%, respectively), indicating a certain restriction of the segmental motion of the polymeric chains located in proximity of the filler's surfaces, while no clear change is observed on the β and γ relaxation temperatures. Therefore, taking into account that filler incorporation results in a limited T_g increase without any effect on the viscoelastic creep compliance, it can be hypothesized that the prepared materials are characterized by a relatively weak filler-matrix interaction degree. This conclusion can be explained considering that (i) the thickness of the physically absorbed Vectran layer on the surface of the filler surfaces is limited due to agglomeration and/or (ii) that the filler-matrix interfacial adhesion is restricted by the poor chemical affinity between the two phases. Both these aspects can affect the viscoelastic behavior of the resulting materials, and further efforts will be required in the future to reach a deeper comprehension of the obtained results.

4. Conclusions

New LCP nanocomposites reinforced with rGO were prepared by in situ thermal reduction of GO particles dispersed in a Vectran matrix. The kinetics of the GO thermal reduction was assessed by spectroscopic analyses (XRD and XPS), thermogravimetric analysis and surface resistivity measurements. It was found that a thermal treatment at 300°C for 4 h

induced an extended reduction of GO nanoplatelets with an increase of the C/O ratio content by a factor of 2.8. A decrease in resistivity (i.e. from $3.9 \cdot 10^{13}$ to $3.7 \cdot 10^7 \Omega/\text{sq}$) can be achieved at a filler amount of 3 wt%. Improvements in the elastic modulus, creep stability and thermo-mechanical behavior were also related to nanofiller incorporation. Also the thermal degradation behavior was enhanced. On the other hand, the slight increase in the glass transition temperature in the nanomodified samples indicated that probably a poor filler dispersion was achieved.

Acknowledgements

The authors would like to thank Dr. Thiago Medeiros Araujo and Dr. Matteo Traina for their precious help on several aspects of the experimental work. The precious contribute of prof. Riccardo Ceccato in X-ray diffraction measurements is also kindly acknowledged.

References

- [1] Geim A. K., Novoselov K. S.: The rise of graphene. *Nature Materials*, **6**, 183–191 (2007). DOI: [10.1038/nmat1849](https://doi.org/10.1038/nmat1849)
- [2] Kuila T., Bose S., Mishra A. K., Khanra P., Kim N. H., Lee J. H.: Chemical functionalization of graphene and its applications. *Progress in Materials Science*, **57**, 1061–1105 (2012). DOI: [10.1016/j.pmatsci.2012.03.002](https://doi.org/10.1016/j.pmatsci.2012.03.002)
- [3] Kim H., Abdala A. A., Macosko C. W.: Graphene/polymer nanocomposites. *Macromolecules*, **43**, 6515–6530 (2010). DOI: [10.1021/ma100572e](https://doi.org/10.1021/ma100572e)
- [4] Rafiee M. A., Rafiee J., Srivastava I., Wang Z., Song H., Yu Z.-Z., Koratkar N.: Fracture and fatigue in graphene nanocomposites. *Small*, **6**, 179–183 (2010). DOI: [10.1002/sml.200901480](https://doi.org/10.1002/sml.200901480)

- [5] Kalaitzidou K., Fukushima H., Drzal L. T.: Multifunctional polypropylene composites produced by incorporation of exfoliated graphite nanoplatelets. *Carbon*, **45**, 1446–1452 (2007).
DOI: [10.1016/j.carbon.2007.03.029](https://doi.org/10.1016/j.carbon.2007.03.029)
- [6] Tait M., Pegoretti A., Dorigato A., Kalaitzidou K.: The effect of filler type and content and the manufacturing process on the performance of multifunctional carbon/poly-lactide composites. *Carbon*, **49**, 4280–4290 (2011).
DOI: [10.1016/j.carbon.2011.06.009](https://doi.org/10.1016/j.carbon.2011.06.009)
- [7] Ganguli S., Roy A. K., Anderson D. P.: Improved thermal conductivity for chemically functionalized exfoliated graphite/epoxy composites. *Carbon*, **46**, 806–817 (2008).
DOI: [10.1016/j.carbon.2008.02.008](https://doi.org/10.1016/j.carbon.2008.02.008)
- [8] Hung M.-T., Choi O., Ju Y. S., Hahn H. T.: Heat conduction in graphite-nanoplatelet-reinforced polymer nanocomposites. *Applied Physics Letters*, **89**, 023117/1–023117/3 (2006).
DOI: [10.1063/1.2221874](https://doi.org/10.1063/1.2221874)
- [9] Wu H., Drzal L. T.: High thermally conductive graphite nanoplatelet/polyetherimide composite by pre-coating: Effect of percolation and particle size. *Polymer Composites*, **34**, 2148–2153 (2013).
DOI: [10.1002/Pc.22624](https://doi.org/10.1002/Pc.22624)
- [10] Saravanan N., Rajasekar R., Mahalakshmi S., Sathishkumar T. P., Sasikumar K. S. K., Sahoo S.: Graphene and modified graphene-based polymer nanocomposites – A review. *Journal of Reinforced Plastics and Composites*, **33**, 1158–1180 (2014).
DOI: [10.1177/0731684414524847](https://doi.org/10.1177/0731684414524847)
- [11] Du X., Yu Z.-Z., Dasari A., Ma J., Mo M., Meng Y., Mai Y.-W.: New method to prepare graphite nanocomposites. *Chemistry of Materials*, **20**, 2066–2068 (2008).
DOI: [10.1021/cm703285s](https://doi.org/10.1021/cm703285s)
- [12] Stankovich S., Piner R. D., Nguyen S. T., Ruoff R. S.: Synthesis and exfoliation of isocyanate-treated graphene oxide nanoplatelets. *Carbon*, **44**, 3342–3347 (2006).
DOI: [10.1016/j.carbon.2006.06.004](https://doi.org/10.1016/j.carbon.2006.06.004)
- [13] Wang G., Wang B., Park J., Yang J., Shen X., Yao J.: Synthesis of enhanced hydrophilic and hydrophobic graphene oxide nanosheets by a solvothermal method. *Carbon*, **47**, 68–72 (2009).
DOI: [10.1016/j.carbon.2008.09.002](https://doi.org/10.1016/j.carbon.2008.09.002)
- [14] Park S., An J., Jung I., Piner R. D., An S. J., Li X., Velamakanni A., Ruoff R. S.: Colloidal suspensions of highly reduced graphene oxide in a wide variety of organic solvents. *Nano Letters*, **9**, 1593–1597 (2009).
DOI: [10.1021/nl803798y](https://doi.org/10.1021/nl803798y)
- [15] Li D., Müller M. B., Gilje S., Kaner R. B., Wallace G. G.: Processable aqueous dispersions of graphene nanosheets. *Nature Nanotechnology*, **3**, 101–105 (2008).
DOI: [10.1038/nnano.2007.451](https://doi.org/10.1038/nnano.2007.451)
- [16] Stankovich S., Piner R. D., Chen X., Wu N., Nguyen S. T., Ruoff R. S.: Stable aqueous dispersions of graphitic nanoplatelets *via* the reduction of exfoliated graphite oxide in the presence of poly(sodium 4-styrenesulfonate). *Journal of Materials Chemistry*, **16**, 155–158 (2006).
DOI: [10.1039/B512799H](https://doi.org/10.1039/B512799H)
- [17] Titelman G. I., Gelman V., Bron S., Khalfin R. L., Cohen Y., Bianco-Peled H.: Characteristics and microstructure of aqueous colloidal dispersions of graphite oxide. *Carbon*, **43**, 641–649 (2005).
DOI: [10.1016/j.carbon.2004.10.035](https://doi.org/10.1016/j.carbon.2004.10.035)
- [18] Cerezo F. T., Preston C. M. L., Shanks R. A.: Morphology, thermal stability, and mechanical behavior of [poly(propylene)-grafted maleic anhydride]-layered expanded graphite oxide composites. *Macromolecular Materials and Engineering*, **292**, 155–168 (2007).
DOI: [10.1002/mame.200600303](https://doi.org/10.1002/mame.200600303)
- [19] Ying Z. R., Dang Z. M., Yan X. H., Ouyang X., Gao Y. Y.: Crystallization properties of polypropylene/graphene oxide nanocomposites. *Advanced Materials Research*, **335–336**, 347–350 (2011).
DOI: [10.4028/www.scientific.net/AMR.335-336.347](https://doi.org/10.4028/www.scientific.net/AMR.335-336.347)
- [20] Wang J., Wang X., Xu C., Zhang M., Shang X.: Preparation of graphene/poly(vinyl alcohol) nanocomposites with enhanced mechanical properties and water resistance. *Polymer International*, **60**, 816–822 (2011).
DOI: [10.1002/pi.3025](https://doi.org/10.1002/pi.3025)
- [21] Park S., An J., Potts J. R., Velamakanni A., Murali S., Ruoff R. S.: Hydrazine-reduction of graphite- and graphene oxide. *Carbon*, **49**, 3019–3023 (2011).
DOI: [10.1016/j.carbon.2011.02.071](https://doi.org/10.1016/j.carbon.2011.02.071)
- [22] Gilje S., Han S., Wang M., Wang K. L., Kaner R. B.: A chemical route to graphene for device applications. *Nano Letters*, **7**, 3394–3398 (2007).
DOI: [10.1021/nl0717715](https://doi.org/10.1021/nl0717715)
- [23] Ren P.-G., Yan D.-X., Ji X., Chen T., Li Z.-M.: Temperature dependence of graphene oxide reduced by hydrazine hydrate. *Nanotechnology*, **22**, 055705/1–055705/8 (2011).
DOI: [10.1088/0957-4484/22/5/055705](https://doi.org/10.1088/0957-4484/22/5/055705)
- [24] Traina M., Pegoretti A.: *In situ* reduction of graphene oxide dispersed in a polymer matrix. *Journal of Nanoparticle Research*, **14**, 801/1–801/6 (2012).
DOI: [10.1007/s11051-012-0801-0](https://doi.org/10.1007/s11051-012-0801-0)
- [25] Jung I., Dikin D. A., Piner R. D., Ruoff R. S.: Tunable electrical conductivity of individual graphene oxide sheets reduced at ‘low’ temperatures. *Nano Letters*, **8**, 4283–4287 (2008).
DOI: [10.1021/nl8019938](https://doi.org/10.1021/nl8019938)
- [26] Chen W., Yan L., Bangal P. R.: Preparation of graphene by the rapid and mild thermal reduction of graphene oxide induced by microwaves. *Carbon*, **48**, 1146–1152 (2010).
DOI: [10.1016/j.carbon.2009.11.037](https://doi.org/10.1016/j.carbon.2009.11.037)

- [27] Kim C.-J., Khan W., Park S.-Y.: Structural evolution of graphite oxide during heat treatment. *Chemical Physics Letters*, **511**, 110–115 (2011).
DOI: [10.1016/j.cplett.2011.06.016](https://doi.org/10.1016/j.cplett.2011.06.016)
- [28] Sengupta R., Bhattacharya M., Bandyopadhyay S., Bhowmick A. K.: A review on the mechanical and electrical properties of graphite and modified graphite reinforced polymer composites. *Progress in Polymer Science*, **36**, 638–670 (2011).
DOI: [10.1016/j.progpolymsci.2010.11.003](https://doi.org/10.1016/j.progpolymsci.2010.11.003)
- [29] Cote L. J., Cruz-Silva R., Huang J.: Flash reduction and patterning of graphite oxide and its polymer composite. *Journal of the American Chemical Society*, **131**, 11027–11032 (2009).
DOI: [10.1021/ja902348k](https://doi.org/10.1021/ja902348k)
- [30] Zhu Y., Murali S., Cai W., Li X., Suk J. W., Potts J. R., Ruoff R. S.: Graphene and graphene oxide: Synthesis, properties, and applications. *Advanced Materials*, **22**, 3906–3924 (2010).
DOI: [10.1002/adma.201001068](https://doi.org/10.1002/adma.201001068)
- [31] Dai B., Fu L., Liao L., Liu N., Yan K., Chen Y., Liu Z.: High-quality single-layer graphene *via* reductive reduction of graphene oxide. *Nano Research*, **4**, 434–439 (2011).
DOI: [10.1007/s12274-011-0099-8](https://doi.org/10.1007/s12274-011-0099-8)
- [32] Yin K., Li H., Xia Y., Bi H., Sun J., Liu Z., Sun L.: Thermodynamic and kinetic analysis of low-temperature thermal reduction of graphene oxide. *Nano-Micro Letters*, **3**, 51–55 (2011).
DOI: [10.3786/nml.v3i1.p51-55](https://doi.org/10.3786/nml.v3i1.p51-55)
- [33] Liu K., Chen L., Chen Y., Wu J., Zhang W., Chen F., Fu Q.: Preparation of polyester/reduced graphene oxide composites *via in situ* melt polycondensation and simultaneous thermo-reduction of graphene oxide. *Journal of Materials Chemistry*, **21**, 8612–8617 (2011).
DOI: [10.1039/C1JM10717H](https://doi.org/10.1039/C1JM10717H)
- [34] Zhu Y., Stoller M. D., Cai W., Velamakanni A., Piner R. D., Chen D., Ruoff R. S.: Exfoliation of graphite oxide in propylene carbonate and thermal reduction of the resulting graphene oxide platelets. *ACS Nano*, **4**, 1227–1233 (2010).
DOI: [10.1021/nn901689k](https://doi.org/10.1021/nn901689k)
- [35] Pegoretti A., Traina M.: Liquid crystalline organic fibres and their mechanical behaviour. in ‘Handbook of tensile properties of textile and technical fibres’ (eds.: Bunsell A. R.) Woodhead Publishing, Cambridge, 354–436 (2009).
DOI: [10.1533/9781845696801.2.354](https://doi.org/10.1533/9781845696801.2.354)
- [36] Pegoretti A., Zanolli A., Migliaresi C.: Flexural and interlaminar mechanical properties of unidirectional liquid crystalline single-polymer composites. *Composites Science and Technology*, **66**, 1953–1962 (2006).
DOI: [10.1016/j.compscitech.2006.01.015](https://doi.org/10.1016/j.compscitech.2006.01.015)
- [37] Pegoretti A., Zanolli A., Migliaresi C.: Preparation and tensile mechanical properties of unidirectional liquid crystalline single-polymer composites. *Composites Science and Technology*, **66**, 1970–1979 (2006).
DOI: [10.1016/j.compscitech.2006.01.012](https://doi.org/10.1016/j.compscitech.2006.01.012)
- [38] Medeiros Araujo T., Pegoretti A.: Liquid crystalline single-polymer short-fibers composites. *Composite Interfaces*, **20**, 287–298 (2013).
DOI: [10.1080/15685543.2013.796753](https://doi.org/10.1080/15685543.2013.796753)
- [39] Biswas S., Fukushima H., Drzal L. T.: Mechanical and electrical property enhancement in exfoliated graphene nanoplatelet/liquid crystalline polymer nanocomposites. *Composites Part A: Applied Science and Manufacturing*, **42**, 371–375 (2011).
DOI: [10.1016/j.compositesa.2010.12.006](https://doi.org/10.1016/j.compositesa.2010.12.006)
- [40] Kalfon-Cohen E., Pegoretti A., Marom G.: Annealing of drawn monofilaments of liquid crystalline polymer vectra/vapor grown carbon fiber nanocomposites. *Polymer*, **51**, 1033–1041 (2010).
DOI: [10.1016/j.polymer.2010.01.016](https://doi.org/10.1016/j.polymer.2010.01.016)
- [41] Kim J. Y.: Carbon nanotube-reinforced thermotropic liquid crystal polymer nanocomposites. *Materials*, **2**, 1955–1974 (2009).
DOI: [10.3390/ma2041955](https://doi.org/10.3390/ma2041955)
- [42] Qi B., Lu S. R., Xiao X. E., Pan L. L., Tan F. Z., Yu J. H.: Enhanced thermal and mechanical properties of epoxy composites by mixing thermotropic liquid crystalline epoxy grafted graphene oxide. *Express Polymer Letters*, **8**, 467–479 (2014).
DOI: [10.3144/expresspolymlett.2014.51](https://doi.org/10.3144/expresspolymlett.2014.51)
- [43] Gibson R. F.: A review of recent research on mechanics of multifunctional composite materials and structures. *Composite Structures*, **92**, 2793–2810 (2010).
DOI: [10.1016/j.compstruct.2010.05.003](https://doi.org/10.1016/j.compstruct.2010.05.003)
- [44] Hummers W. S. J., Offeman R. E.: Preparation of graphitic oxide. *Journal of American Chemical Society*, **80**, 1339 (1958).
DOI: [10.1021/ja01539a017](https://doi.org/10.1021/ja01539a017)
- [45] Kovtyukhova N. I., Ollivier P. J., Martin B. R., Mallouk T. E., Chizhik S. A., Buzaneva E. V., Gorchinskiy A. D.: Layer-by-layer assembly of ultrathin composite films from micron-sized graphite oxide sheets and polycations. *Chemistry of Materials*, **11**, 771–778 (1999).
DOI: [10.1021/cm981085u](https://doi.org/10.1021/cm981085u)
- [46] Shang S., Zhao L., Liu W., Zhao P., Li X.: A high-luminescence fringelike field emission from screen-printed carbon nanotube and zinc oxide composite film. *Journal of Electromagnetic Analysis and Applications*, **2**, 649–653 (2010).
DOI: [10.4236/jemaa.2010.212085](https://doi.org/10.4236/jemaa.2010.212085)
- [47] Huh S. H.: Thermal reduction of graphene oxide. in ‘Physics and applications of graphene – Experiments’, (ed.: Mikhailov S.) InTech, Rijeka, 73–90 (2011).
DOI: [10.5772/14156](https://doi.org/10.5772/14156)
- [48] Sawyer L., Jaffe M.: The structure of thermotropic copolyesters. *Journal of Materials Science*, **21**, 1897–1913 (1986).
DOI: [10.1007/BF00547924](https://doi.org/10.1007/BF00547924)
- [49] Weng T., Hiltner A., Baer E.: Hierarchical structure in a thermotropic liquid-crystalline copolyester. *Journal of Materials Science*, **21**, 744–750 (1986).
DOI: [10.1007/BF01117348](https://doi.org/10.1007/BF01117348)

- [50] Chung T. S.: Thermotropic liquid crystal polymers: Thin-film polymerization, characterization, blends, applications. Technomic Publishing, Lancaster (2001).
- [51] Dorigato A., Pegoretti A., Frache A.: Thermal stability of high density polyethylene–fumed silica nanocomposites. *Journal of Thermal Analysis and Calorimetry*, **109**, 863–873 (2012).
DOI: [10.1007/s10973-012-2421-4](https://doi.org/10.1007/s10973-012-2421-4)
- [52] Dorigato A., Dzenis Y., Pegoretti A.: Filler aggregation as a reinforcement mechanism in polymer nanocomposites. *Mechanics of Materials*, **61**, 79–90 (2013).
DOI: [10.1016/j.mechmat.2013.02.004](https://doi.org/10.1016/j.mechmat.2013.02.004)
- [53] Dzenis Y. A.: Effect of aggregation of a dispersed rigid filler on the elastic characteristics of a polymer composite. *Mechanics of Composite Materials*, **22**, 12–19 (1986).
DOI: [10.1007/BF00606002](https://doi.org/10.1007/BF00606002)
- [54] Karevan M., Kalaitzidou K.: Formation of a complex constrained region at the graphite nanoplatelets-polyamide 12 interface. *Polymer*, **54**, 3691–3698 (2013).
DOI: [10.1016/j.polymer.2013.05.019](https://doi.org/10.1016/j.polymer.2013.05.019)
- [55] Findley W. N., Lai J. S. Y., Onaran K.: Creep and relaxation of nonlinear viscoelastic materials: With an introduction to linear viscoelasticity. Dover, New York (1976).
- [56] Jancar J.: Review of the role of the interphase in the control of composite performance on micro- and nano-length scales. *Journal of Materials Science*, **43**, 6747–6757 (2008).
DOI: [10.1007/s10853-008-2692-0](https://doi.org/10.1007/s10853-008-2692-0)

Toughening of poly(lactic acid) without sacrificing stiffness and strength by melt-blending with polyamide 11 and selective localization of halloysite nanotubes

B. J. Rashmi, K. Prashantha*, M-F. Lacrampe, P. Krawczak

Mines Douai, Department of Polymers and Composites Technology and Mechanical Engineering, 941 rue Charles Bourseul, CS 10838, F-59508 Douai Cedex, France

Received 15 December 2014; accepted in revised form 25 February 2015

Abstract. This paper aims at improving the mechanical behavior of biobased brittle amorphous polylactide (PLA) by extrusion melt-blending with biobased semi-crystalline polyamide 11 (PA11) and addition of halloysite nanotubes (HNT). The morphological analysis of the PLA/PA11/HNT blends shows a strong interface between the two polymeric phases due to hydrogen bonding, and the migration of HNTs towards PA11 phase inducing their selective localization in one of the polymeric phases of the blend. A ‘salami-like’ structure is formed revealing a HNTs-rich tubular-like (fibrillar) PA11 phase. Moreover, HNTs localized in the dispersed phase act as nucleating agents for PA11. Compared to neat PLA, this leads to a remarkable improvement in tensile and impact properties (elongation at break is multiplied by a factor 43, impact strength by 2, whereas tensile strength and stiffness are almost unchanged). The toughening mechanism is discussed based on the combined effect of resistance to crack propagation and nanotubes load bearing capacity due to the existence of the fibrillar structure. Thus, blending brittle PLA with PA11 and HNT nanotubes results in tailor-made PLA-based compounds with enhanced ductility without sacrificing stiffness and strength.

Keywords: polymer blends and alloys, biopolymers, polylactide, polyamide 11, halloysite nanotubes

1. Introduction

Polylactide or poly(lactic acid) (PLA) is considered as being a promising thermoplastic polyester because of its renewable resource-based origin along with its biodegradability and its biocompatibility [1–4]. Nevertheless, its inherent brittleness is a major drawback for its large-scale commercial applications. Thus, numerous approaches have been adopted to correct this drawback [1, 2, 5], one of them being based on melt blending PLA with a more ductile engineered polymer such as polyamide (PA).

Ebadi-Dehaghani *et al.* [6] showed that the tensile behavior of PLA varies dramatically from brittle to ductile when blended with at least 15 wt% of a terpolymer of PA (PA6/PA66/PA610). The elongation

at break increases from 5% (neat PLA) to 176% (PLA with 20 wt% of PA). The two glass transition temperatures (T_g) of PLA and PA in blends shift to lower T_g than their respective original ones, sign of a partially miscible system due to the interactions led by hydrogen bonding between the molecules of PA and PLA. The spherical particles of PA are dispersed homogeneously in the PLA matrix. The strong interfacial adhesion of the two phases is beneficial for the improvement of the ductility. Unfortunately, this toughness improvement was achieved at the expense of the tensile resistance which decreases by 25% [6]. Arrieta *et al.* [7] reported a significant improvement of the unnotched Izod impact strength of PLA when blended with 50 wt% of a bio-based

*Corresponding author, e-mail: kalappa.prashantha@mines-douai.fr
© BME-PT

PA610 and 2 phr epoxy resin as reactive compatibilizer. While neat PLA shows a brittle behavior, unnotched impact strength of the compatibilized blend achieves no break level. This toughening effect was ascribed to (i) the formation of a polyester-polyamide block copolymer during blending, which acts as an efficient compatibilizing agent reducing the dispersed phase size and (ii) the reaction between epoxy resin and the terminal functional groups of both PLA and PA610 favoring adhesion between the two components. Nevertheless, the compatibilized blend did not exhibit improved mechanical properties (Young modulus, tensile and flexural strengths, elongation at break) except unnotched impact strength [7]. Derho *et al.* [8] characterized the morphology, thermal and mechanical behavior of PLA/PA11 blends over a large composition range. The good compatibility between both polymers, highlighted by the morphological analysis, induces an increase in the ductility only for PA11 content higher than 50 wt%, obtained at the expense of rigidity and yield stress. For the blend containing 20 wt% of PA11, the elongation at break remains similar to that of the neat PLA while its rigidity is reduced by approximately 38% [8]. Pai *et al.* [9] showed that such PLA/PA11 blends can be compatibilized by titanium isopropoxide catalyst through interchange reaction. However, an improvement of the ductility and toughness is observed only for high PA11 contents (>50 wt%), both Young modulus and stress at break showing a substantial decrease.

Recent literature reports suggest that, nanostructured polymer blends having a minor polymer phase with nanoscale dimensions offer much promise because of enhanced toughness in comparison to conventional polymer blends [10–12]. This method was used by Nuzzo and coworkers [13–15] to prepare PLA/PA11 blends containing small amounts of nanoparticles (organo-modified montmorillonite (OMMT), sepiolite and carbon nanotubes). Co-continuous morphologies are obtained and with fillers preferentially located inside the minor PA11 phase. These blends show improved thermal stability, their structural integrity being kept up to ~160°C, i.e., about 100°C above the PLA glass transition temperature. But no information was given on their tensile behavior and their ductility. Finally, existing literature suffers from a lack of detailed investigations on the mechanical properties and toughening mecha-

nism in particular for PLA/PA11 nanocomposites, which opens the avenues for further studies.

So, in practice, a PLA-based material having good stiffness-toughness balance along with high bio-based PLA content remains still elusive. Therefore, the present work focuses on the toughening of PLA without sacrificing stiffness and strength by melt blending with bio-sourced PA11 and by phase selective localization of natural halloysite nanotubes in PA11 phase of blends.

2. Experimental

2.1. Materials

Poly lactide (PLA) in pellets form (4032D, Natureworks, USA) has a specific gravity of 1.24 and a melt flow index around 7 g/10 min at 210°C. Polyamide 11 (PA11) is an injection molding grade (Rilsan® BMNO TLD, Arkema, France). Halloysite nanotubes (HNT) (Natural Nano, Inc, USA) have an average diameter of 80 nm, a length of about 1.2 microns, and a density of 2.5 g·cm⁻³. All materials used in this study were dried in an oven at 80°C overnight to remove any excess moisture.

2.2. Compounding and processing procedure

Masterbatches containing 15 wt% of halloysites were prepared by adding nanotubes in the melt zone of a twin-screw extruder (Haake PolyLab OS, Thermoscientific, USA) equipped with a screw of 16 mm diameter and *L/D* of 40 length to diameter ratio. The temperature profile of the extruder for the production of PA11/HNT masterbatch was set at 220°C in the feed zone, sequentially at 225, 227, 230, and 232°C in the metering zone and 235°C at the die. The screw speed and feed rate were set at 60 rpm and 1 kg·h⁻¹ respectively. In case of PLA/HNT masterbatch, the temperature profile in the extruder was set between 170 to 180°C from feed zone to die. The screw speed and feed rate were set at 40 rpm and 1 kg·h⁻¹ respectively. Extruded masterbatches were cut into small pellets in a pelletizer (SGS 25-E4, Scheer, Germany). Both masterbatch pellets were dried at 80°C in vacuum oven for overnight to remove residual water content for further utilization. The previously prepared 15 wt% halloysite nanotubes loaded PLA/HNT and PA11/HNT masterbatches were diluted with neat PLA and neat PA11 to give 2, 4 and 6 wt% HNTs in PLA/PA11 nanocomposites with a blend mixture ratio of 80:20 compounded using afore mentioned twin-screw extruder

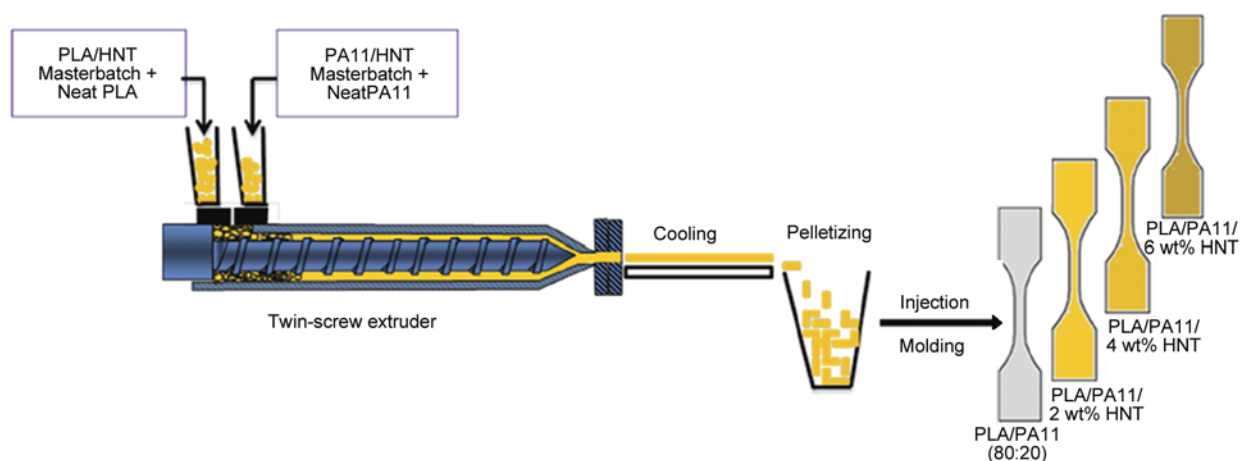


Figure 1. Schematic illustration of compounding process

(Figure 1). The melt-compounding temperature of the barrel was in the range of 193 to 198°C at a screw speed of 100 rpm. After compounding, the extrudate strand was cut into pellets.

After pelletizing, the dried (80°C in vacuum oven for overnight) nanocomposite granules were compression-molded into 2 mm-thick plates using a hydraulic press (Dolouets, France) at 205°C during 2 min for rheological experiments. For mechanical testing, nanocomposite granules were injection-molded (Babyplast 6/10P, Spain) into standard test specimen for tensile, impact and dynamic mechanical tests. During injection molding, the temperature profile ranged from 200 to 205°C and the mold temperature was kept at 35°C. The injection molding throughput and the holding pressure were 1.25 cm³·s⁻¹, and 80 bars respectively with a cooling time of 10 seconds. As a reference, neat PLA/PA11 in the same proportion was also similarly extruded and then injection-molded for rheological and mechanical studies.

2.3. Characterization methods

2.3.1. Scanning and transmission electron microscopy

Scanning electron microscopy (SEM) was used to analyse morphology (S-4300 SE/N, Hitachi, Japan). Injection-molded samples were cryofractured both in transversal and longitudinal directions. Then, samples were coated with a thin gold layer (Polaron E5100 series II, Watford) to observe the morphology under high vacuum at 5 kV.

Additionally, for transmission electron microscopy (TEM), injection-molded samples were cut using a cryo-diamond knife on a microtome (Leica ultracut, LEICA, Germany) to give sections with a nominal

thickness of 150 nm. These sections were transferred to Cu grids of 400 meshes. Bright-field TEM images of nanocomposites were obtained at 200 kV under low dose conditions with an electron microscope (Philips CM30 Zaventem, Belgium), using a CCD camera (Gatan, USA).

2.3.2. Differential scanning calorimetry (DSC)

Thermal transitions of the materials were examined by differential scanning calorimetry (DSC 7 Perkin-Elmer, USA) under nitrogen flow (20 mL·min⁻¹). Samples were crimple-sealed in aluminum pans and heated from 30 to 220°C at a heating rate of 10°C·min⁻¹ (first heating scan), equilibrated at 220°C for 2 min, cooled at 10°C·min⁻¹ to 30°C, equilibrated at 30°C for 2 min, and then heated again to 220°C at 10°C·min⁻¹ (second heating scan).

2.3.3. Rheology

Oscillatory shear measurements were performed using an advanced rheometric system (HAAKE MARS, TA Instruments, Germany). The measurements were performed at 205°C using plate and plate geometry (diameter, 35 mm). Deformation in the linear viscoelastic region was found to be 2% and then chosen for all subsequent frequency sweep tests. Samples were equilibrated at 205°C before testing. The frequency was varied from 0.1 to 100 rad·s⁻¹.

2.3.4. Dynamic mechanical analysis (DMA)

The viscoelastic behavior was studied in tension by dynamic mechanical analysis (DMA+150, MetraviB, France). Dynamic strain sweep was first performed to determine the linear viscoelastic range of the materials. The tests were then performed at a strain

amplitude of 2% and a frequency of 1 Hz. Data were collected from -50 to 120°C at a scanning rate of 3°C·min⁻¹. Rectangular DMA specimens (nominal dimensions, (4±0.2)×(10±0.5)×30 mm³) were cut from injection-molded impact bar samples.

2.3.5. Mechanical behavior testing

The mechanical properties were evaluated from injection-molded specimens. Tensile strength and elongation at break were measured at a crosshead rate of 5 mm·min⁻¹ and modulus at 1 mm·min⁻¹, using a tensile machine (Lloyd LR 50 K, USA) at 25°C and 50% RH according to ISO 527 standard. Charpy notched and un-notched impact tests were carried out as per ISO 179-1 standard by using a pendulum impact machine (Model 5101, Zwick, Germany) at 25°C and 50% RH. All the reported values were calculated as averages over five and ten specimens for tensile and impact test respectively.

3. Results and discussion

3.1. HNTs selective localization in PLA/PA11 blend

The selective localization of nanofillers in a specific polymer phase of an immiscible polymer blend is generally governed by thermodynamic factors. Wetting coefficient ω_a is proposed to deduce the selective localization of nanofiller according to Equation (1) [16]:

$$\omega_a = \frac{\gamma_{\text{nanofiller-polymer}_1} - \gamma_{\text{nanofiller-polymer}_2}}{\gamma_{\text{polymer}_1,2}} \quad (1)$$

where, $\gamma_{\text{nanofiller-polymer}_1}$, $\gamma_{\text{nanofiller-polymer}_2}$, and $\gamma_{\text{polymer}_1,2}$ are the interfacial energies between nanofiller and polymer₁, between nanofiller and polymer₂, and between the two polymer phases. In the present work PLA represents polymer₁ and PA11 represents polymer₂. If $\omega_a > 1$, nanofiller preferentially locates in polymer₂; if $\omega_a < -1$, nanofiller preferentially locates in polymer₁, and if $-1 < \omega_a < 1$, nanofiller locates at the interface.

The interfacial energy between nanofiller and polymer can be adjusted in different degrees by different surface modifications of nanofiller and/or the modification of polymer matrix. The interfacial energy can be calculated according to the harmonic-mean (Equation (2)) and geometric-mean (Equation (3)) [17]:

Table 1. Surface energy data of the ternary system components

Material	Surface energy [mN·m ⁻¹]			References
	γ_i^{total}	γ_i^{d}	γ_i^{p}	
PLA	47.0	35.9	11.1	[18]
PA11	45.0	40.0	5.0	[19]
HNT	28.4	26.9	1.5	[20]

Table 2. Calculated interfacial energy

Material	Interfacial energy [mN·m ⁻¹]	
	Harmonic-mean equation	Geometric-mean equation
PLA/PA11	2.5	1.3
PLA/HNT	8.7	5.0
PA11/HNT	4.5	2.3

$$\gamma_{12} = \gamma_1 + \gamma_2 - 4 \left(\frac{\gamma_1^{\text{d}} \gamma_2^{\text{d}}}{\gamma_1^{\text{d}} + \gamma_2^{\text{d}}} + \frac{\gamma_1^{\text{p}} \gamma_2^{\text{p}}}{\gamma_1^{\text{p}} + \gamma_2^{\text{p}}} \right) \quad (2)$$

$$\gamma_{12} = \gamma_1 + \gamma_2 - (\sqrt{\gamma_1^{\text{d}} \gamma_2^{\text{d}}} + \sqrt{\gamma_1^{\text{p}} \gamma_2^{\text{p}}}) \quad (3)$$

In this work, surface energy values of PLA, PA11 and HNTs are taken from the literature [18–20] (Table 1) and those values are used to calculate interfacial energy (Table 2). Based on interfacial energies, the wetting coefficient (ω_a) was calculated according to Equation (1). Its value is 1.69 and 2.11 using harmonic-mean Equation (2) and geometric-mean Equation (3), respectively. Therefore, the theoretical calculation indicates that HNTs preferentially locate in the PA11 phase during the melt-blending processing.

3.2. Morphology

Figure 2 shows representative SEM images of the cryo-fractured PLA/PA11 blends with and without HNTs in both transversal (perpendicular to injection molding) and longitudinal (along the injection molding) directions. It is well known that the mechanical properties of blends are strongly dependent on their morphology and the control of the morphology is crucial for the final properties of the product [21–23]. In case of neat blends, PA11 is dispersed in PLA matrix. The transversal images (Figure 2a) show a ‘sea–island’ morphology of the blends, where the continuous phase is PLA and the spherical dis-

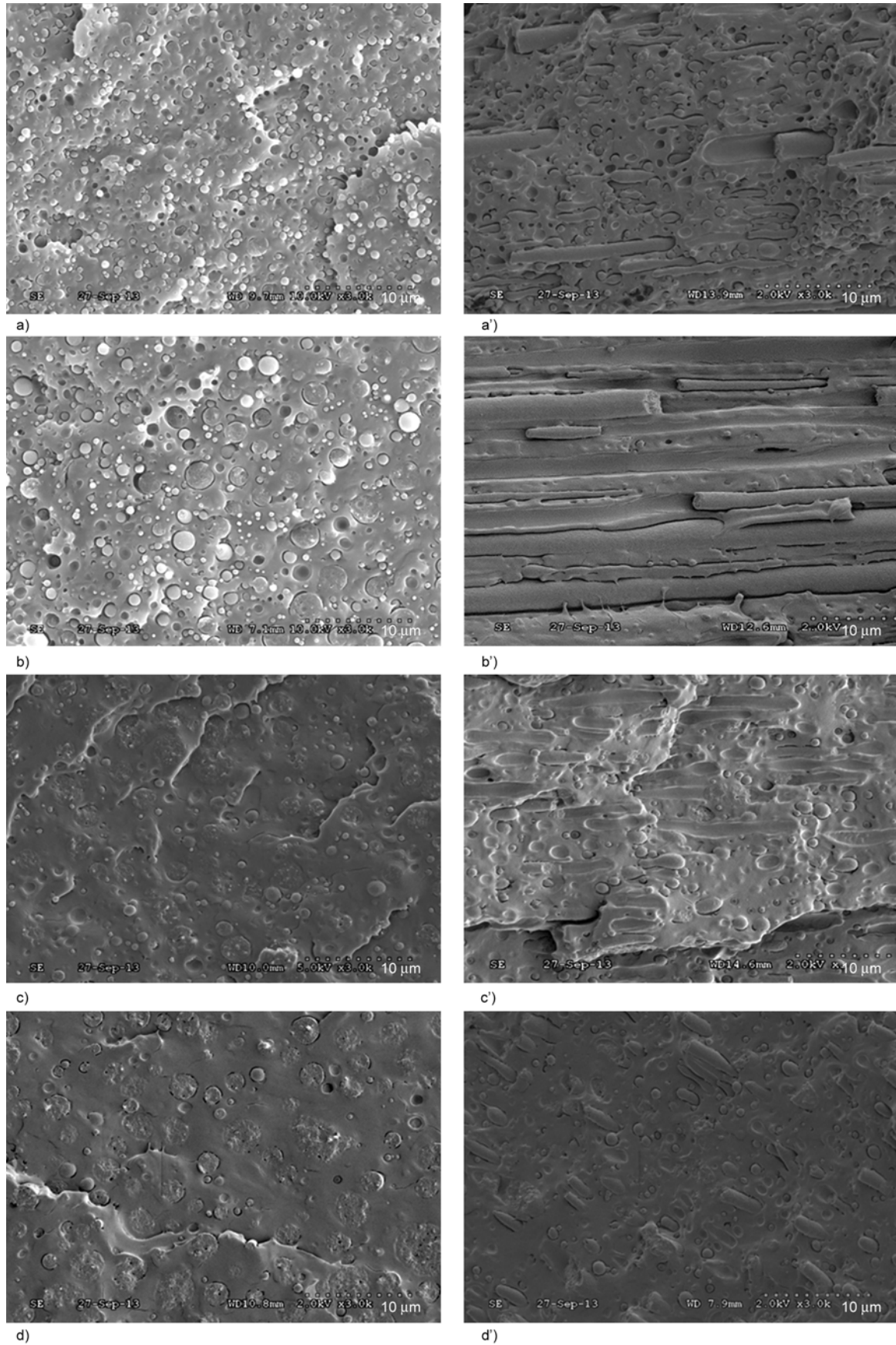


Figure 2. SEM images of PLA/PA11/HNT systems in transversal (a, b, c, d) and in longitudinal (a', b', c' and d') directions. (a, a') Neat blend; (b, b') with 2 wt% HNTs; (c, c') with 4 wt% HNTs; (d, d') with 6 wt% HNTs.

persed phase represents PA11. In the longitudinal direction (Figure 2a'), an heterogeneous discontinuous fibrillar morphology is observed which is attributed to the viscosity difference between the PLA and PA11 [24]. Whatever the observation direction, the interface between PA11 and PLA seems to be weak, a clear gap between the PLA matrix and the PA11 domains being clearly observed. This means that PLA and PA11 are not totally miscible.

The incorporation of HNTs leads to a totally different phase structure. The droplet size increases slightly (Figure 2b). This is due to the fact that, when added to PLA/PA11, all HNTs migrate into PA11 phase due to their affinity towards PA11 and remain trapped inside the PA11 phase, thereby increasing the droplets size. Also, increase in HNTs content enhances the droplets viscosity (see section 3.4) and their resistance to breakup, leading to enlarged dispersed phase.

Also, longitudinal section shows that irregular cylindrical structures of PA11 in flow direction turned out to regular fibrillar structures upon addition of 2 wt% HNTs (Figure 2b') compared to the binary PLA/PA11 blend. However, with increase in HNT concentration to 4 and 6 wt% (c, c' and d, d'), discontinuous fibrillar structure is observed, which is similar to that of the neat blends.

Figure 3 shows the SEM images of neat blends and 6 wt% HNTs-filled blend with higher magnification. HNTs are hardly visible in the PLA matrix, confirming that during processing migration of HNTs from PLA/HNT masterbatch to PA11 matrix has happened, and that HNTs are largely localized in PA11 domain forming interesting 'salami-like' structure

(Figure 3b). In general, the localization of nanofillers in polymer blends should be linked to the balance of interactions between the surface of the nanofillers and the polymer components and wettability factor [25]. As predicted earlier, HNTs are selectively localized inside PA11 (shown in Figure 3a and 3b) and at the interface. This is attributed to HNTs affinity towards PA11 which is higher than that towards PLA. Further morphological observations show that, the interface between neat PLA and PA11 is not sharp, indicating the partial compatibility or weak interaction between PLA and PA11 components (Figure 2a), but with the addition of HNTs this interface quality tends to improve. The difference compared to PLA/PA11 blends without HNTs is that, the PA11 phase holds tightly with the PLA phase, indicating that the interface between the PLA and PA11 phases with the addition of HNT is much stronger than for the binary blend without HNTs.

The selective confinement of HNTs in the PA11 phase is further proved by characterizing the samples using transmission electron microscopy (TEM). The cross-section of PLA/PA11 blend exhibits regular drop-matrix morphology with micro-sized PA11 domains in the continuous PLA matrix (Figure 4a). Upon addition of 2 wt% HNTs into the blends, HNTs appear selectively confined inside the PA11 phase (Figure 4b), while almost no nanotubes can be noticed within the PLA phase. Interestingly, only ultra-micron-sized PA11 droplets are unfilled, which is not surprising, as the length/size of PA11 droplets should be greater than that of HNTs in order to accommodate nanotubes in their domain. Further, upon addition of 4 wt% HNTs, the size of the HNTs-

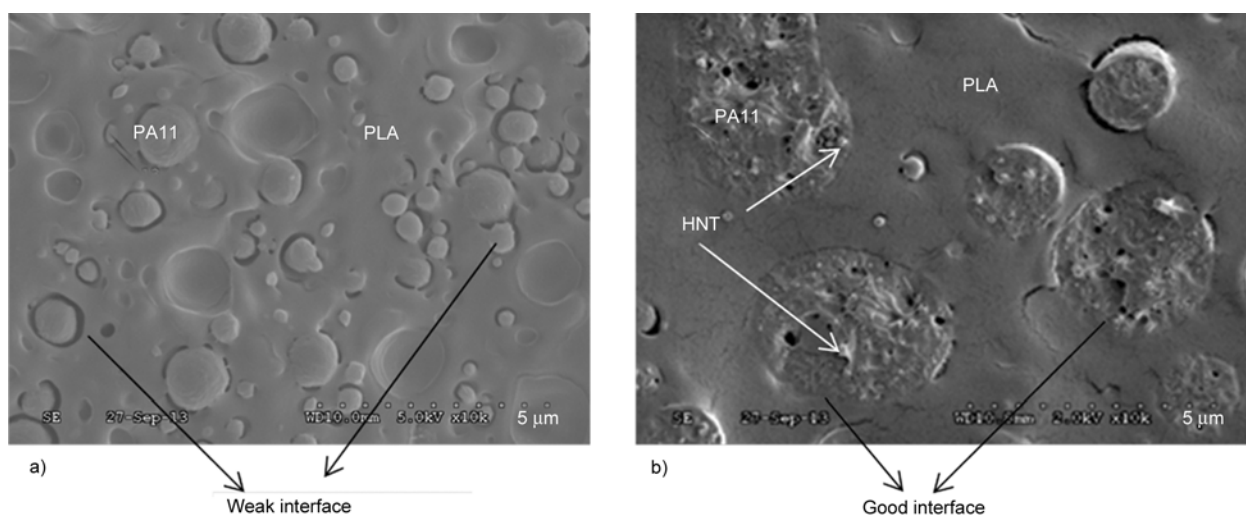


Figure 3. SEM images in transversal direction: (a) PLA/PA11 with weak interface and (b) PLA/P11/6 wt% HNT systems showing a good interface with salami like structure

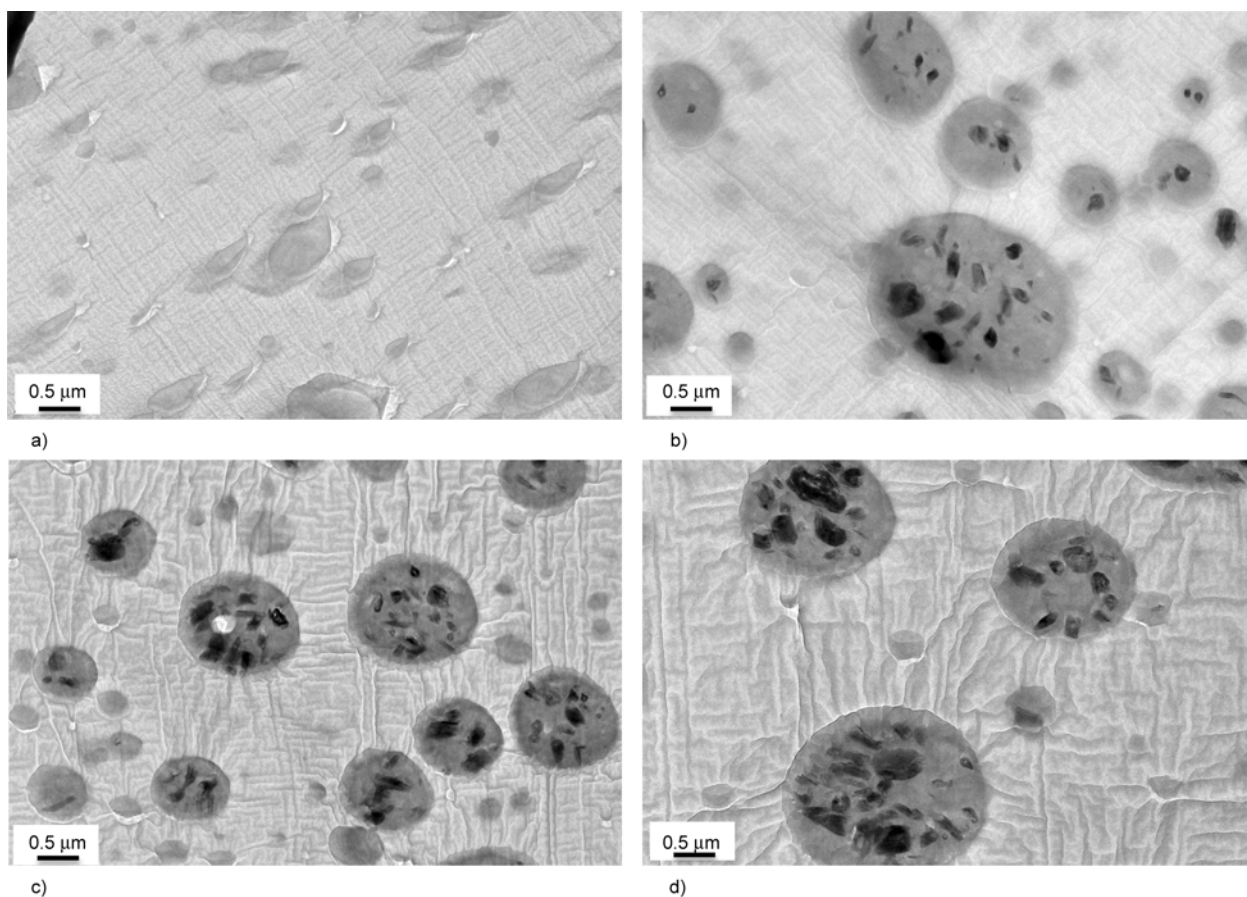


Figure 4. TEM images in transversal direction: (a) PLA/PA11, (b) PLA/PA11/2 wt% HNT, (c) PLA/PA11/4 wt% HNT and (d) PLA/PA11/6 wt% HNTs

filled PA11 droplets slightly increases while the number of unfilled PA11 droplets substantially decreases (Figure 4c). Finally, for 6 wt% HNTs, the size of the HNTs-filled PA11 droplets further increases while only traces of unfilled PA11 droplets are observed (Figure 4d). These observations clearly indicate that the presence of the HNTs in the PLA/PA11 blends creates a regular morphology, which still depends on the halloysite content. Also, at higher loading, HNTs form a network structure in the nanocomposites.

3.3. Thermal behavior

Thermal behavior of PLA/PA11 blend and its nanocomposites was investigated by DSC. The heating and cooling thermograms are shown in Figure 5 and corresponding data are summarized in Table 3. In heating endotherm (Figure 5a), one can see one exotherm corresponding to cold crystallization of PLA (T_{cc}). Comparing the thermograms (Figure 5a) and calorimetric parameters (Table 3), the influence of HNTs on the cold crystallization of the PLA in PLA/PA11 hybrid blends is clearly visible. When HNTs

are added, the T_{cc} of the PLA decreases from 105 to 97°C. The crystallization enthalpies also decrease in the nanocomposites. The decrease of the T_{cc} in the neat blend may be explained as follows. Presence of amorphous PA11 chains could activate the chain mobility of PLA, thereby advancing the cold crystallization of PLA. Furthermore, the surface of the dispersed PA11 domains might also act as nucleating centers and thereby enhance the crystallization of the PLA in the blends, which is accordance with the reported literature [26]. Then, decrease in T_{cc} in ternary nanocomposites is due to characteristic changes of PA11 phase related to migration of HNTs to PA11 matrix bringing further decrease in T_{cc} of PLA phase. Two peaks appearing at about ~52 and ~60°C correspond to the glass transition temperatures (T_g) of PA11 and PLA phases respectively. Addition of HNT has no profound effect on the T_g of the blends. However a marginal increase was observed at high HNT content (~54°C for PA11 and 61.5°C for PLA). This is probably due to the indirect nucleation effect exerted by HNTs. Two endotherms corresponding to melting temperature (T_m) of PLA

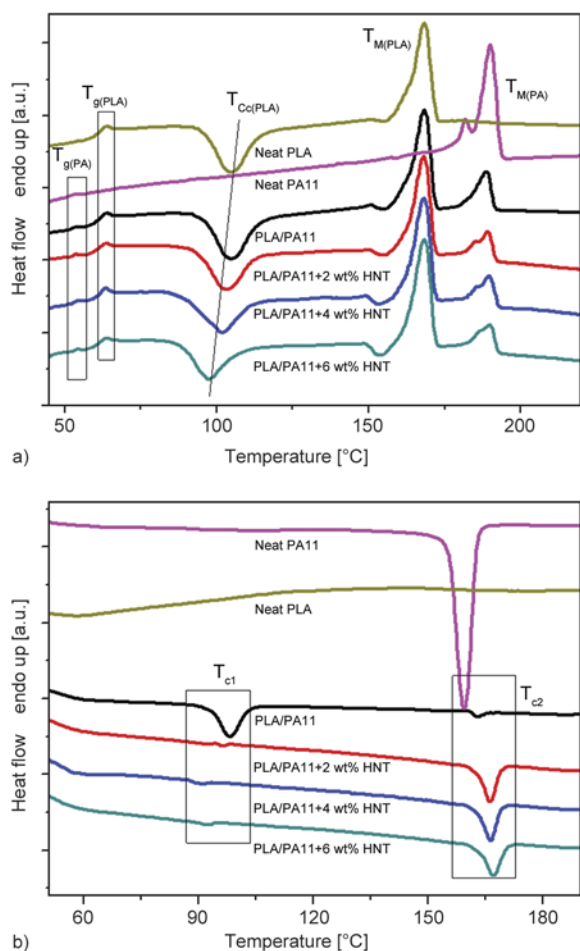


Figure 5. DSC thermograms (a) second heating scan and (b) cooling curves for PLA/PA11/HNT systems with different HNT concentrations

($\sim 168^\circ\text{C}$) and PA11 ($\sim 189^\circ\text{C}$) are visible. The melting temperature remains unaltered with increasing filler concentration. The appearance of shoulder peak in PA11 is attributed to the melting of preferentially oriented PA11 macromolecules. This preferential orientation is inhibited in presence of PLA showing a single peak in PLA/PA11. But, upon addition of HNTs, preferential orientation reappears, which is in accordance with the literature [27]. The intensity of

shoulder peak increases with increasing filler concentration.

During cooling (Figure 5b), the neat PLA/PA11 blend shows two peaks, one big at $\sim 98^\circ\text{C}$ and another small one at around 165°C indicating the fractionated crystallization of PA11. Crystallization at the higher temperature corresponds to bulk crystallization of PA11, which takes place due to effective heterogeneity in the PA11 phase, and crystallization at the lower temperature corresponds to crystallization of PA11 droplets, which needs much larger supercooling [13, 27]. The fractionated crystallization process becomes less evident when the HNTs are added with a reduced peak at 98°C indicating a lower number of fine droplets as observed in TEM image (Figure 4), while peak at 165°C increases drastically. This change in crystalline structure is very important as it governs the mechanical performances of polymer systems. Addition of filler not only alters blend microstructure, but also affects the crystallization behavior of the polymer phases. This further indicates that, HNTs are selectively localized in PA11 matrix as observed in Figures 2 and 4. For neat PLA, no crystallization exothermic peak can be seen as PLA is completely amorphous, due to its slow crystallization kinetics [6, 28, 29]. Addition of filler does not induce any crystallization in PLA phase.

3.4. Rheological behavior

Figure 6 shows the storage modulus (G') and the complex viscosity (η^*) as a function of frequency for PLA/PA11 blends with and without HNTs. Upon addition of 2 and 4 wt% HNTs, G' does not change apparently (Figure 6a), whereas it largely increases at relatively lower frequency for 6 wt% HNTs. A plateau is observed in that case at low frequency, indicating the formation of a percolated network structure of the HNTs in the melt. These inconsistent variations of storage modulus with increasing content

Table 3. Thermal properties of PLA/PA11/ HNT ternary systems

Material	Second heating [°C]						Cooling [°C]			
	$T_{M(PLA)}$	$T_{M(PA)}$	T_{cc}	$\Delta H_{cc(PLA)}$	$T_{g(PA)}$	$T_{g(PLA)}$	$T_{C1(PA)}$	$T_{C2(PA)}$	$\Delta H_{C1(PA)}$	$\Delta H_{C2(PA)}$
PLA	168	–	106	–	–	60	–	–	–	–
PA11	–	190	–	–	54	–	–	159	–	39
PLA/PA11	168	189	105	15	52	60	98	165	13.2	0.4
PLA/PA11/2 wt% HNT	168	189	103	10	53.4	61	96	167	0.3	5.1
PLA/PA11/4 wt% HNT	167.7	189.7	102	10.2	53.5	61	93	168	0.2	5.2
PLA/PA11/6 wt% HNT	168	190	97	13.7	53.8	61.5	92	168	0.2	5.5

ΔH_{cc} cold crystallization enthalpy of PLA, ΔH_{C1} & ΔH_{C2} crystallization enthalpy of PA11

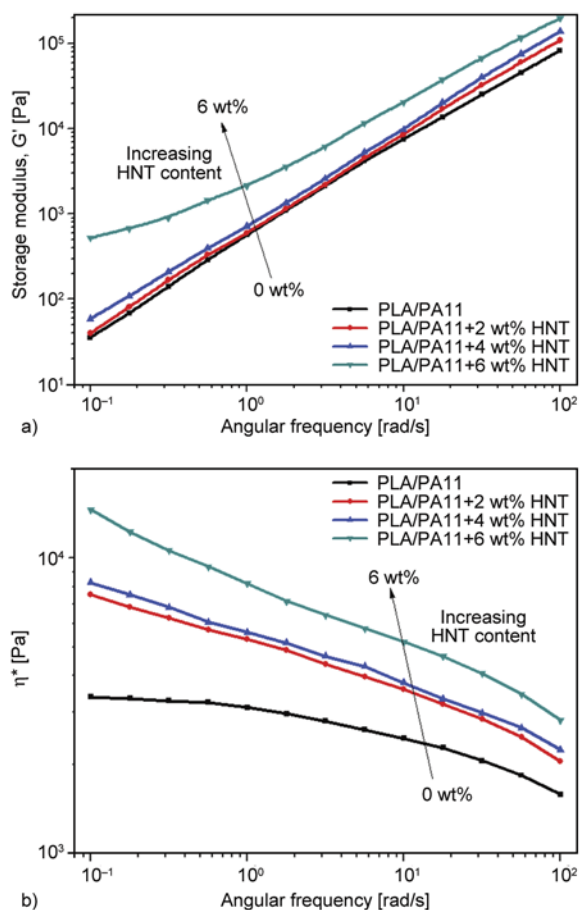


Figure 6. Storage modulus (G') (a) and complex viscosity (η^*) (b) of PLA/PA11/HNT systems with frequency sweep as a function of HNT content at 205°C

of the HNTs may be explained as follows. The original aspect ratio of HNTs is very low (between 10 and 30) and very high loading is necessary to see substantial increase in the storage modulus at low frequency [30]. Therefore, in spite of good distribution of PA11 in PLA phase (Figure 2) and uniform dispersion of HNTs in PA11 at 2 and 4 wt% HNTs contents, the effect of the HNTs on the rheological properties of nanocomposites is not visible and hence in this case, rheological properties of the material are mainly governed by PLA matrix. At 6 wt% HNTs, the presence of a large number of HNTs in PA11 phase induces the formation of percolated network structure and the rheological properties of material are determined by both PLA and HNTs-filled PA11 components. Consequently, pseudo-solid-like behavior is observed in 6 wt% HNTs-filled PLA/PA11 blend only.

The frequency dependency of the complex viscosity (η^*), for all samples is shown in Figure 6b. Upon introduction of HNTs, viscosity of the blend increases

and the shear-thinning behavior is intensified with increase in the nanotubes concentration. Higher viscosity of nanocomposites arises from the network structure of HNT-rich PA11 phase as observed from the morphological images of the nanocomposites (section 3.2). Another possible reason for increased viscosity of nanocomposites is the higher flow resistance of macromolecules due to the interaction between HNTs and the polymer [27]. Both storage modulus and complex viscosity are the highest for 6 wt% HNTs. The increase in the storage modulus (G') and the complex viscosity (η^*) is ascribed to the interfacial interactions between polymer chains and filler surface [30, 31].

3.5. Viscoelastic properties

During dynamic mechanical analysis (DMA) (Figure 7), storage modulus (E') of all the samples logically decreases with increasing temperature and a more rapid drop occurs at glass transition region of PLA. Addition of HNTs to the PLA/PA11 blend increases the storage modulus in the glassy region (Figure 7a) and increase in HNTs concentration further increases the storage modulus of the blends, which can be attributed to the mobility restriction of the polymer chains. Due to selective positioning of HNTs in PA11 matrix coupled with their nucleating action, HNTs not only reinforce the polymers blend but also increases the size of the PA11 phase in PLA matrix.

The temperature dependence of $\tan \delta$ of PLA/PA11 blend and ternary nanocomposites are presented in Figure 7b. The $\tan \delta$ curves show two dynamic relaxation peaks. The peak observed at 65–68°C is often interpreted as the T_g of PLA. This peak does not shift upon HNTs addition, indicating that the presence of the HNTs does not affect significantly the T_g of PLA, which is slightly higher than that obtained from DSC data (Table 3). However, addition of HNTs considerably lowers the intensity of the $\tan \delta$ peak (Figure 7b); the higher the HNTs content, the lower is the peak intensity. The damping behavior of the material is reduced, because the presence of well dispersed HNTs localized in PA11 fibrils retards the segmental motions of the polymer matrix during the transition, thus resulting in the reduction of sharpness and height of the $\tan \delta$ peak [32, 33]. This is in agreement with the significant increase in the elastic component due to the presence of the HNTs in the blends [34].

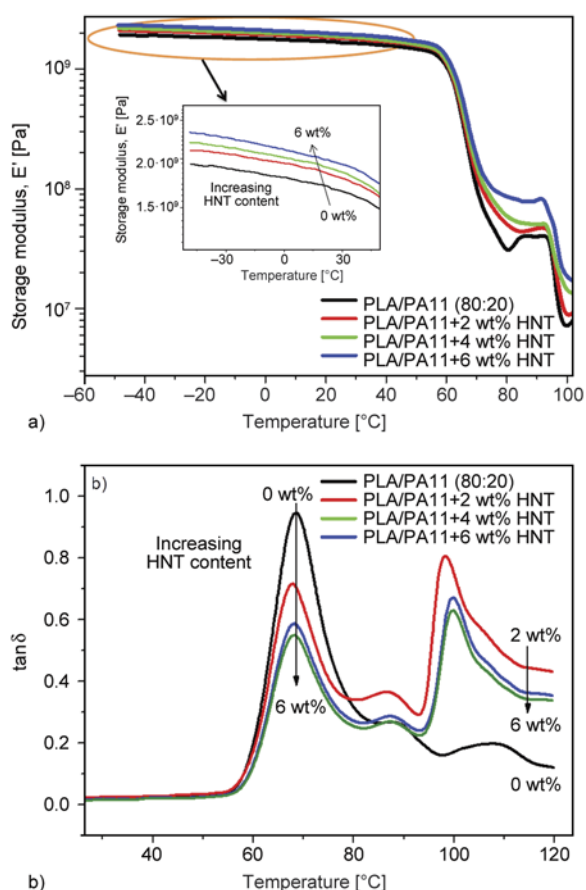


Figure 7. Storage modulus (a) and $\tan \delta$ (b) versus temperature for PLA/PA11/HNT systems

The other peak appearing at 105°C for the PLA/PA11 blend is due to the cold crystallisation of the PLA. Its intensity also decreases with increase in HNTs content. This confirms the previous DSC analysis indicating that HNTs act as a nucleating agent for the crystallisation of PLA. The fact that HNTs act as both reinforcing filler and indirect nucleating agent for crystallisation of PLA is quite interesting, considering the fact that HNTs localize only in PA11 domain as observed by SEM and TEM.

3.6. Mechanical behavior

The mechanical behavior of injection-molded PLA/PA11 (80/20) blends and nanocomposites was

assessed using tensile and impact tests. The mechanical properties (tensile strength, Young’s modulus, strain-at-break, and impact resistance) of the materials are shown in Table 4.

Tensile behavior

The typical tensile stress–strain curves of the PLA/PA11 blends and its nanocomposites are shown in Figure 8. During tensile tests, all the samples showed distinct yielding and stable neck growth with characteristics of a ductile fracture. The neat PLA is a brittle polymer with poor ductility (3.96%) and high strength (54 MPa) (Table 4). When PLA is blended with PA11 the ductility increases up to 79% without significant change in the tensile strength and with only a slight (about 10%) reduction in the modulus. Derho *et al.* [8] reported the brittle fracture for PLA/PA11 (80:20) blends, with decrease in elongation at break due to the presence of micron-sized PA11 nodules in PLA matrix. On the contrary and interestingly in the present work, the PA11 phase appears in elongated/stretched structure (quasi-fibrillar) (Figure 2). Therefore, mixing PLA with PA11 at 80:20 ratio changes the brittle fracture of neat PLA to the ductile fracture of the PLA/PA11 blend.

Also, the tensile behavior of the nanocomposite blends varies significantly with different HNT load-

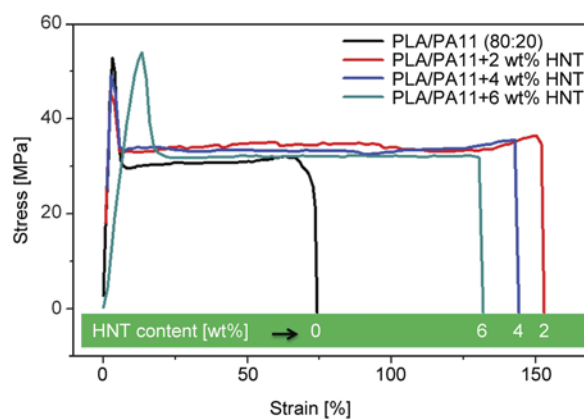


Figure 8. Tensile stress–strain curves of PLA/PA11/HNT systems

Table 4. Mechanical properties of PLA/PA11/ HNT ternary systems

Sample	Tensile strength [MPa]	Elongation at break [%]	Young’s modulus [MPa]	Notched impact resistance [kJ·m ⁻²]	Un-notched impact resistance [kJ·m ⁻²]
PLA	54.5±1.6	3.6±0.2	2923±14	3.1±0.3	16.4±2
PA11	43.7±2.5	254±7	1220±12	–	–
PLA/PA11 (80:20)	53.5±2.5	79±7	2569±12	3.4±0.4	19.0±2
PLA/PA11/2 wt% HNT	54.5±1.5	155±8	2782±11	5.6±0.4	37.0±2
PLA/PA11/4 wt% HNT	53.6±2.6	145±4	2879±21	4.8±0.6	29.2±3
PLA/PA11/6 wt% HNT	54.2±1.1	139±4	2974±14	4.4±0.6	27.8±3

ings. Upon HNTs addition into PLA/PA11 blend, ductility of the material increases dramatically. Compared to neat blend, the elongation at break for the 2 wt% HNTs-filled PLA/PA11 samples almost doubles, increasing from 79 to 155 %, and the modulus increases by ~8% without change in tensile strength. This is due to the fact that, HNTs induced almost uniform PA11 fibrillation in PLA matrix (Figure 2b'). On further increase in HNTs content, a slight decrease in elongation at break is noticed, hardly significant i.e. 145% for 4 wt% HNTs and 139% for 6 wt% HNTs-filled PLA/PA11 blends. This could be due to overloading of HNTs that may induce formation of aggregates or cause damage to PA11 fibrils leading to early fracture of samples. However, decrease in ductility is not eminent; elongation at break remains higher than that of the neat blend. The Young's modulus of the PLA/PA11 blend further increases with increase in HNTs content without altering tensile strength displaying a positive combination of yield stress and strain at break resulting in an optimum filler content (~2 wt%) to achieve balanced tensile properties.

In order to understand further the effect of elongated/stretched PA11 phase with and without HNTs on tensile properties of the blends, the necked down region of the tensile specimen was cryo-fractured longitudinally and morphologies were character-

ized using SEM (Figure 9). Neat blends during the tensile test showed a fracture surface with stretched PA11 phase. Debonding of the PA11 from the PLA matrix under tensile stress is clearly observed. As explained earlier (section 3.2), the original fibrillar structure is not uniform and it remains the same even after stretching. PLA/ PA11 blends with 2 wt% HNT have the highest elongation at break, and HNTs-filled PA11 phase experiences tremendous plastic deformation in the loading direction. All the PA11 fibrils show a uniform stretching without any debonding between PA11 and PLA. No HNTs are visible on the surface of PA11 fibrils, which confirms the greater affinity of HNTs towards PA11. This effectively facilitates the bridging of necking zone by continuous stretching of PA11 with HNTs alignment as the deformation zone propagates along the triaxial deformation. This phenomenon provides a continuous stretching and orientation in the deformation zone, which greatly enhances the ductile characteristics of the PLA/PA11 blends. In case of 4 wt% HNTs and 6 wt% HNTs-filled PLA/PA11 blends, the fractured morphology is quite similar, which is a reflection of their tensile properties (Table 4). In both cases, diameters of the fibrils are much bigger due to overloading of HNTs and there exist a mismatch between the stretching of PA11 and HNTs alignment during the tensile deforma-

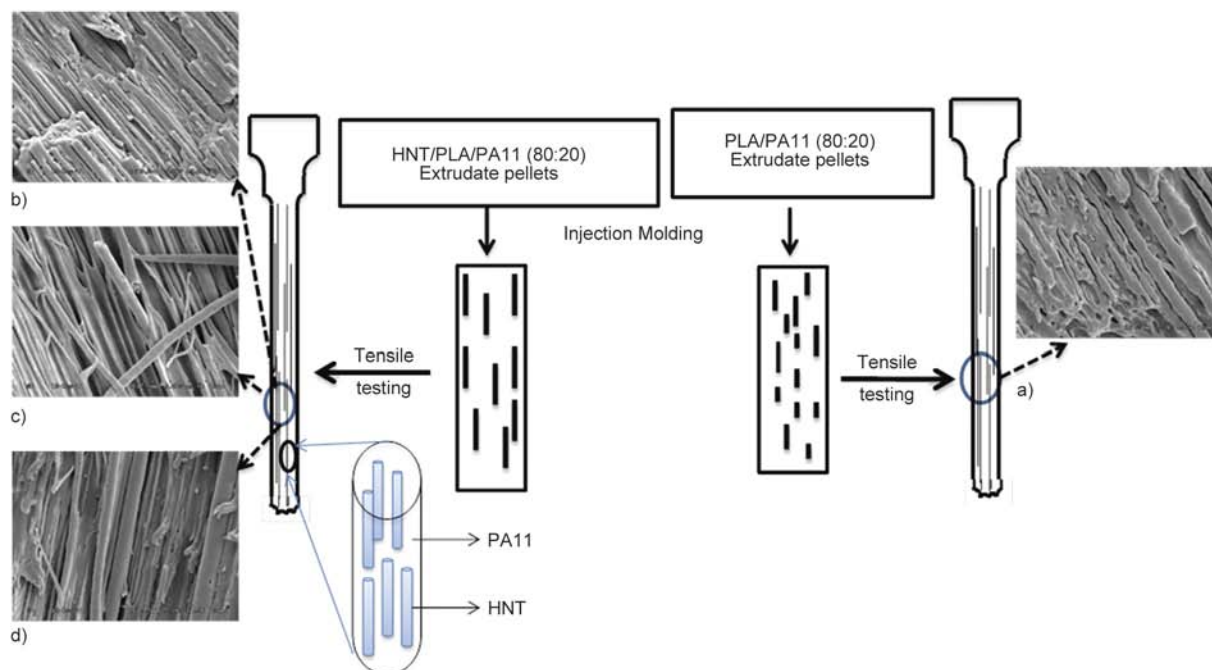


Figure 9. Fracture mechanism of longitudinally cryo-fractured tensile failed samples-right: deformation of PA11 phase in PLA (a) PLA/PA11 (80:20)-left: deformation of HNTs localized in PA11 dispersed in PLA (b) PLA/PA11/2 wt% HNT, (c) PLA/PA11/4 wt% HNT and (d) PLA/PA11/6 wt% HNT

tion, which eventually causes an early failure of the sample.

Impact properties

Table 4 shows the notched and un-notched Charpy impact strength of PLA/PA11 blend and its nanocomposites. PLA is known for its brittle characteristics; therefore, toughening agents are widely used to enhance the PLA impact strength [35–37]. Considering the tensile elongation at break results, PA11 may be expected to be a good candidate for blending with PLA to increase the PLA toughness. Nevertheless, both notched and un-notched Charpy impact strength of unfilled blend are not as good as

expected (3.4 and 19 kJ·m⁻² in notched and un-notched specimens respectively), only slightly higher than neat PLA. By introducing 2 wt% HNTs to PLA/PA11 blends, the notched impact strength increases by + 67% and the un-notched impact strength by + 95%. HNTs effectively toughen the matrix through the stretching of PA11 phase. Further increasing the concentration of the HNTs does not increase the impact strength. Slight decrease in the impact strength (both notched and un-notched) of 4 and 6 wt% HNTs-filled PLA/PA11 blends may be attributed to the excessive localization of HNTs in PA11 phase, as discussed earlier in the tensile properties section. The elongation at break for the blend con-

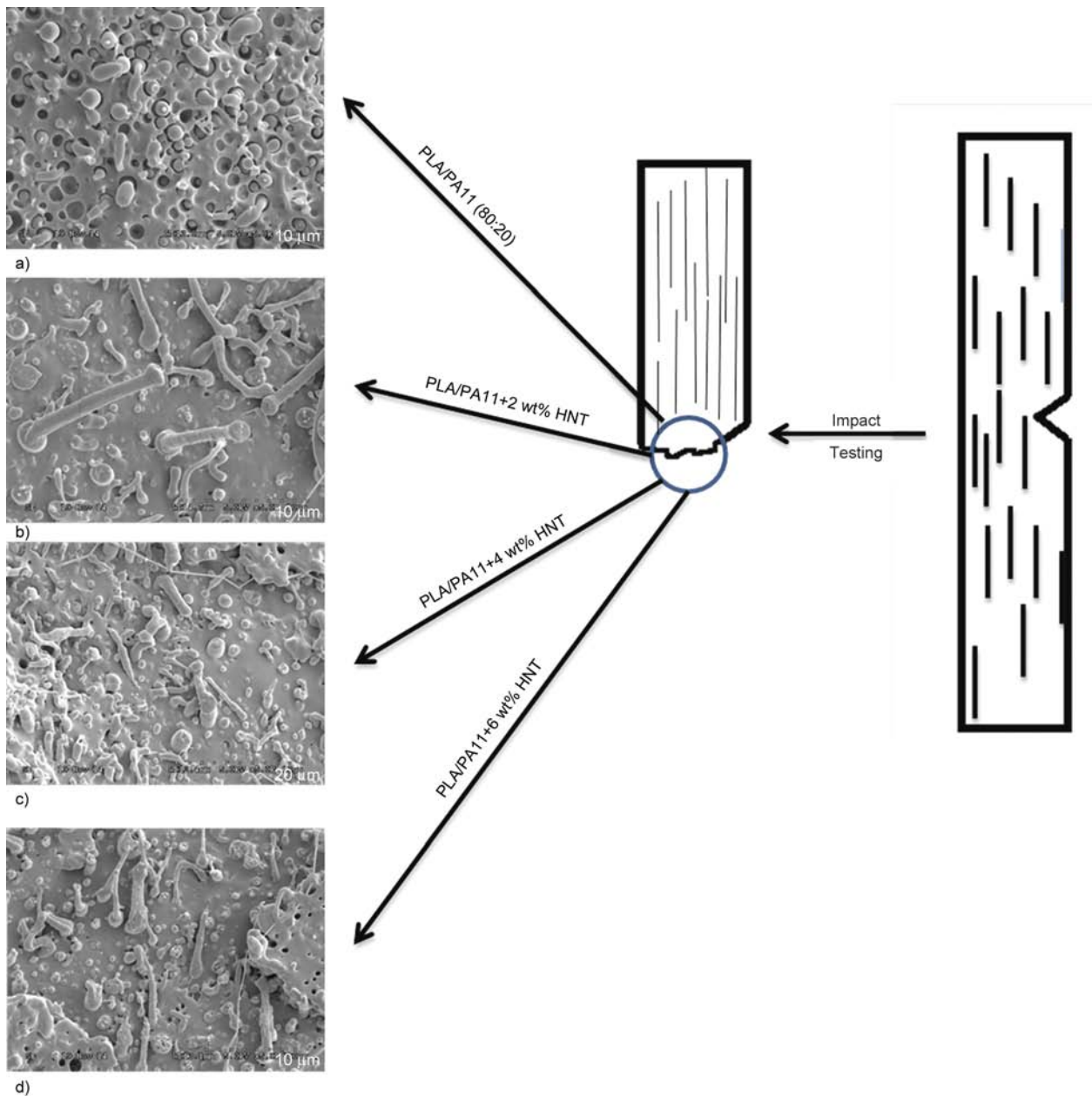


Figure 10. Fracture mechanism of impact failed samples – deformation of phase of PA11 in PLA: (a) PLA/PA11 (80:20), (b) PLA/PA11/2 wt% HNT, (c) PLA/PA11/4 wt% HNT and (d) PLA/PA11/6 wt% HNT

taining 4 and 6 wt% HNTs showed similar trend as that of the impact strength. These results are in accordance with those obtained for the clay filled poly(L-lactide)/polypropylene blends [4].

The fracture surface was observed in the vicinity of the notch under SEM (Figure 10). The neat blend shows a fracture surface with multiple-sized elongated PA11 fibrils. The toughening effect in this case remains moderate due to the lower compatibility between the phases. Some voids due to pullout of dispersed PA11 domain are clearly observed, which suggests a poor interfacial adhesion between PLA and PA11 phases. In comparison to neat blend, the compound containing 2 wt% HNTs shows numerous fibrils which are stretched on the fracture. No obvious interface between the different phases is observed between the PLA and the HNTs-filled PA11 phases. In case of 4 wt% HNTs and 6 wt% HNTs-filled PLA/PA11 blends, the fractured morphology is similar (Figure 10) to that of tensile failed samples. In both the cases, although good adhesion between fibrils and matrix was observed, stretching of fibrils was limited due to high filler content.

4. Conclusions

A fully bio-based blend with PLA as the dominant component with improved ductility and impact strength and unaltered tensile strength and stiffness was produced by blending amorphous brittle PLA with semi-crystalline PA11 and natural halloysite nanotubes (HNTs). Blending PLA and PA11 at 80:20 ratio leads to the formation of an irregular fibrillar structure due to the viscosity ratio of the two thermoplastics. PLA ductility increases (tensile elongation at break being multiplied by a factor 20), however at the slight expense of strength and stiffness. This fibrillar structure of the PLA/PA11 blend is kept upon addition of HNTs, but the morphology becomes interestingly more regular at 2 wt% HNTs. As predicted by thermodynamics rules, microscopic observations confirm that HNTs are selectively located in the PA11 phase. Such a regular fibrillar structure associated with the polymers interface improvement leads to significantly enhanced toughness of the brittle neat PLA. Elongation at break in tension increases from 3.6% (neat PLA) to 155% (PLA/PA11 + 2wt% HNT) without sacrificing tensile strength or Young modulus. In the same time, impact resistance is multiplied by 2. So, proper selection of bio-based PLA and PA11 blend composition and

addition of naturally available HNTs, which positively alter the microstructure of blend, may effectively result in ‘engineered’ materials with significantly enhanced mechanical properties.

Acknowledgements

Authors would like to thank International Campus on Safety and Intermodality in Transportation (CISIT), Nord-Pas-de-Calais Region and European Community (FEDER). The authors sincerely acknowledge Dr. Rajashekhara Shabadi, Unité Matériaux et Transformations, Université Lille1 (France), for his precious help in TEM observations.

References

- [1] Soulestin J., Prashantha K., Lacrampe M. F., Krawczak P.: Bioplastics based nanocomposites for packaging applications. in ‘Handbook of bioplastics and biocomposites engineering applications’ (Ed.: Pilla S.) Wiley, New York, 76–119 (2011)
DOI: [10.1002/9781118203699.ch4](https://doi.org/10.1002/9781118203699.ch4)
- [2] Rusu D., Boyer S. A. E., Lacrampe M. F., Krawczak P.: Bioplastics and vegetal fiber reinforced bioplastics for automotive applications. in ‘Handbook of bioplastics and biocomposites engineering applications’ (Ed.: Pilla S.) Wiley, New York, 397–449 (2011).
DOI: [10.1002/9781118203699.ch15](https://doi.org/10.1002/9781118203699.ch15)
- [3] Nijenhuis A. J., Colstee E., Grijpma D. W., Pennings A. J.: High molecular weight poly(L-lactide) and poly(ethylene oxide) blends: Thermal characterization and physical properties. *Polymer*, **37**, 5849–5857 (1996).
DOI: [10.1016/S0032-3861\(96\)00455-7](https://doi.org/10.1016/S0032-3861(96)00455-7)
- [4] Pulapura S., Kohn J.: Trends in the development of bio-resorbable polymers for medical applications. *Journal of Biomaterials Applications*, **6**, 216–250 (1992).
DOI: [10.1177/088532829200600303](https://doi.org/10.1177/088532829200600303)
- [5] Zhang L., Gon S. H., Lee S. Y.: Miscibility and crystallization behaviour of poly(L-lactide)/poly(*p*-vinylphenol) blends. *Polymer*, **39**, 4841–4847 (1998).
DOI: [10.1016/S0032-3861\(97\)10167-7](https://doi.org/10.1016/S0032-3861(97)10167-7)
- [6] Ebadi-Dehaghani H., Khonakdar H. A., Barikani M., Jafari S. H.: Experimental and theoretical analyses of mechanical properties of PP/PLA/clay nanocomposites. *Composites Part B: Engineering*, **69**, 133–144 (2015).
DOI: [10.1016/j.compositesb.2014.09.006](https://doi.org/10.1016/j.compositesb.2014.09.006)
- [7] Arrieta M. P., Fortunati E., Dominici F., Rayón E., López J., Kenny J. M.: Multifunctional PLA–PHB/cellulose nanocrystal films: Processing, structural and thermal properties. *Carbohydrate Polymers*, **107**, 16–24 (2014).
DOI: [10.1016/j.carbpol.2014.02.044](https://doi.org/10.1016/j.carbpol.2014.02.044)
- [8] Derho J., Soulestin J., Krawczak P.: Structural evolution of poly(lactic acid)/poly(ethylene oxide)/unmodified clay upon ambient ageing. *Journal of Applied Polymer Science*, **131**, 40426/1–40426/8 (2014).
DOI: [10.1002/APP.40426](https://doi.org/10.1002/APP.40426)

- [9] Pai F.-C., Lai S.-M., Chu H.-H.: Characterization and properties of reactive poly(lactic acid)/polyamide 610 biomass blends. *Journal of Applied Polymer Science*, **130**, 2563–2571 (2013).
DOI: [10.1002/app.39473](https://doi.org/10.1002/app.39473)
- [10] Feng F., Lin Y.: Structure and property of polylactide/polyamide blends. *Journal of Macromolecular Science Part B: Physics*, **49**, 1117–1127 (2010).
DOI: [10.1080/00222341003609179](https://doi.org/10.1080/00222341003609179)
- [11] Stoclet G., Seguela R., Lefebvre J.-M.: Morphology, thermal behavior and mechanical properties of binary blends of compatible biosourced polymers: Polylactide/polyamide11. *Polymer*, **52**, 1417–1425 (2011).
DOI: [10.1016/j.polymer.2011.02.002](https://doi.org/10.1016/j.polymer.2011.02.002)
- [12] Patel R., Ruehle D. A., Dorgan J. R., Halley P., Martin D.: Biorenewable blends of polyamide-11 and polylactide. *Polymer Engineering and Science*, **54**, 1523–1532 (2014).
DOI: [10.1002/pen.23692](https://doi.org/10.1002/pen.23692)
- [13] Nuzzo A., Coiai S., Carroccio S. C., Dintcheva N. T., Gambarotti C., Filippone G.: Heat-resistant fully bio-based nanocomposite blends based on poly(lactic acid). *Macromolecular Materials and Engineering*, **299**, 31–40 (2014).
DOI: [10.1002/mame.201300051](https://doi.org/10.1002/mame.201300051)
- [14] Nuzzo A., Acierno D., Filippone G.: Clay-filled bio-based blends of poly(lactic acid) and polyamide 11. *AIP Conference Proceedings*, **1459**, 208–210 (2012).
DOI: [10.1063/1.4738445](https://doi.org/10.1063/1.4738445)
- [15] Nuzzo A., Bilotti E., Peijs T., Acierno D., Filippone G.: Nanoparticle-induced co-continuity in immiscible polymer blends – A comparative study on bio-based PLA-PA11 blends filled with organoclay, sepiolite, and carbon nanotubes. *Polymer*, **55**, 4908–4919 (2014).
DOI: [10.1016/j.polymer.2014.07.036](https://doi.org/10.1016/j.polymer.2014.07.036)
- [16] Sumita M., Sakata K., Asai S., Miyasaka K., Nakagawa H.: Dispersion of fillers and the electrical conductivity of polymer blends filled with carbon black. *Polymer Bulletin*, **25**, 265–261 (1991).
DOI: [10.1007/BF00310802](https://doi.org/10.1007/BF00310802)
- [17] Wu S.: *Polymer interface and adhesion*. Marcel Dekker, New York (1982).
- [18] Molinaro S.: *Bio-based food packaging films: Influence of formulation and processing on functional properties*. PhD Thesis, University of Udine (2013).
- [19] Lennon P., Espuche E., Sage D., Gauthier H., Sautereau H., Valot E.: Comparison of the wetting behaviour of polyamides presented as particles and films – Influence of a plasma microwave treatment. *Journal of Materials Science*, **35**, 49–55 (2000).
DOI: [10.1023/A:1004728229418](https://doi.org/10.1023/A:1004728229418)
- [20] Wu H., Watanabe H., Ma W., Fujimoto A., Higuchi T., Uesugi K., Takeuchi A., Suzuki Y., Jinnai H., Takahara A.: Robust liquid marbles stabilized with surface-modified halloysite nanotubes. *Langmuir*, **29**, 14971–14975 (2013).
DOI: [10.1021/la4041858](https://doi.org/10.1021/la4041858)
- [21] Dave V., Tamagno M., Focher B., Marsano E.: Hyaluronic acid-(hydroxypropyl)cellulose blends: A solution and solid state study. *Macromolecules*, **28**, 3531–3539 (1995).
DOI: [10.1021/ma00114a006](https://doi.org/10.1021/ma00114a006)
- [22] Nam S. Y., Lee Y. M.: Pervaporation and properties of chitosan-poly(acrylic acid) complex membranes. *Journal of Membrane Science*, **135**, 161–168 (1997).
DOI: [10.1016/S0376-7388\(97\)00144-0](https://doi.org/10.1016/S0376-7388(97)00144-0)
- [23] Yousfi M., Soulestin J., Vergnes B., Lacrampe M.-F., Krawczak P.: Compatibilization of immiscible polymer blends by organoclay: Effect of nanofiller or organo-modifier? *Macromolecular Materials and Engineering*, **298**, 757–770 (2013).
DOI: [10.1002/mame.201200138](https://doi.org/10.1002/mame.201200138)
- [24] Chomat D., Soulestin J., Lacrampe M. F., Sclavons M., Krawczak P.: *In situ* fibrillation of polypropylene/polyamide 6 blends: Effect of organoclay addition. *Journal of Applied Polymer Science*, **132**, 41680/1–41680/13 (2015).
DOI: [10.1002/APP.41680](https://doi.org/10.1002/APP.41680)
- [25] Frieberg B., Kim J., Narayanan S., Green P. F.: Surface dynamics of miscible polymer blend nanocomposites. *ACS Nano*, **8**, 607–613 (2014).
DOI: [10.1021/nn405233a](https://doi.org/10.1021/nn405233a)
- [26] Zhang K., Mohanty A. K., Misra M.: Fully biodegradable and biorenewable ternary blends from polylactide, poly(3-hydroxybutyrate-co-hydroxyvalerate) and poly(butylene succinate) with balanced properties. *ACS Applied Materials and Interfaces*, **4**, 3091–3101 (2012).
DOI: [10.1021/am3004522](https://doi.org/10.1021/am3004522)
- [27] Prashantha K., Lacrampe M.-F., Krawczak P.: Highly dispersed polyamide-11/halloysite nanocomposites: Thermal, rheological, optical, dielectric, and mechanical properties. *Journal of Applied Polymer Science*, **130**, 313–321 (2013).
DOI: [10.1002/app.39160](https://doi.org/10.1002/app.39160)
- [28] Garlotta D.: A literature review of poly(lactic acid). *Journal of Polymers and the Environment*, **9**, 63–84 (2001).
DOI: [10.1023/A:1020200822435](https://doi.org/10.1023/A:1020200822435)
- [29] Lim L.-T., Auras R., Rubino M.: Processing technologies for poly(lactic acid). *Progress in Polymer Science*, **33**, 820–852 (2008).
DOI: [10.1016/j.progpolymsci.2008.05.004](https://doi.org/10.1016/j.progpolymsci.2008.05.004)
- [30] Prashantha K., Lacrampe M. F., Krawczak P.: Processing and characterization of halloysite nanotubes filled polypropylene nanocomposites based on a masterbatch route: Effect of halloysites treatment on structural and mechanical properties. *Express Polymer Letters*, **5**, 295–307 (2011).
DOI: [10.3144/expresspolymlett.2011.30](https://doi.org/10.3144/expresspolymlett.2011.30)
- [31] Schmitt H., Prashantha K., Soulestin J., Lacrampe M. F., Krawczak P.: Preparation and properties of novel melt-blended halloysite nanotubes/wheat starch nanocomposites. *Carbohydrate Polymers*, **89**, 920–927 (2012).
DOI: [10.1016/j.carbpol.2012.04.037](https://doi.org/10.1016/j.carbpol.2012.04.037)

- [32] Liu X., Dever M., Fair N., Benson R. S.: Thermal and mechanical properties of poly(lactic acid) and poly(ethylene/butylene succinate) blends. *Journal of Environmental Polymer Degradation*, **5**, 225–235 (1997). DOI: [10.1007/BF02763666](https://doi.org/10.1007/BF02763666)
- [33] Pothan L. A., Oommen Z., Thomas S.: Dynamic mechanical analysis of banana fiber reinforced polyester composites. *Composites Science and Technology*, **63**, 283–293 (2003). DOI: [10.1016/S0266-3538\(02\)00254-3](https://doi.org/10.1016/S0266-3538(02)00254-3)
- [34] Elwathig H., You W., He J., Yu M.: Dynamic mechanical properties and thermal stability of poly(lactic acid) and poly(butylene succinate) blends composites. *Journal of Fiber Bioengineering and Informatics*, **6**, 85–94 (2013). DOI: [10.3993/jfbi03201308](https://doi.org/10.3993/jfbi03201308)
- [35] Zhang K., Nagarajan V., Misra M., Mohanty A. K.: Supertoughened renewable PLA reactive multiphase blends system: Phase morphology and performance. *ACS Applied Materials and Interfaces*, **6**, 12436–12448 (2014). DOI: [10.1021/am502337u](https://doi.org/10.1021/am502337u)
- [36] Jiang L., Wolcott M. P., Zhang J.: Study of biodegradable polylactide/poly(butylene adipate-*co*-terephthalate) blends. *Biomacromolecules*, **7**, 199–207 (2006). DOI: [10.1021/bm050581q](https://doi.org/10.1021/bm050581q)
- [37] Ishida S., Nagasaki R., Chino K., Dong T., Inoue Y.: Toughening of poly(L-lactide) by melt blending with rubbers. *Journal of Applied Polymer Science*, **113**, 558–566 (2009). DOI: [10.1002/app.30134](https://doi.org/10.1002/app.30134)

Fabrication of polyaniline coated iron oxide hybrid particles and their dual stimuli-response under electric and magnetic fields

B. Sim, H. S. Chae, H. J. Choi*

Department of Polymer Science and Engineering, Inha University, 402-751 Incheon, Korea

Received 13 January 2015; accepted in revised form 9 March 2015

Abstract. Polyaniline (PANI)-coated iron oxide (Fe_3O_4) sphere particles were fabricated and applied to a dual stimuli-responsive material under electric and magnetic fields, respectively. Sphere Fe_3O_4 particles were synthesized by a solvothermal process and protonated after acidification. The aniline monomer tended to surround the surface of the Fe_3O_4 core due to the electrostatic and hydrogen bond interactions. A core-shell structured product was finally formed by the oxidation polymerization of PANI on the surface of Fe_3O_4 . The formation of Fe_3O_4 @PANI particles was examined by scanning electron microscope and transmission electron microscope. The bond between Fe_3O_4 and PANI was confirmed by Fourier transform-infrared spectroscopy and magnetic properties were analyzed by vibration sample magnetometer. A hybrid of a conducting and magnetic particle-based suspension displayed dual stimuli-response under electric and magnetic fields. The suspension exhibited typical electrorheological and magnetorheological behaviors of the shear stress, shear viscosity and dynamic yield stress, as determined using a rotational rheometer. Sedimentation stability was also compared between Fe_3O_4 and Fe_3O_4 @PANI suspension.

Keywords: smart polymers, electrorheology, magnetorheology, polyaniline, iron oxide

1. Introduction

The reversible phase transitions as a response to external stimuli, such as pH, temperature, ionic strength, shear, electric or magnetic fields become a significant area of materials research [1–8]. Electric or magnetic stimuli-responsive suspension systems are particularly noticeable because their dramatic changes in shear viscosity and yield stress under a range of conditions is useful for rheology control applications. For example, suspensions consisting of magnetic particles dispersed in a nonmagnetic liquid have controllable properties under an external magnetic field [9]. If magnetic fields are applied to suspensions, their shear viscosity increases significantly and causes solidification. The magnetic dipole-dipole interactions are induced between the adjacent

magnetic particles and fibrillar structures along the direction of the magnetic fields are formed. Therefore, a liquid-like suspension is transformed quite rapidly to a solid-like state [10]. As soon as the magnetic field is removed, the suspension returns rapidly to its original free flowing liquid state. These suspensions are called magnetorheological (MR) fluids or suspensions. The reversible magnetization and demagnetization upon the application of an external magnetic field applied alters the rheological properties of suspensions. Similar to MR suspensions, electrorheological (ER) fluids are composed of electrically polarizable particles dispersed in an insulating liquid and features electrically reversible and tunable behavior [11].

*Corresponding author, e-mail: hjchoi@inha.ac.kr
© BME-PT

Soft magnetic carbonyl iron (CI) microspheres are the most popular MR materials because of their excellent magnetic behavior but their large density causes severe sedimentation problems. To overcome this drawback, iron oxide (Fe_3O_4) particles, which have lower density but sufficient magnetic properties, were adopted. Furthermore, due to their oxidation state these magnetic particles are not easily affected by the corrosion under acidic conditions compared to the CI particles [12]. Concurrently, as an electroresponsive material, polyaniline (PANI), has been investigated extensively in ER systems [13–15] because of its easy synthesis, good thermal stability, low cost, and reversible doping/dedoping process to control the conductivity. Both ER and MR fluids have been studied extensively but there are only a few reports on electrorheological/magnetorheological (EMR) suspensions. For example, EMR performance-based polypyrrole/ Fe_3O_4 composites [16] and synergistic effect of EMR suspensions have been investigated [17–19].

In this study, PANI-coated Fe_3O_4 particle-based EMR suspensions were prepared. A hybrid of dielectric and magnetic particles revealed dual stimuli-responses. The ER and MR experiments were conducted respectively using a rotational rheometer.

2. Experimental

2.1. Materials and preparation

Spherical Fe_3O_4 microspheres were synthesized using a solvothermal process, in which initially 10.8 g of ferric chloride hexahydrate (Sigma-Aldrich) and 14.4 g of sodium acetate (Sigma-Aldrich) were dissolved in 200 mL of ethylene glycol (Daejung Co. Ltd., Korea) with vigorous stirring. The solution was transferred to a Teflon-lined stainless-steel autoclave, sealed and heated at 200°C for 24 h. The resulting product was washed several times with ethanol and distilled water.

And then, 1 g of Fe_3O_4 was added to a three-neck flask containing 400 mL of HCl (0.1 M, Duksan, Korea) and sonicated for 30 min using a sonication bath (Powersonic 410, 40 kHz, 500 W, Hawshin Tech., Korea) After stirring reactor for 10 h at 5°C, the solution was decanted by the application of an external magnet. Subsequently, 100 mL of anhydrous ethanol and 1 mL of aniline (DC Chemical, Korea) were added to the reactor. The solution was sonicated for 10 min and stirred slowly at 5°C in a nitrogen atmosphere. After being kept for 12 h,

1.7 mL of HCl (12 M) was added, and then 250 mL of ammonium persulfate (0.04 M, Daejung Co., Korea) was also added dropwise over a ca. 30 min period. The mixture was stirred vigorously in a nitrogen atmosphere for 8 h. Finally, the resulting product was collected magnetically and washed with ethanol and distilled water [20].

To prevent dielectric breakdown under applied high electric field strength, we dedoped the particles using 1 M NaOH solution as follows. Once the particles were dispersed in distilled water by adjusting the pH value to 7, they were washed with distilled water several times and then dried in vacuum oven. Their electrical conductivity was measured to be in a semi-conducting region with $5.56 \cdot 10^{-8}$ S/cm.

The EMR suspension was prepared by dispersing the particles in insulating silicone oil (Shin-Etsu silicone, KF-96, kinematic viscosity at 25°C: 50 mPa·s, specific gravity at 25°C: 0.96 g/cm³).

2.2. Characterization

The chemical structure of the PANI-coated Fe_3O_4 was analyzed by Fourier transform-infrared spectroscopy (FT-IR) (VERTEX 80v, Bruker). KBr powder was used to make the pellet and measured by a transmission mode. The morphology and elemental composition were characterized by high resolution-scanning electron microscope (HR-SEM) (SU-8010, Hitachi) combined with an energy dispersive X-ray analyzer (EDS) (EX-250, HORIBA). The transmission electron microscope (TEM) (CM200, Philips) also used to observe core-shell structures. Thermal stability was determined by thermogravimetric analysis (TGA) (STA 409 PC, NETZSCH) heated up to 800°C at a heating rate of 10°C/min under an atmospheric condition. Magnetic properties were examined on the powder state using a vibration sample magnetometer (VSM) (Lakeshore 7307). Gas pycnometer (AccuPyc 1330, Micromeritics) was used to measure the particle density. The ER properties were examined using a rotational rheometer (MCR 300, Anton Paar) connected to a high voltage power supplier (HCN 7E-12 500, Fug) and the suspension was placed in the Couette-type geometry with a bob and cup (CC 17/E, gap distance: 0.71 mm). The MR properties were investigated using a parallel-plate (PP 20, gap distance: 1 mm) geometry equipped with a MR device (Physica MRD 180, Anton Paar). A Turbiscan lab expert system (Turbiscan Classic MA2000, Formulaction) was used to confirm the

sedimentation stability. All characterizations were conducted at room temperature.

3. Results and discussion

The FT-IR spectra confirmed the successful polymerization of aniline onto the Fe_3O_4 surface, as shown in Figure 1. In the Fe_3O_4 @PANI spectrum, the peaks at approximately 3384 cm^{-1} (free N–H stretching vibration band in association with hydrogen bond), 1585 and 1498 ($\text{C}=\text{N}$ and $\text{C}=\text{C}$ stretching vibration of the quinoid and benzenoid ring, respectively), 1304 and 1143 ($\text{C}-\text{N}$ stretching of the secondary aromatic amine), 1247 ($\text{C}-\text{N}$ stretching vibration in protonic acid doped PANI), and 829 cm^{-1} (out of plane deformation of $\text{C}-\text{H}$ in the 1,4-disubstituted benzene ring) were assigned to the characteristics of pure PANI [21, 22]. All of them were blue-shifted compared to the pure PANI peaks (1568 , 1492 , 1303 , and 1135 cm^{-1}) because the N atoms with lone pairs of electrons in PANI are inclined to adsorb to the surface hydroxyls of Fe_3O_4 by hydrogen bonding, which decreases the electron cloud density of $\text{C}=\text{C}$, $\text{C}=\text{N}$ and $\text{C}-\text{N}$ bonds in the conjugated quinoid and/or benzenoid rings. At the same time, the characteristic peak of Fe_3O_4 at 584 cm^{-1} ($\text{Fe}-\text{O}$ stretching) [23] shows a red-shift compared to 592 cm^{-1} for pure Fe_3O_4 due to weakening of the surface $\text{Fe}-\text{O}$ bonds. As a result, the bond between Fe_3O_4 and PANI is a definite combination rather than just a blend of two components [24]. SEM images in Figure 2 present the morphology of particles. Pure Fe_3O_4 is spherical with a grainy surface. After the polymer coating process, the surface of the composite is changed, evidently due to the growth of PANI on the Fe_3O_4 surface. TEM images revealed well-defined core-shell structures of

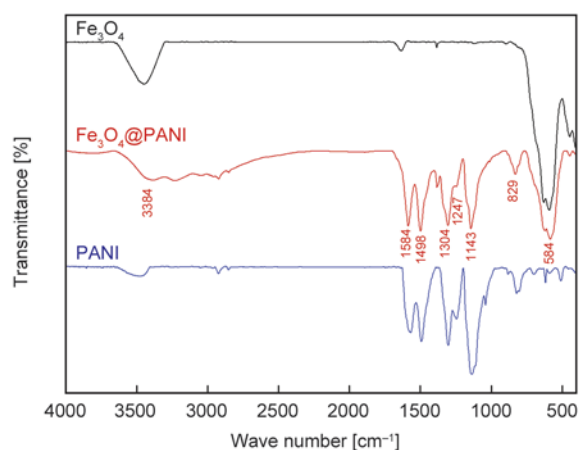


Figure 1. FT-IR spectra of Fe_3O_4 , Fe_3O_4 @PANI and PANI

Fe_3O_4 @PANI. After an acidifying step of the Fe_3O_4 core, the aniline monomer was adsorbed onto the Fe_3O_4 surface through electrostatic and hydrogen bonding. PANI can nucleate and grow on the Fe_3O_4 surface to form a core-shell structure. The core-shell structure can be hardly formed in the absence of protonation of the core. Without an acidifying process of Fe_3O_4 , bare Fe_3O_4 particles are mainly

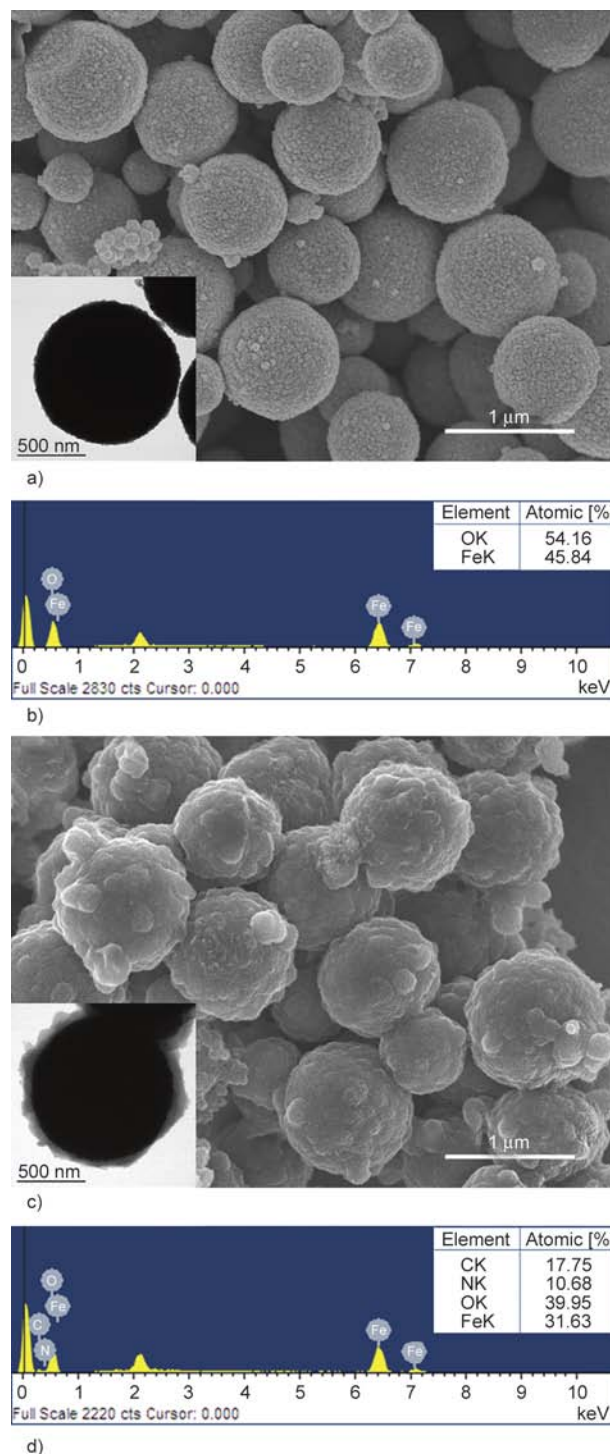


Figure 2. SEM and TEM (inset) images of (a) Fe_3O_4 , (c) Fe_3O_4 @PANI and EDS results of (b) Fe_3O_4 , (d) Fe_3O_4 @PANI (Pt from Pt coating is removed)

formed. This proves that acidification is essential for preparing the $\text{Fe}_3\text{O}_4@\text{PANI}$ structure and those other surfactants are unnecessary [20]. Further composition was analyzed by SEM-EDS spectra. In Figure 2d, the peaks corresponding to C, N, O and Fe confirmed the presence of the PANI coating on the Fe_3O_4 surface, indicating the successful fabrication. To calculate the amount of PANI incorporated on $\text{Fe}_3\text{O}_4@\text{PANI}$, the thermal analysis was carried out as shown in Figure 3. The weight loss around 100°C is attributed to the release of water and dopant from the PANI. The sharp degradation of PANI observed around 350°C and continues to 600°C due to large scale thermal degradation of the PANI chains. $\text{Fe}_3\text{O}_4@\text{PANI}$ underwent a similar decomposition behavior as like PANI, but it possessed an enhanced thermal stability with a slower rate of weight loss. It was certain that the Fe_3O_4 particles can improve the thermal stability of the composite due to an interaction between Fe_3O_4 and PANI chains which restricts the thermal motion [25]. The content of Fe_3O_4 in the composite was approximately 63.91 and about 33.84 wt% of PANI was coated.

Figure 4 presents magnetic hysteresis loop of Fe_3O_4 and $\text{Fe}_3\text{O}_4@\text{PANI}$ which was measured by a VSM under a magnetic field from -10 to 10 kOe. The values of saturation magnetization, remnant magnetization and coercivity of Fe_3O_4 are 64, 2.6 emu/g and 39.5 Oe, respectively, while those of $\text{Fe}_3\text{O}_4@\text{PANI}$ are 38, 2.2 emu/g and 39.7 Oe, respectively. The decrease in the saturation of magnetization was attributed to the introduction of non-magnetic PANI. Also, a low coercivity value demonstrated their superparamagnetism [20] which is beneficial for the reversible MR systems.

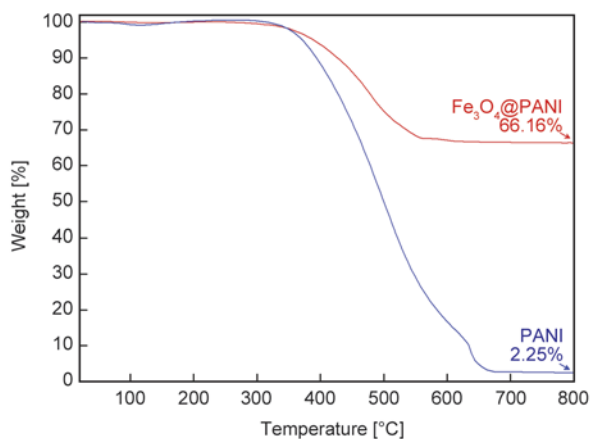


Figure 3. TGA curves of $\text{Fe}_3\text{O}_4@\text{PANI}$ and PANI

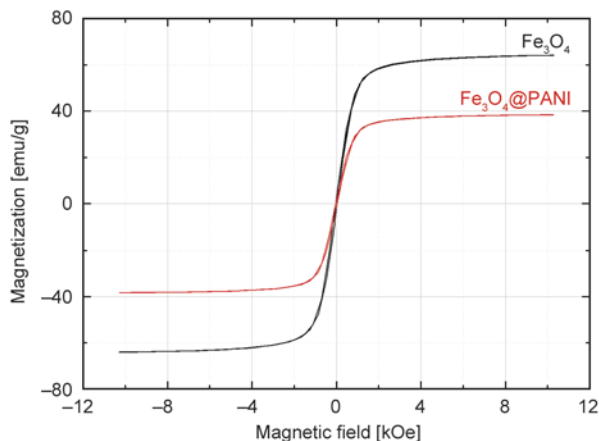
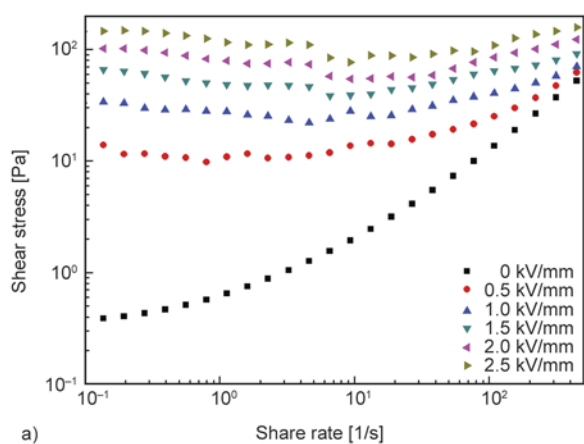


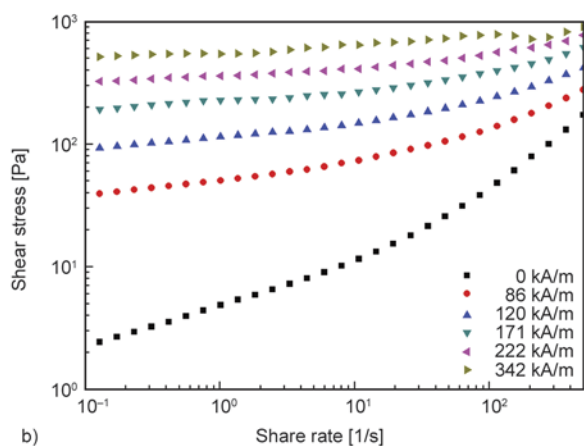
Figure 4. Magnetization curves of Fe_3O_4 and $\text{Fe}_3\text{O}_4@\text{PANI}$

To examine the electric responses of the suspension, the controlled shear rate mode was tested using Couette-type geometry with a rotational rheometer, as shown in Figure 5a. Typically, the suspension behaves like a Newtonian fluid in the absence of an electric field, where the shear stress increases linearly with increasing shear rate [26]. In contrast, under high electric fields, the suspension requires a certain yield stress to initiate shear flow and a shear stress to become stable at the low shear rate region. A large increase in shear stress was caused by the polarized particles and inter-particle interaction force [27]. The yield stresses of the suspension, which was estimated by extrapolating the shear stress to a zero shear rate was enhanced from 13 to 144 Pa with increasing electric field strength from 0.5 to 2.5 kV/mm.

The suspension between the parallel-plate cells was loaded to examine the magnetic responses. The shear stresses were measured as a function of the shear rate ranging from 0.1 to 500 s^{-1} under a magnetic field (Figure 5b). At a zero magnetic field, the suspension behaved like a general fluid, which shows linearity between the shear stress and shear rate. On the other hand, it acted as a Bingham fluid [28] under an external magnetic field with a yield stress due to the formed particle cluster or chains by polarization forces [29]. The yield stresses increased from 30 to 437 Pa under magnetic field strengths from 86 to 342 kA/m. As the polarization force between the particles became stronger, a more rigid chain-like structure can be formed [30]. These improved robust structures can explain why the shear stress is independent of the shear rate and why the yield stress increased with increasing magnetic field strength.

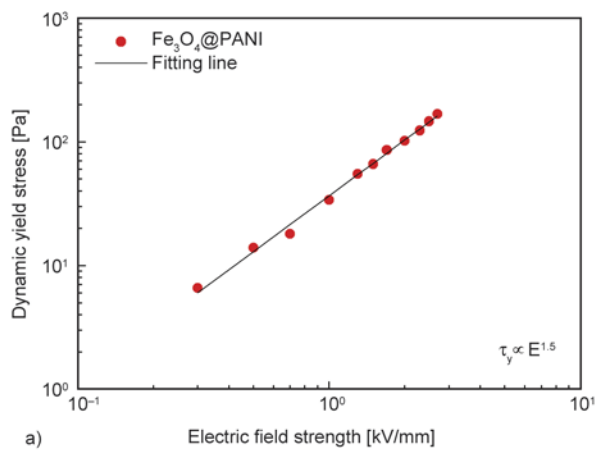


a)

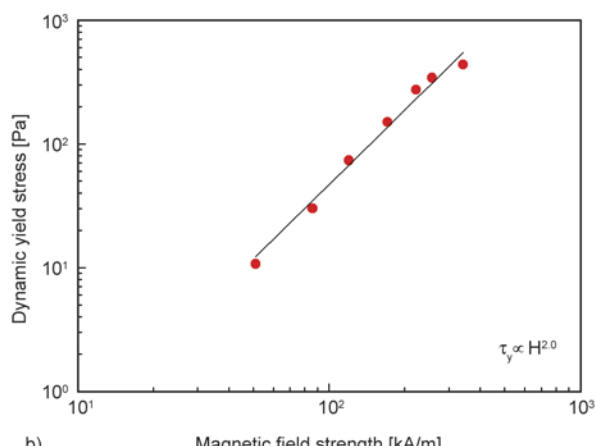


b)

Figure 5. Flow curves of 20 wt% Fe₃O₄@PANI suspension under a) electric and b) magnetic fields



a)



b)

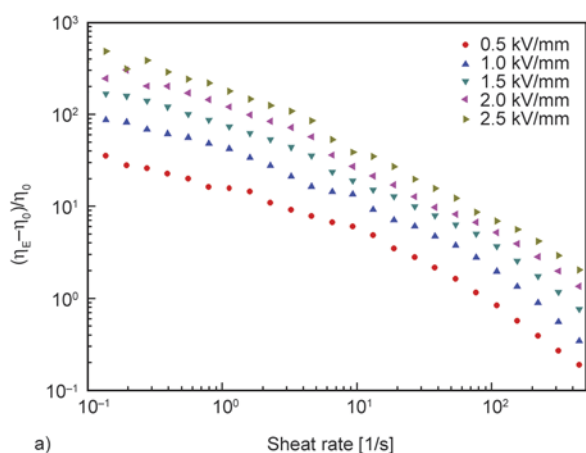
Figure 6. Dynamic yield stress of 20 wt% Fe₃O₄@PANI suspension under a) electric and b) magnetic fields

In particular, the induced magnetostatic force is larger than the hydrodynamic force between particles [31].

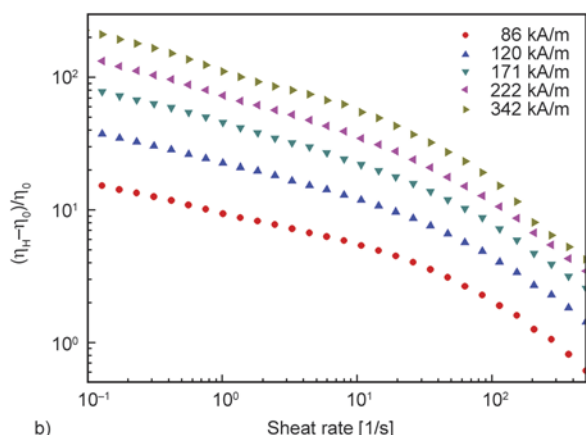
In Figure 6, dynamic yield stresses (τ_y) were reanalyzed as a function of electric and magnetic field strengths from Figure 5 by extrapolating shear stress to zero shear rate. In the presence of external stimuli as electric field (E) and magnetic field (H), the plot showed a power-law relationship of $\tau_y \propto E^\alpha$ [32] and $\tau_y \propto H^\alpha$ [28], respectively. The power-law index α was suggested to be 1.5 in conduction model and 2.0 in polarization model. The dependency of α of Fe₃O₄@PANI suspension was found to 1.5 for ER and 2.0 for MR system.

Some studies have defined an ER efficiency as $(\eta_E - \eta_0)/\eta_0$, where η_E is the viscosity in the presence of electric fields and η_0 is a zero electric field viscosity [13, 33]. In Figure 7, the efficiency increased with increasing electric field from 35 (0.5 kV/mm) to 484 (2.5 kV/mm) at 0.1 s^{-1} . On the other hand, at a high shear rate region, the efficiency decreased due to the destroyed gap-spanning particle chains

resulting in weak resistance to flow [33]. At the low shear rate region, the ER efficiency is significantly higher with increasing electric field due to the high low shear viscosity. Similar to the ER efficiency, the ratio of the shear viscosity with and without a magnetic field can be considered an important factor for evaluating the MR efficiency. The efficiency increased more than 15 fold with increasing magnetic field strength from 15 (51 kA/m) to 227 (342 kA/m) at 0.1 s^{-1} . Consequently, Fe₃O₄@PANI suspension possessed the highest efficiency when 2.5 kV/mm was applied. Compared to other group's results dealing with ER or MR, it has higher ER efficiency than bare titania and GO-wrapped titania microspheres [33], and lower than PANI/TiO₂ nanotubes [34]. Also, it is higher than spherical PANI/VO₂ and lower than flower-like PANI/VO₂ structures [35]. Poly(p-phenylenediamine) particles carbonized under 200°C [36] and PANI-coated carbonized PANI base [37] showed higher ER efficiency value. Nonetheless, the MR efficiency is lower than core-shell urchin-like ZnO coated carbonyl iron microparticles [10].



a) Shear rate [1/s]



b) Shear rate [1/s]

Figure 7. EMR efficiency of 20 wt% Fe₃O₄@PANI suspension under a) electric and b) magnetic fields

The dispersion stability of both Fe₃O₄ and Fe₃O₄@PANI suspension was examined using a Turbiscan, as shown in Figure 8. It measures the degree of light transmission as a function of time along the y-axis sample coordinates. Fe₃O₄@PANI stays steady compared to pure Fe₃O₄ more than five times. The sedimentation test corresponded to the

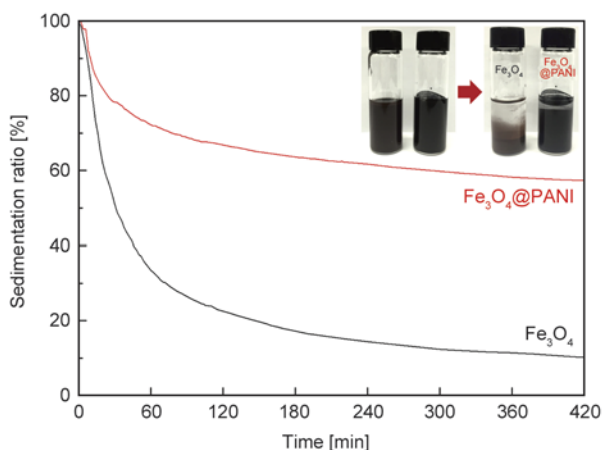


Figure 8. Sedimentation ratio of Fe₃O₄ and Fe₃O₄@PANI suspension (Inset: optical images of samples)

decrease in particle density from 4.46 g/cm³ (Fe₃O₄) to 2.76 g/cm³ (Fe₃O₄@PANI) because the coating of polymer resulted in low density and can improve the dispersion stability.

4. Conclusions

PANI-coated Fe₃O₄ was successfully prepared by solvothermal and oxidation polymerization. The chemical bond formation between Fe₃O₄ and PANI was confirmed by FT-IR spectroscopy, which showed a blue-shift and red-shift of PANI and Fe₃O₄ peaks, respectively. SEM and TEM images confirmed that PANI was attached well to the Fe₃O₄ surface. VSM data showed that magnetization saturation was 38 emu/g for Fe₃O₄@PANI which is lower than that of pure Fe₃O₄ particles. The prepared Fe₃O₄@PANI-based EMR suspension demonstrated typical ER or MR characteristics when electric or magnetic fields were applied, respectively, because of the conducting PANI-shell and magnetic Fe₃O₄-core structure. It is noteworthy that the suspension responded both of electric and magnetic fields and its sedimentation stability was also improved simultaneously.

Acknowledgements

This study was supported by Ministry of Trade, Industry and Energy, Korea through Daeheung RNT (# 10047791).

References

- [1] Yao Z. L., Grishkewich N., Tam K. C.: Swelling and shear viscosity of stimuli-responsive colloidal systems. *Soft Matter*, **9**, 5319–5335 (2013). DOI: [10.1039/C3SM50374G](https://doi.org/10.1039/C3SM50374G)
- [2] Han M. S., Zhang X. Y., Li L., Peng C., Bao L., Ou E. C., Xiong Y. Q., Xu W. J.: Dual-switchable surfaces between hydrophobic and superhydrophobic fabricated by the combination of click chemistry and RAFT. *Express Polymer Letters*, **8**, 528–542 (2014). DOI: [10.3144/expresspolymlett.2014.56](https://doi.org/10.3144/expresspolymlett.2014.56)
- [3] Thakur S., Karak N.: Multi-stimuli responsive smart elastomeric hyperbranched polyurethane/reduced graphene oxide nanocomposites. *Journal of Materials Chemistry A*, **2**, 14867–14875 (2014). DOI: [10.1039/C4TA02497D](https://doi.org/10.1039/C4TA02497D)
- [4] Fameau A-L., Saint-Jalmes A.: Yielding and flow of solutions of thermoresponsive surfactant tubes: Tuning macroscopic rheology by supramolecular assemblies. *Soft Matter*, **10**, 3622–3632 (2014). DOI: [10.1039/C3SM53001A](https://doi.org/10.1039/C3SM53001A)
- [5] Ahn S., Lee S. J.: Nanoparticle role on the repeatability of stimuli-responsive nanocomposites. *Scientific Reports*, **4**, 6624/1–6624/9 (2014). DOI: [10.1038/srep06624](https://doi.org/10.1038/srep06624)

- [6] Zhang W. L., Choi H. J.: Stimuli-responsive polymers and colloids under electric and magnetic fields. *Polymers*, **6**, 2803–2818 (2014). DOI: [10.3390/polym6112803](https://doi.org/10.3390/polym6112803)
- [7] Bica I., Anitas E. M., Bunoiu M., Vatzulik B., Juganaru I.: Hybrid magnetorheological elastomer: Influence of magnetic field and compression pressure on its electrical conductivity. *Journal of Industrial and Engineering Chemistry*, **20**, 3994–3999 (2014). DOI: [10.1016/j.jiec.2013.12.102](https://doi.org/10.1016/j.jiec.2013.12.102)
- [8] Bica I., Liu Y. D., Choi H. J.: Physical characteristics of magnetorheological suspensions and their applications. *Journal of Industrial and Engineering Chemistry*, **19**, 394–406 (2013). DOI: [10.1016/j.jiec.2012.10.008](https://doi.org/10.1016/j.jiec.2012.10.008)
- [9] Zhang X., Li W., Gong X.: Thixotropy of MR shear-thickening fluids. *Smart Materials and Structures*, **19**, 125012/1–125012/6 (2010). DOI: [10.1088/0964-1726/19/12/125012](https://doi.org/10.1088/0964-1726/19/12/125012)
- [10] Machovsky M., Mrlik M., Kuritka I., Pavlinek V., Babayan V.: Novel synthesis of core-shell urchin-like ZnO coated carbonyl iron microparticles and their magnetorheological activity. *RSC Advances*, **4**, 996–1003 (2014). DOI: [10.1039/c3ra44982c](https://doi.org/10.1039/c3ra44982c)
- [11] Marins J. A., Soares B. G., Silva A. A., Hurtado M. G., Livi S.: Electrorheological and dielectric behavior of new ionic liquid/silica systems. *Journal of Colloid and Interface Science*, **405**, 64–70 (2013). DOI: [10.1016/j.jcis.2013.05.013](https://doi.org/10.1016/j.jcis.2013.05.013)
- [12] Mrlik M., Ilcikova M., Sedlacik M., Mosnacek J., Peer P., Filip P.: Cholesteryl-coated carbonyl iron particles with improved anti-corrosion stability and their viscoelastic behaviour under magnetic field. *Colloid and Polymer Science*, **292**, 2137–2143 (2014). DOI: [10.1007/s00396-014-3245-5](https://doi.org/10.1007/s00396-014-3245-5)
- [13] Lengálová A., Pavlínek V., Sába P., Quadrat O., Kitano T., Stejskal J.: Influence of particle concentration on the electrorheological efficiency of polyaniline suspensions. *European Polymer Journal*, **39**, 641–645 (2003). DOI: [10.1016/S0014-3057\(02\)00281-1](https://doi.org/10.1016/S0014-3057(02)00281-1)
- [14] Wang B., Yin Y., Liu C., Yu S., Chen K.: Synthesis of flower-like BaTiO₃/Fe₃O₄ hierarchically structured particles and their electrorheological and magnetic properties. *Dalton Transactions*, **42**, 10042–10055 (2013). DOI: [10.1039/c3dt50504a](https://doi.org/10.1039/c3dt50504a)
- [15] Jang W. H., Kim J. W., Choi H. J., Jhon M. S.: Synthesis and electrorheology of camphorsulfonic acid doped polyaniline suspensions. *Colloid and Polymer Science*, **279**, 823–827 (2001). DOI: [10.1007/s003960100534](https://doi.org/10.1007/s003960100534)
- [16] Fang F. F., Liu Y. D., Choi H. J.: Electrorheological and magnetorheological response of polypyrrole/magnetite nanocomposite particles. *Colloid and Polymer Science*, **291**, 1781–1786 (2013). DOI: [10.1007/s00396-013-2913-1](https://doi.org/10.1007/s00396-013-2913-1)
- [17] Bednarek S.: Electromagnetorheological suspensions and induced changes of their magnetic permeability and dielectric constant. *Review of Scientific Instruments*, **70**, 1505–1510 (1999). DOI: [10.1063/1.1149614](https://doi.org/10.1063/1.1149614)
- [18] Minagawa K., Watanabe T., Koyama K., Sasaki M.: Significant synergistic effect of superimposed electric and magnetic fields on the rheology of iron suspension. *Langmuir*, **10**, 3926–3928 (1994). DOI: [10.1021/la00023a003](https://doi.org/10.1021/la00023a003)
- [19] Korobko E. V., Novikova Z. A., Zhurauski M. A., Borin D., Odenbach S.: Synergistic effect in magnetoelectrorheological fluids with a complex dispersed phase. *Journal of Intelligent Material Systems and Structures*, **23**, 963–967 (2012). DOI: [10.1177/1045389X11429174](https://doi.org/10.1177/1045389X11429174)
- [20] Han X., Gai L., Jiang H., Zhao L., Liu H., Zhang W.: Core-shell structured Fe₃O₄/PANI microspheres and their Cr(VI) ion removal properties. *Synthetic Metals*, **171**, 1–6 (2013). DOI: [10.1016/j.synthmet.2013.02.025](https://doi.org/10.1016/j.synthmet.2013.02.025)
- [21] Zheng W., Angelopoulos M., Epstein A. J., MacDiarmid A. G.: Experimental evidence for hydrogen bonding in polyaniline: Mechanism of aggregate formation and dependency on oxidation state. *Macromolecules*, **30**, 2953–2955 (1997). DOI: [10.1021/ma9700136](https://doi.org/10.1021/ma9700136)
- [22] Liu W., Kumar J., Tripathy S., Samuelson L. A.: Enzymatic synthesis of conducting polyaniline in micelle solutions. *Langmuir*, **18**, 9696–9704 (2002). DOI: [10.1021/la0206357](https://doi.org/10.1021/la0206357)
- [23] Zheng Y-H., Cheng Y., Bao F., Wang Y-S.: Synthesis and magnetic properties of Fe₃O₄ nanoparticles. *Materials Research Bulletin*, **41**, 525–529 (2006). DOI: [10.1016/j.materresbull.2005.09.015](https://doi.org/10.1016/j.materresbull.2005.09.015)
- [24] Gai L., Du G., Zuo Z., Wang Y., Liu D., Liu H.: Controlled synthesis of hydrogen titanate–polyaniline composite nanowires and their resistance–temperature characteristics. *The Journal of Physical Chemistry C*, **113**, 7610–7615 (2009). DOI: [10.1021/jp900369y](https://doi.org/10.1021/jp900369y)
- [25] Deng J., He C., Peng Y., Wang J., Long X., Li P., Chan A. S. C.: Magnetic and conductive Fe₃O₄–polyaniline nanoparticles with core–shell structure. *Synthetic Metals*, **139**, 295–301 (2003). DOI: [10.1016/S0379-6779\(03\)00166-8](https://doi.org/10.1016/S0379-6779(03)00166-8)
- [26] Cho M. S., Cho Y. H., Choi H. J., Jhon M. S.: Synthesis and electrorheological characteristics of polyaniline-coated poly(methyl methacrylate) microsphere: Size effect. *Langmuir*, **19**, 5875–5881 (2003). DOI: [10.1021/la026969d](https://doi.org/10.1021/la026969d)
- [27] Stěnička M., Pavlínek V., Sába P., Blinova N. V., Stejskal J., Quadrat O.: The electrorheological efficiency of polyaniline particles with various conductivities suspended in silicone oil. *Colloid and Polymer Science*, **287**, 403–412 (2009). DOI: [10.1007/s00396-008-1977-9](https://doi.org/10.1007/s00396-008-1977-9)

- [28] Bossis G., Lacis S., Meunier A., Volkova O.: Magnetorheological fluids. *Journal of Magnetism and Magnetic Materials*, **252**, 224–228 (2002).
DOI: [10.1016/S0304-8853\(02\)00680-7](https://doi.org/10.1016/S0304-8853(02)00680-7)
- [29] Jang I. B., Kim H. B., Lee J. Y., You J. L., Choi H. J., Jhon M. S.: Role of organic coating on carbonyl iron suspended particles in magnetorheological fluids. *Journal of Applied Physics*, **97**, 10Q912/1–10Q912/3 (2005).
DOI: [10.1063/1.1853835](https://doi.org/10.1063/1.1853835)
- [30] Orihara H., Nishimoto Y., Aida K., Na Y. H., Nagaya T., Ujiie S.: Morphology and rheology of an immiscible polymer blend subjected to a step electric field under shear flow. *Journal of Physics: Condensed Matter*, **23**, 284106/1–284106/6 (2011).
DOI: [10.1088/0953-8984/23/28/284106](https://doi.org/10.1088/0953-8984/23/28/284106)
- [31] Park B. J., Hong M. K., Choi H. J.: Atom transfer radical polymerized PMMA/magnetite nanocomposites and their magnetorheology. *Colloid and Polymer Science*, **287**, 501–504 (2009).
DOI: [10.1007/s00396-009-2013-4](https://doi.org/10.1007/s00396-009-2013-4)
- [32] Klingenberg D. J., van Swol F., Zukoski C. F.: The small shear rate response of electrorheological suspensions. II. Extension beyond the point–dipole limit. *The Journal of Chemical Physics*, **94**, 6170–6178 (1991).
DOI: [10.1063/1.460403](https://doi.org/10.1063/1.460403)
- [33] Yin J., Shiu Y., Dong Y., Zhao X.: Enhanced dielectric polarization and electro-responsive characteristic of graphene oxide-wrapped titania microspheres. *Nanotechnology*, **25**, 045702/1–045702/11 (2014).
DOI: [10.1088/0957-4484/25/4/045702](https://doi.org/10.1088/0957-4484/25/4/045702)
- [34] Cheng Q., Pavlinek V., He Y., Li C., Saha P.: Electrorheological characteristics of polyaniline/titanate composite nanotube suspensions. *Colloid and Polymer Science*, **287**, 435–441 (2009).
DOI: [10.1007/s00396-008-1985-9](https://doi.org/10.1007/s00396-008-1985-9)
- [35] Goswami S., Brehm T., Filonovich S., Cidade M. T.: Electrorheological properties of polyaniline–vanadium oxide nanostructures suspended in silicone oil. *Smart Materials and Structures*, **23**, 105012/1–105012/10 (2014).
DOI: [10.1088/0964-1726/23/10/105012](https://doi.org/10.1088/0964-1726/23/10/105012)
- [36] Plachy T., Sedlacik M., Pavlinek V., Morávková Z., Hajná M., Stejskal J.: An effect of carbonization on the electrorheology of poly(*p*-phenylenediamine). *Carbon*, **63**, 187–195 (2013).
DOI: [10.1016/j.carbon.2013.06.070](https://doi.org/10.1016/j.carbon.2013.06.070)
- [37] Sedlacik M., Pavlinek V., Mrlik M., Morávková Z., Hajná M., Trchová M., Stejskal J.: Electrorheology of polyaniline, carbonized polyaniline, and their core–shell composites. *Materials Letters*, **101**, 90–92 (2013).
DOI: [10.1016/j.matlet.2013.03.084](https://doi.org/10.1016/j.matlet.2013.03.084)

Amino acid-incorporated polymer network by thiol-ene polymerization

R. Yokose, T. Shimasaki, N. Teramoto, M. Shibata*

Department of Life and Environmental Sciences, Faculty of Engineering, Chiba Institute of Technology, 2-17-1, Tsudanuma, Narashino, 275-0016 Chiba, Japan

Received 22 January 2015; accepted in revised form 9 March 2015

Abstract. Triallyl L-alanine (A3A) and triallyl L-phenylalanine (A3F) were synthesized by reactions of L-alanine and L-phenylalanine with allyl bromide in the presence of sodium hydroxide, respectively. Thiol-ene thermal polymerization of A3A or A3F with pentaerythritol-based primary tetrathiol (pS4P) or pentaerythritol-based secondary tetrathiol (S4P) at allyl/SH 1/1 in the presence of 2,2'-azobis(isobutyronitrile) produced an amino acid-incorporated polymer network (A3A-pS4P, A3A-S4P or A3F-S4P). Although the thermally cured resins were homogeneous and flat films, the corresponding thiol-ene photopolymerization did not give a successful result. Degree of swelling for each thermally cured film in *N,N*-dimethylformamide was much higher than that in water. The glass transition and 5% weight loss temperatures (T_g and T_5) of A3F-pS4P and A3F-S4P were higher than those of A3A-pS4P and A3A-S4P, respectively. Also, A3F-pS4P and A3F-S4P exhibited much higher tensile strengths and moduli than A3A-pS4P and A3A-S4P did, respectively. Consequently, A3F-pS4P displayed the highest T_g (38.7°C), T_5 (282.0°C), tensile strength (9.5 MPa) and modulus (406 MPa) among all the thermally cured resins.

Keywords: thermosetting resins, biopolymers, alanine, phenylalanine, thiol-ene polymerization

t1. Introduction

Naturally occurring α -amino acid based polymers have gathered considerable attention over recent years as biodegradable, biocompatible and functional materials having various characteristics such as amphoteric nature [1, 2], chiral recognition [3], drug delivery [4, 5], response to stimuli [6–12] and self-organization via supramolecular interactions [13–15]. In past studies, amino acid-based side chain polymers had been mainly synthesized by conventional or controlled free radical polymerizations of amino acids whose *N*- or *C*-terminals are modified with (meth)acrylamide [1–4, 10–12, 14, 16–22] or (meth)acrylate groups [6–9, 23–27]. Amino acid-based main chain polymers had been prepared by ring-opening polymerizations of α -

amino acid *N*-carboxyanhydrides [15, 28–30] or polycondensations of amino acids [31, 32]. Although these strategies had been successfully applied to the synthesis of linear polymers having amino acid moieties, the polymer networks having amino acid moieties in the main chain have not yet been synthesized by the addition polymerizations of amino acids whose *N*- and *C*-terminals are simultaneously modified with substituted olefinic groups. There have been few reports on the synthesis of amino acid-based polymer networks by use of polyaddition reactions. For example, Kiyotsukuri *et al.* [33] reported a polymer network by the reaction of lysine triisocyanate and glutamic acid diethylester hydrochloride. Li *et al.* [34] reported a polymer network by the reaction of a cycloaliphatic epoxy resin with

*Corresponding author, e-mail: mitsuhiro.shibata@p.chibakoudai.jp
© BME-PT

DL-lysine, or diglycidyl ether of bisphenol A with L-tryptophan [35]. We also reported a polymer network by the reaction of 4,4'-bismaleimidodiphenylmethane with L-lysine [36].

Recently, radical-mediated thiol-ene 'click' reactions have attracted increasing attention as a method for the production of crosslinked polymer networks with various frameworks and functional groups [37–40]. The radical thiol-ene reaction can be initiated by a variety of techniques including under traditional thermal conditions with common azo species such as 2,2'-azobis(isobutyronitrile) (AIBN) or via photochemical methods, with or without added photoinitiator. Thiol-ene polymerization is characterized by advantages such as an inherently rapid reaction rate, reduced oxygen inhibition, high regioselectivity and low polymerization shrinkage. Furthermore, as the reaction is initiated by the formation of primary radicals by the decomposition of an initiator and subsequent production of a thiyl radical by the abstraction of a hydrogen radical from the thiol group, monomers containing functional groups (OH, CO₂H, NH₂ etc.) with a hydrogen that is less easily abstracted than the hydrogen of a thiol group can be polymerized without protecting the functional groups. In past studies, several research groups reported on the syntheses of bio-based polymer networks by thiol-ene polymerizations. For example, Echeverri *et al.* [41] reported elastomeric networks from maleated soybean-oil glycerides by thiol-ene coupling. Ortiz *et al.* [42] reported polymer networks prepared by thiol-ene photopolymerizations of allyl-etherified sucroses. We also reported trehalose- and eugenol-incorporated polymer networks by thiol-ene photopolymerizations [43, 44]. In the past studies, thiol-ene reactions have been applied to the modification of unsaturated amino acids [45] and to the synthesis of peptide-functionalized conjugates [46], but amino acid-based polymer network has not been prepared by use of thiol-ene polymerization to the best of our knowledge. In this study, triallyl L-alanine (A3A) and triallyl L-phenylalanine (A3F) whose *N*- and *C*-terminals are simultaneously modified with allyl groups were conveniently synthesized by one-pot reactions of L-alanine and L-phenylalanine with allyl bromide, respectively (Figure 1), and thermal and mechanical properties of polymer networks prepared by thiol-ene reactions of A3A and A3F with tetrathiol compounds were investigated.

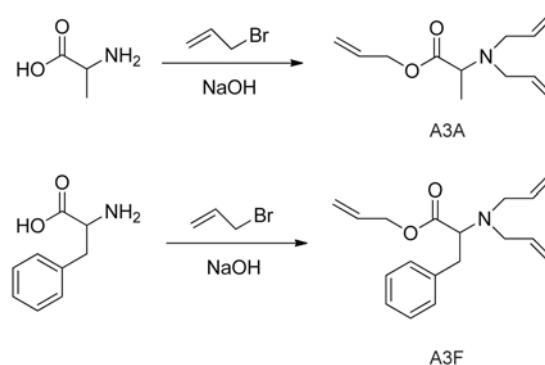


Figure 1. Synthesis of A3A and A3F

2. Experimental section

2.1. Materials

L-Alanine and L-phenylalanine were purchased from Tokyo Kasei Kogyo Co. Ltd. (Tokyo, Japan). Pentaerythritol-based primary tetrathiol (pS4P, pentaerythritol tetrakis(3-mercaptopropionate)) was purchased from Sigma-Aldrich Corporation (St. Louis, MO, USA). Pentaerythritol-based secondary tetrathiol (S4P, pentaerythritol tetrakis(3-mercaptopbutyrate), trade name: Karenz MT™ PE1) was kindly provided by Showa Denko K. K. (Tokyo, Japan). The chemical structures of pS4P and S4P are shown in Figure 2. As photo-initiators, 1-hydroxycyclohexyl phenyl ketone (Irgacure® 184, mp. 45–49°C, UV/VIS absorption peaks in methanol: 246, 280, 333 nm), phenyl bis(2,4,6-trimethylbenzoyl) phosphine oxide (Irgacure® 819, mp. 127–133°C, UV/VIS absorption peaks in methanol: 295, 370 nm), 2-hydroxy-1-[4-(2-hydroxyethoxy)phenyl]-2-methyl-1-propanone (Irgacure® 2959, mp. 86.5–89.5°C, UV/VIS absorption peak in methanol: 276 nm) were purchased from Toyotsu Chemiplas Corporation (Tokyo, Japan). (±)-Camphorquinone (Wako Pure Chemical Industries Ltd., Osaka, Japan) was also used as a photo-initiator. Allyl bromide, sodium hydroxide, AIBN, dimethyl sulfoxide (DMSO), *N,N*-dimethylformamide (DMF) and acetone were purchased from Kanto Chemical Co., Inc. (Tokyo,

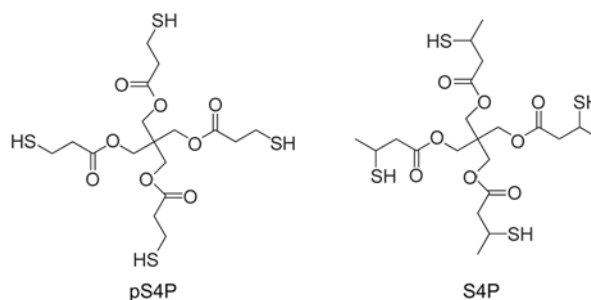


Figure 2. Chemical structures of pS4P and S4P

Japan). All of the commercially available reagents were used without further purification.

2.2. Synthesis of *N,N,O*-triallyl-L-alanine (A3A)

To a solution of L-alanine (0.891 g, 10.0 mmol) in DMSO (30 mL), pulverized sodium hydroxide (2.64 g, 66.0 mol) was added, and the resulting mixture was stirred for 10 min. Allyl bromide (3.99 g, 33.0 mol) was dropwise added over a period of 30 min at room temperature. After the addition, the mixture was stirred for 24 h at room temperature and filtered. Dilute hydrochloric acid was added to the filtrate, and then extracted with chloroform. The organic layer was washed with water five times, dried over sodium sulfate and concentrated in vacuo to produce A3A as a brown liquid (1.08 g) in 52% yield: $^{13}\text{C-NMR}$ (400 MHz, CDCl_3 , δ , ppm): 14.94 (C-9), 53.63 (C-4), 57.38 (C-7), 64.76 (C-1), 116.87 (C-6), 118.24 (C-3), 132.17 (C-2), 136.41 (C-5), 173.52 (C-8). Anal. calcd. for $\text{C}_{12}\text{H}_{19}\text{O}_2\text{N}$: C, 68.87%; H, 9.15%; N, 6.69%. Found: C, 68.5%; H, 9.22%; N, 6.30%.

2.3. Synthesis of

N,N,O-triallyl-L-phenylalanine (A3F)

To a solution of L-phenylalanine (1.65 g, 10.0 mmol) in DMSO (30 mL), pulverized sodium hydroxide (2.64 g, 66.0 mol) was added, and the resulting mixture was stirred for 10 min. Allyl bromide (3.99 g, 33.0 mol) was dropwise added over a period of 30 min at room temperature. After the addition, the mixture was stirred for 24 h at room temperature and filtered. Dilute hydrochloric acid was added to the filtrate, and then extracted with ethyl acetate. The organic layer was washed with water three times, dried over sodium sulfate and concentrated in vacuo to produce A3F as a brown liquid (2.62 g) in 92% yield. $^{13}\text{C-NMR}$ (400 MHz, CDCl_3 , δ , ppm): 35.96 (C-9), 53.54 (C-4), 64.05 (C-7), 64.95 (C-1), 117.07 (C-6), 118.22 (C-3), 126.45 (C-13), 128.05 (C-12), 129.32 (C-11), 132.10 (C-2), 136.19 (C-5), 138.83 (C-10), 172.16 (C-8). Anal. calcd. for $\text{C}_{18}\text{H}_{23}\text{O}_2\text{N}$: C, 75.76%; H, 8.12%; N, 4.91%. Found: C, 75.4%; H, 8.09%; N, 4.91%.

2.4. Thiol-ene photopolymerization of A3A and pS4P

A mixture of A3A (0.209 g, 1.00 mmol), pS4P (0.366 g, 0.750 mmol), IRGACURE[®] 2959 (17 mg, 0.076 mmol) and acetone (2 mL) was stirred for

30 min to form a homogeneous solution. The solution was poured on a glass culture dish with a diameter of 40 mm and was dried at 60°C for 3 h. The obtained mixture was photo-irradiated for 30 s \times 60 times at 1 min intervals to yield a photo-cured A3A/pS4P with the allyl/SH ratio of 1/1 (pc-A3A-pS4P) film with wrinkles. A SPOT-CURE SP-7 (250 W light source, wavelength 240–440 nm, Ushio Inc., Yokohama, Japan) device equipped with a uniform-radiation optical unit was used for UV curing (irradiation distance 200 mm, irradiation intensity 72 mW/cm²).

2.5. Thiol-ene thermal polymerizations

A typical procedure is as follows: A mixture of A3A (2.233 g, 10.67 mmol), pS4P (3.909 g, 8.00 mmol), AIBN (57 mg, 0.35 mmol) and acetone (5 mL) was stirred for 30 min to form a homogeneous solution. The solution was poured on a poly(methylpentene) culture dish with a diameter of 85 mm and was dried at room temperature for 3 h. The obtained mixture was cured at 80°C for 24 h and furthermore at 120°C for 48 h to yield a thermally cured A3A/pS4P with the allyl/SH ratio of 1/1 (A3A-pS4P) film (thickness: ca. 1.0 mm).

In a manner similar to the preparation of A3A-pS4P except using A3F (2.282 g, 8.00 mmol), pS4P (3.269 g, 6.00 mmol), AIBN (56 mg, 0.34 mmol) and acetone (4 mL), a thermally cured A3F/pS4P with the allyl/SH ratio of 1/1 (A3F-pS4P) film (thickness: ca. 1.0 mm) were prepared. Thermally cured A3A/S4P and A3F/S4P with the allyl/SH ratio of 1/1 (A3A-S4P and A3F-S4P) were similarly prepared by using S4P instead of pS4P.

2.6. Measurements

Proton and carbon nuclear magnetic resonance (^1H - and $^{13}\text{C-NMR}$) spectra were recorded on a Bruker AV-400 (400 MHz) (Madison, WI, USA) using CDCl_3 as a solvent. Fourier transform infrared (FTIR) spectra were recorded on a Shimadzu FT-IR 8100 (Kyoto, Japan) by the attenuated total reflectance (ATR) method. Elemental analyses were performed on a SUMIGRAPH NCH-22F elemental microanalyzer (Sumika Chemical Analysis Service, Ltd., Ehime, Japan). Degree of swelling (D_s) was measured by dipping a thermally cured film (length 10 mm, width 10 mm, thickness 1.0 mm) in deionized water, acetone or DMF at room temperature for 48 h according to Equation (1):

$$D_s [\%] = 100 \frac{w_1 - w_0}{w_0} \quad (1)$$

where w_0 is the initial weight of the cured film and w_1 is the weight of the swollen film after dipping. The differential scanning calorimetry (DSC) measurements were performed on a Perkin-Elmer Diamond DSC (Waltham, MA, USA) in a nitrogen atmosphere. The samples were heated from -100 to 200°C at a heating rate of $20^\circ\text{C}\cdot\text{min}^{-1}$ to determine the glass transition temperature (T_g). The 5% weight loss temperature (T_5) was measured on a Shimadzu TGA-50 thermogravimetric analyzer at a heating rate of $20^\circ\text{C}\cdot\text{min}^{-1}$ in a nitrogen atmosphere. Tensile testing of the rectangular plates (length 50 mm,

width 10 mm, thickness 1.0 mm) was performed at room temperature using a Shimadzu Autograph AG-1 based on the standard method for testing the tensile properties of plastics (JIS K7161:1994, ISO527-1). The span length was 25 mm, and the testing speed was $10\text{ mm}\cdot\text{min}^{-1}$. Five specimens were tested for each set of samples, and the mean value and standard deviation were calculated.

3. Results and discussion

3.1. Synthesis and characterization of A3A and A3F

Triallylated amino acids, A3A and A3F whose all *N*- and *C*-terminal active hydrogens are substituted by allyl groups were conveniently synthesized by

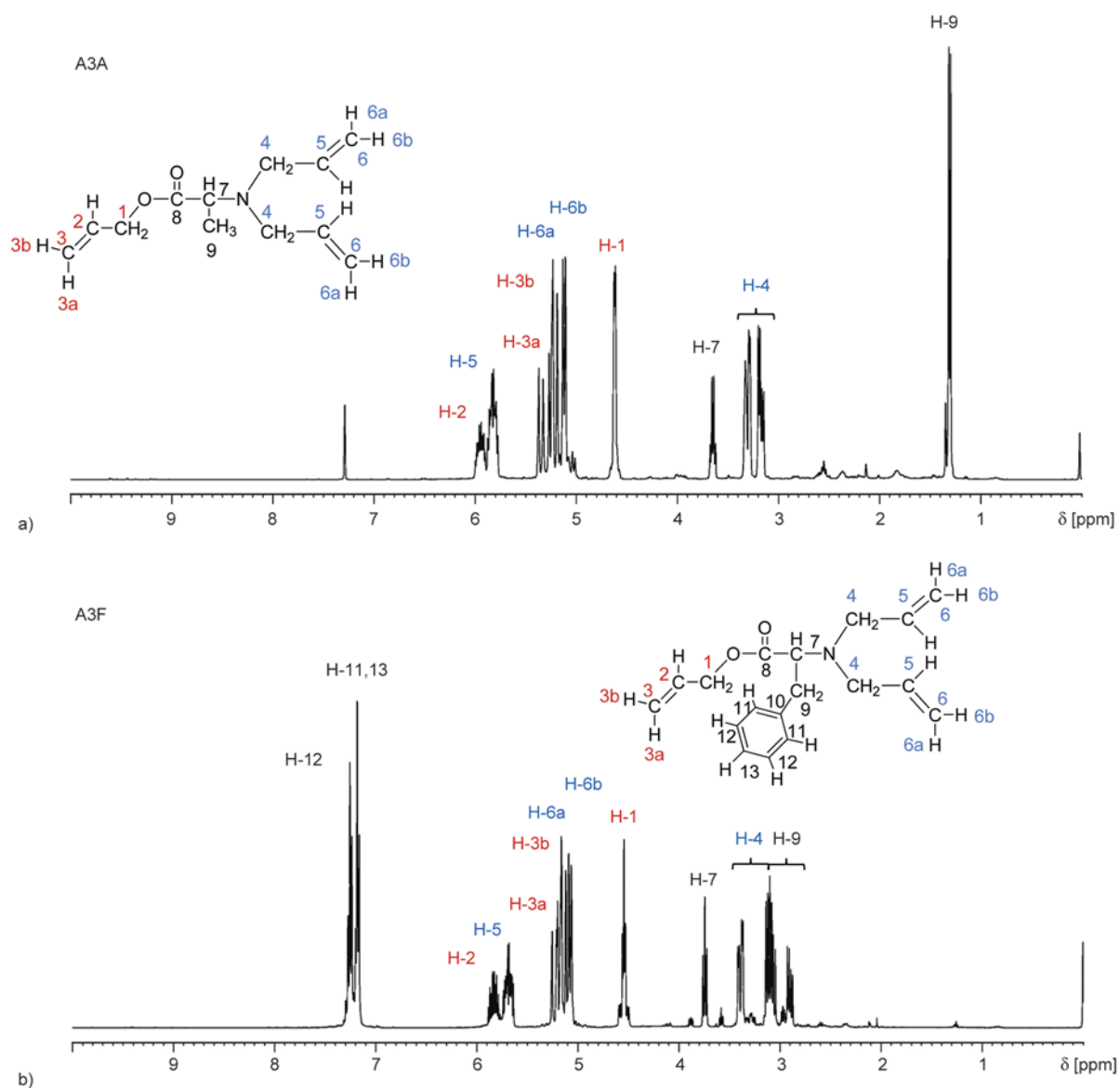


Figure 3. $^1\text{H-NMR}$ spectra of (a) A3A and (b) A3F in CDCl_3 . The ^1H -signals displayed in red and blue are related *O*-allyl and *N*-allyl groups, respectively.

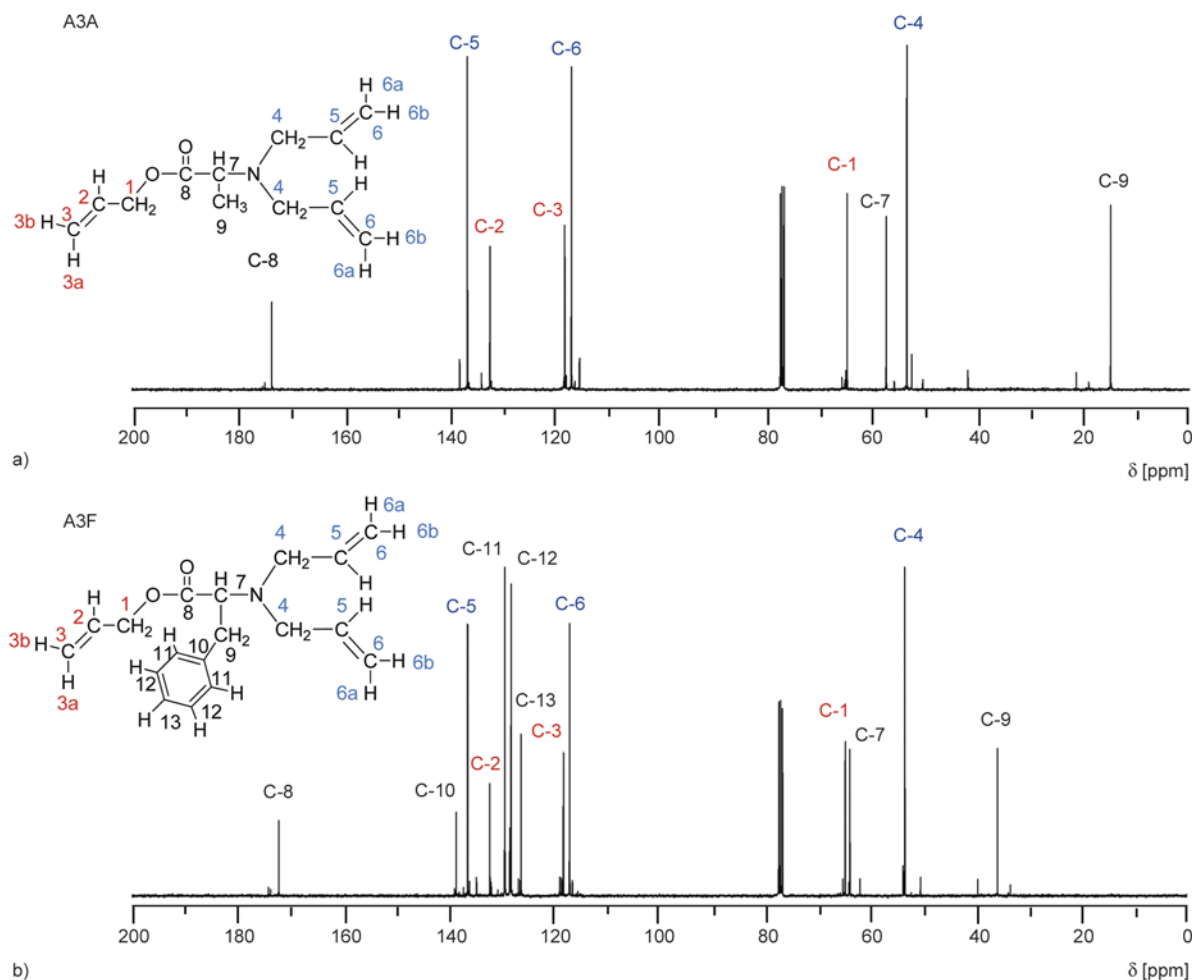


Figure 4. ^{13}C -NMR spectra of (a) A3A and (b) A3F in CDCl_3 . The ^1H -signals displayed in red and blue are related *O*-allyl and *N*-allyl groups, respectively.

reactions of L-alanine and L-phenylalanine with allyl bromide in the presence of excess pulverized sodium hydroxide in DMSO, respectively (Figure 1). Figure 3a shows ^1H -NMR spectrum of A3A in CDCl_3 . The methyl and methine ^1H signals of alanine residue of A3A were observed at δ 3.65 (m, 1H, H-7) and 1.30 ppm (d, 3H, H-9), respectively. The ^1H signals of *N,N*-diallyl groups were observed at δ 5.81 (m, 2H, H-5), 5.21 (m, 2H, H-6a), 5.11 (m, 2H, H-6b) and 3.30, 3.19 ppm (m, 4H, H-4), respectively. The proton signals of *O*-allyl group were observed at δ 5.95 (m, 1H, H-2), 5.35 (m, 1H, H-3a), 5.27 (m, 1H, H-3b) and 4.60 ppm (m, 2H, H-1). Figure 3b shows ^1H -NMR spectrum of A3F in CDCl_3 . The phenyl, methine and benzyl methylene ^1H signals of phenylalanine residue of A3F were observed at δ 7.26 (m, 2H, H-12), 7.18 (m, 3H, H-11,13), 3.75 (m, 1H, H-7) and 3.09, 2.90 ppm (m, 2H, H-9), respectively. The ^1H signals of *N,N*-diallyl groups were observed at δ 5.69 (m, 2H, H-5),

5.16 (m, 2H, H-6a), 5.06 (m, 2H, H-6b) and 3.39, 3.11 ppm (m, 4H, H-4), respectively. The proton signals of *O*-allyl group were observed at δ 5.82 (m, 1H, H-2), 5.26 (m, 1H, H-3a), 5.20 (m, 1H, H-3b) and 4.52 ppm (m, 2H, H-1). The fact that *N*- CH_2 protons (H-4 of A3A or A3F) were observed as complex signals indicates that the two methylene protons are magnetically non-equivalent probably due to steric hindrance around the *N*-methylene groups. Figure 4 shows ^{13}C -NMR spectra of A3A and A3F in CDCl_3 . As are shown in the figure, all the carbons of A3A and A3F were reasonably assigned. The assignment of ^1H and ^{13}C -signals of A3A and A3F shown in Figure 3 and Figure 4 was confirmed by H–H correlated spectroscopy (COSY), C–H COSY and the heteronuclear multiple bond correlation (HMBC) spectroscopy.

It is important for checking the progress of thiol-ene reaction of A3A and A3F to assign the IR absorption bands related to the allyl groups. Figure 5 shows

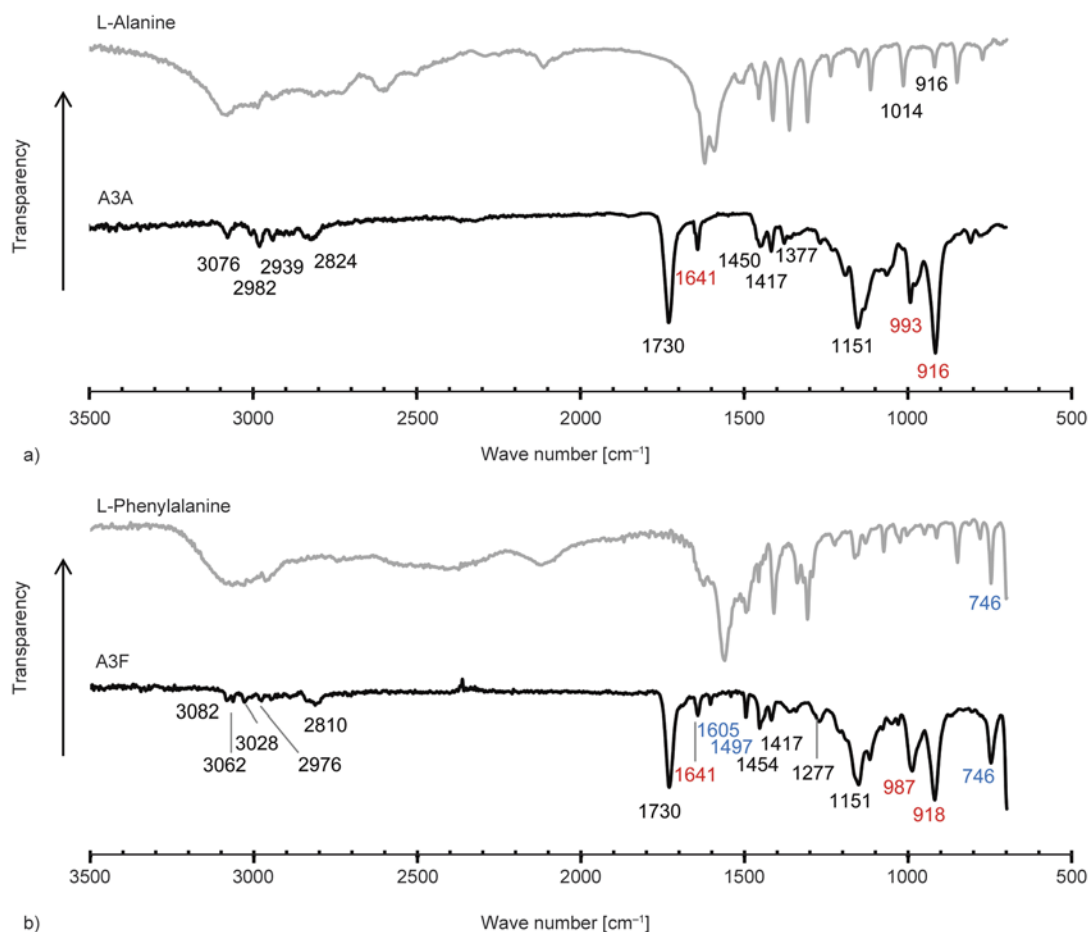


Figure 5. FT-IR spectra of (a) L-alanine and A3A and (b) L-phenylalanine and A3F. The wavenumbers displayed in red and blue are related to allyl and phenyl groups, respectively.

FT-IR spectra of A3A and A3F compared with those of L-alanine and L-phenylalanine. In the FT-IR spectrum of A3F, the bands characteristic to benzene ring were observed at 1605, 1497 and 746 cm⁻¹, which are ascribed to aromatic C=C stretching vibration and aromatic =C–H out-of-plane bending vibration, respectively. As the bands which are common in the spectra of A3A and A3F, the bands due to olefinic and/or aromatic C–H stretching vibrations and aliphatic C–H stretching vibration were observed at 3082–3028 cm⁻¹ and 2982–2810 cm⁻¹, respectively. Also, the bands due to C=O and C–O (C–N) stretching vibrations were observed at 1730 and 1151 cm⁻¹, respectively. Furthermore, the bands ascribed to allyl C=C stretching ($\nu_{C=C}$) and =C–H out-of-plane bending (δ_{C-H}) vibrations were observed at 1641 cm⁻¹ and 993 (987), 916 (918) cm⁻¹, respectively. These bands characteristic to allyl group were used for the confirmation of progress of thiol-ene reaction of A3A and A3F with

the proviso that a weak absorption band is also observed at 916 cm⁻¹ for L-alanine.

3.2. FT-IR analysis for the thiol-ene polymerization of A3A and A3F

Thiol-ene photopolymerization of A3A and pS4P at the allyl/thiol ratio of 1/1 in the presence of a photoinitiator (Irgacure[®] 184) produced a crosslinked yellow film (pc-A3A-pS4P) with many wrinkles, as is obvious from Figure 6. Although other photoinitiators (Irgacure[®] 819, Irgacure[®] 2959 and camphorquinone) were examined, we could not get a flat film. Furthermore, photo-irradiation of a mixture of A3F/pS4P in the presence of a photoinitiator produced a viscous liquid whose surface portion only is hardened. There is a possibility that the sterically hindered diallylamino groups of A3A and A3F have a lower reactivity than the allyl ester group at room temperature. Next, thiol-ene thermal polymerizations were examined. When A3A and A3F were

thermally cured with pS4P in the presence of AIBN at 80–120°C, flat and flexible films (A3A-pS4P and

A3F-pS4P) with a brown color were obtained (Figure 6). Also, we could get similar flat films by the thiol-ene thermal polymerizations of A3A and A3F with S4P. Also, we confirmed that A3A or A3F by itself cannot be thermally cured in the presence of AIBN at the same curing condition.

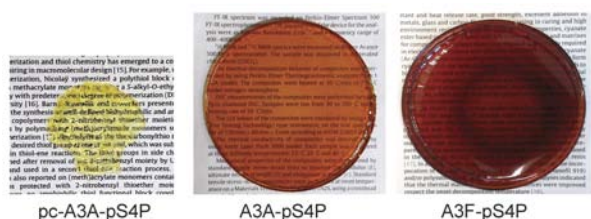


Figure 6. Photographs of pc-A3A-pS4P, A3A-pS4P and A3F-pS4P films

Figure 7 shows FT-IR spectra of pc-A3A-pS4P, A3A-pS4P and A3A-S4P compared with those of A3A, pS4P and S4P. The absorption bands related to allyl $\nu_{C=C}$ (1641 cm^{-1}) and δ_{C-H} ($993, 916\text{ cm}^{-1}$) vibrations were non-existent for pc-A3A-pS4P,

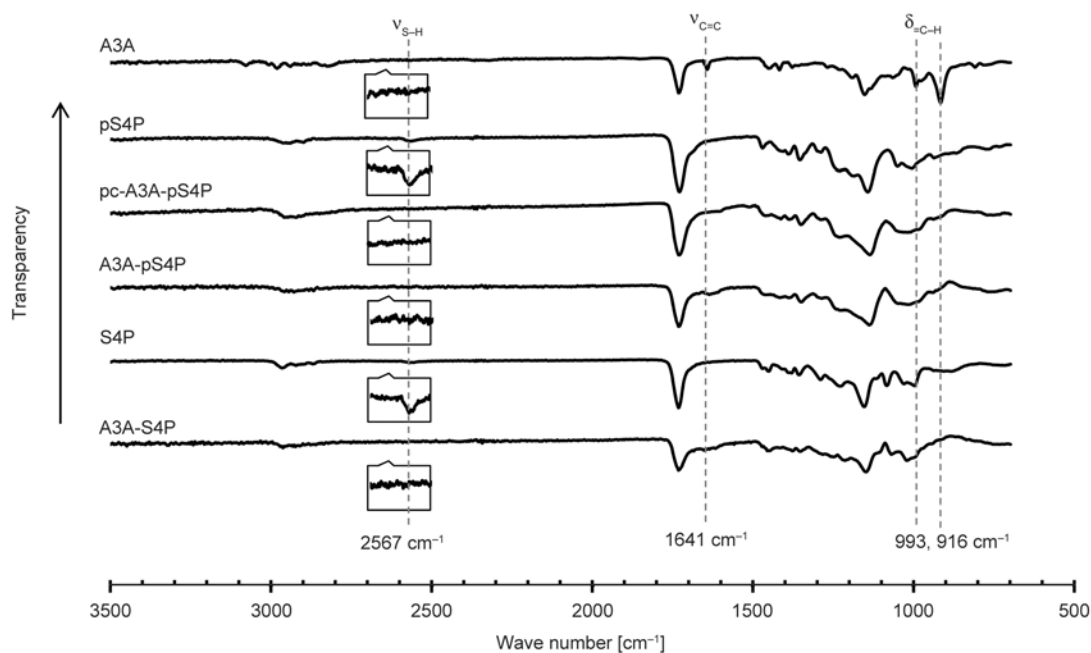


Figure 7. FT-IR spectra of pc-A3A-pS4P, A3A-pS4P and A3A-S4P compared with those of A3A, pS4P and S4P

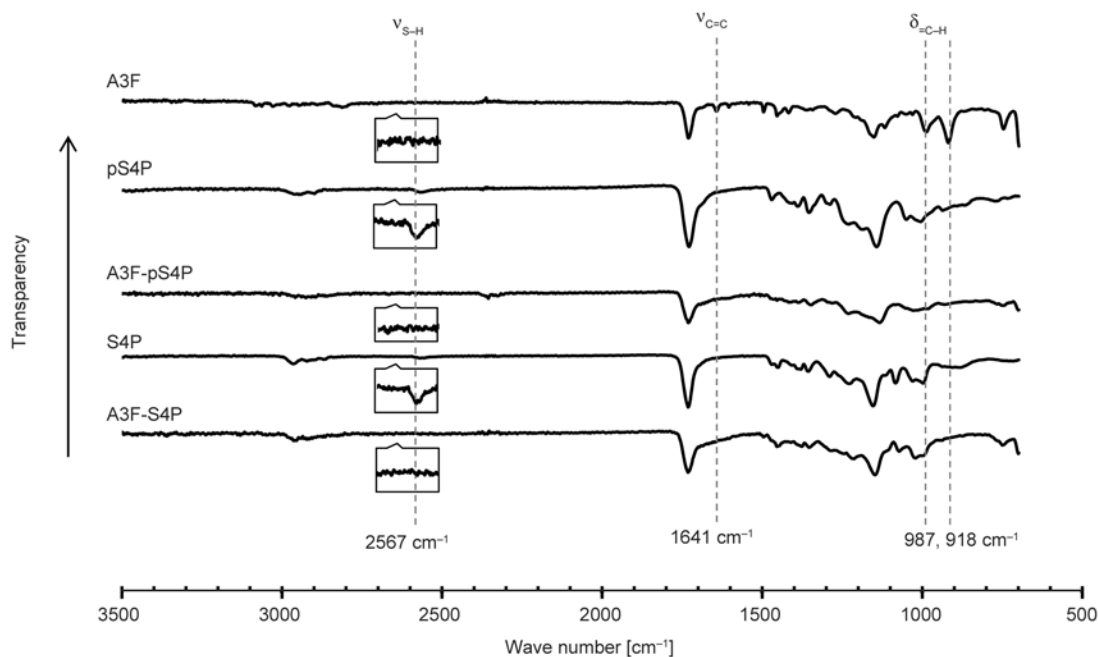


Figure 8. FT-IR spectra of A3F-pS4P and A3F-S4P compared with those of A3F, pS4P and S4P

A3A-pS4P and A3A-S4P. Furthermore, an absorption band due to stretching vibration of S–H group ($\nu_{\text{S-H}}$) at 2567 cm^{-1} which was observed in a longitudinally enlarged spectrum at the wavelength region from 2500 to 2700 cm^{-1} for pS4P or S4P was non-existent for all the cured resins. These results indicate that thiol-ene reaction between allyl and thiol groups almost completely progressed. Although pc-A3A-pS4P was a heterogeneous film with many wrinkles, the thiol-ene photopolymerization considerably proceeded. In a similar manner, smooth progress of thiol-ene thermal polymerizations of A3F with pS4P and S4P was also confirmed, as is obvious from Figure 8. However, the fact that A3F did not produce a fully crosslinked film by thiol-ene photopolymerization suggests that the phenyl group of A3F hinders the photopolymerization at room temperature. Thermal and mechanical properties of the homogeneous film of thermally cured A3A or A3F with pS4P or S4P were investigated in the next section.

3.3. Properties of thermally cured films

Table 1 summarizes the values of D_s for all the thermally cured films dipped in acetone, DMF or water for 48 h. As A3A, A3F, pS4P and S4P are soluble in DMF and acetone, the fact that all the films swelled in the solvents indicates the formation of polymer network. However, the solvents after swelling tests were slightly colored yellow only for A3A-S4P and A3F-S4P in acetone and DMF, suggesting that incompletely crosslinked polymers are slightly formed for the S4P-based cured resins. It is inferred that some side-reactions disturbing the crosslinking reaction occurred because of a lower reactivity of secondary thiol groups of S4P than that of primary thiol groups of pS4P, considering that thiol and allyl groups were almost completely consumed for A3A-S4P and A3F-S4P as is obvious from the FT-IR analysis. If the crosslinking density of S4P-based cured resin is lower than that of pS4P-based cured resin, the D_s of the former resin would be higher than

Table 1. D_s values [%] of A3A-pS4P, A3A-S4P, A3F-pS4P and A3F-S4P films dipped in acetone, DMF or water at room temperature for 48 h

Sample	Acetone	DMF	Water
A3A-pS4P	30.8	109.2	2.0
A3A-S4P	33.0	109.0	1.9
A3F-pS4P	25.7	138.9	1.5
A3F-S4P	21.1	119.5	3.2

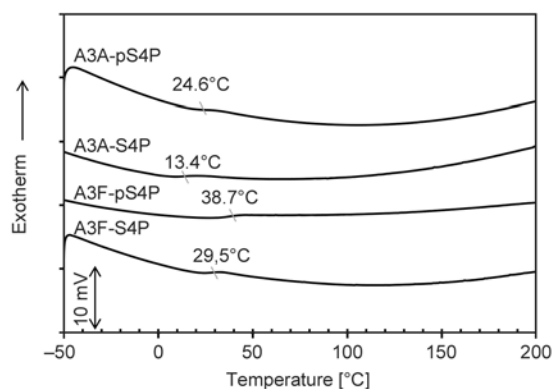


Figure 9. DSC curves of A3A-pS4P, A3A-S4P, A3F-pS4P and A3F-S4P

that of the latter. However, the D_s values of S4P-based cured resins in acetone or DMF were not always larger than those for the corresponding pS4P-based cured resin. This result may be caused by some elution of incompletely crosslinked polymers. The order of a higher D_s value by a difference of dipped solvent was DMF > acetone > water, indicating that the hydrophilicity of the formed polymer network is not so large in agreement with a hydrophobic character of other parts of the polymer network than amino acid residues.

Figure 9 shows the DSC charts of all the thermally cured resins. Every cured resin showed only a T_g at a temperature region from 13 to 39°C , suggesting that the cured resin is amorphous polymer. The T_g s of A3F-pS4P and A3F-S4P (38.7 and 29.5°C) were higher than those of A3A-pS4P and A3A-S4P (24.6 and 13.4°C), attributable to the fact that the former networks have bulky benzyl groups leading to suppression of thermal motion of the polymer chain. Also, T_g s of A3A-pS4P and A3F-pS4P (24.6 and 38.7°C) were higher than those of A3A-S4P and A3F-S4P (13.4 and 29.5°C), respectively. The possibility that S4P-based cured resin has a lower crosslinking density than pS4P-based resin does is also supported from this DSC result.

Figure 10 shows TGA curves of all the cured resins. The T_{5s} of A3F-pS4P and A3F-S4P (282.0 and 266.2°C) were higher than those of A3A-pS4P and A3A-S4P (258.1 and 257.6°C), respectively. This result is attributable to a higher thermal stability of phenylalanine than alanine residue. Also, T_{5s} of A3A-pS4P and A3F-pS4P (258.1 and 282.0°C) were a little higher than those of A3A-S4P and A3F-S4P (257.6 and 266.2°C), respectively. Furthermore, the char yields at ca. 500°C for A3A-pS4P and A3F-pS4P were higher than those for A3A-S4P and A3F-

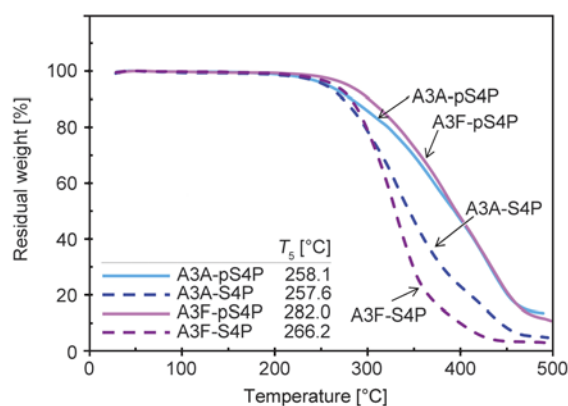


Figure 10. TGA curves of A3A-pS4P, A3A-S4P, A3F-pS4P and A3F-S4P

S4P. These results may be caused by a little higher crosslinking density of the polymer network from pS4P than that from S4P, considering that the crosslinkage prevents the formation of volatile low-molecular-weight fragments even if some bonds of the main chain were cleaved. The T_g s of A3A-S4P and A3F-S4P were comparable to those of polymer networks prepared by the thiol-ene photopolymerizations of S4P and allyl-etherified trehaloses with degrees of allylation of ca. 6 and 8 (251.4 and 289.4°C), respectively, indicating that the amino acid moiety has a similar thermal stability to the saccharide moiety [43]. However the T_g s were lower than that (343.9°C) of the polymer network prepared by the thiol-ene photopolymerization of S4P and allyl-etherified eugenol (AEG) [44], indicating that the amino acid moiety has lower thermal stability than eugenol moiety.

Figure 11 shows typical stress-strain curves by a tensile mode for A3A-pS4P, A3A-S4P, A3F-pS4P and A3F-S4P. It is obvious that a maximal stress of A3F-based cured resin is much higher than that of A3A-based cured resin, and that a strain at break of

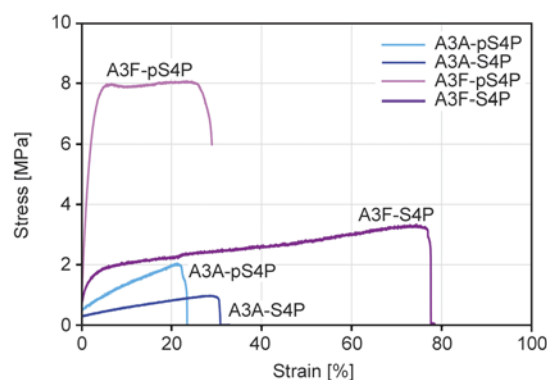


Figure 11. Stress-strain curves of A3A-pS4P, A3A-S4P, A3F-pS4P and A3F-S4P

Table 2. Tensile properties of A3A-pS4P, A3A-S4P, A3F-pS4P and A3F-S4P

Sample	Tensile strength [MPa]	Tensile modulus [MPa]	Elongation at break [%]
A3A-pS4P	2.14±0.67	7.39±1.42	25.2±6.0
A3A-S4P	1.02±0.51	3.90±1.00	27.6±6.6
A3F-pS4P	9.48±2.02	406±129	15.9±8.6
A3F-S4P	3.02±0.66	66.5±55.8	71.8±9.1

S4P-based cured resin is higher than that of pS4P-based cured resin. Table 2 summarizes tensile strength, modulus and elongation at break of the cured resins. Tensile strengths and moduli of A3F-pS4P and A3F-S4P were much higher than those of A3A-pS4P and A3A-S4P, respectively. Especially, the former had much higher tensile moduli than the latter, attributable to the fact that the former network is in glassy state at room temperature, while the latter is in rubbery state, as is obvious from their T_g s. Also, tensile strengths and moduli of A3A-pS4P and A3F-pS4P were higher than those of A3A-S4P and A3F-S4P, respectively. Reversely, the latter displayed higher elongation at break than the former, suggesting that S4P-based polymer network has a lower crosslinking density than pS4P-based polymer network does. Consequently, A3F-pS4P exhibited the highest tensile strength and modulus (9.48 and 406 MPa), whose values were much higher than those of the already reported AEG-pS4P (0.98 and 23.9 MPa) [44]. The difference in the mechanical properties should be caused by the fact that the allyl functionality of A3F (3) is higher than that of AEG (2), leading to a higher crosslinking density.

4. Conclusions

Both *C*- and *N*-terminal allylated amino acid derivatives, A3A and A3F were conveniently synthesized by one-pot reactions of L-alanine and L-phenylalanine with allyl bromide in the presence of sodium hydroxide, respectively. Thiol-ene thermal polymerization of A3A or A3F with pS4P or S4P at allyl/SH 1/1 produced a homogeneous and flat film (A3A-pS4P, A3A-S4P, A3F-S4P or A3F-S3I), while the corresponding photo-curing did not give a successful result. Although all the thermally cured films swelled in acetone, DMF and water, some elution of incompletely crosslinked polymers was observed for the S4P-based cured resins. A higher order of D_s for each cured film was DMF > acetone > water. The T_g s (38.7 and 29.5°C) of A3F-pS4P and A3F-S4P were

higher than those (24.6 and 13.4°C) of A3A-pS4P and A3A-S4P, respectively. The T_{5s} (282.0 and 266.2°C) of A3F-pS4P and A3F-S4P were higher than those (258.1 and 257.6°C) of A3A-pS4P and A3A-S4P, respectively. A3F- and pS4P-based cured resins exhibited much higher tensile strengths and moduli than A3A- and S4P-based cured resins, respectively. A3F-pS4P displayed the highest T_5 (282.0°C), tensile strength (9.5 MPa) and modulus (406 MPa) among all the cured resins. Biodegradability and biocompatibility of these materials are currently under consideration. The methodology in this study is expected to be applied to the preparation of various amino acid-incorporated polymer networks which are applicable to biomaterials.

Acknowledgements

We gratefully acknowledge financial support from the Chiba Institute of Technology. We thank Mr. Shohei Nagashima of our department for his helpful suggestions.

References

- [1] Lokitz B. S., York A. W., Stempka J. E., Treat N. D., Li Y., Jarrett W. L., McCormick C. L.: Aqueous RAFT synthesis of micelle-forming amphiphilic block copolymers containing *N*-acryloylvaline. Dual mode, temperature/pH responsiveness, and ‘locking’ of micelle structure through interpolyelectrolyte complexation. *Macromolecules*, **40**, 6473–6480 (2007). DOI: [10.1021/ma070921v](https://doi.org/10.1021/ma070921v)
- [2] Lokitz B. S., Convertine A. J., Ezell R. G., Heldenreich A., Li Y., McCormick C. L.: Responsive nanoassemblies via interpolyelectrolyte complexation of amphiphilic block copolymer micelles. *Macromolecules*, **39**, 8594–8602 (2006). DOI: [10.1021/ma061672y](https://doi.org/10.1021/ma061672y)
- [3] Oishi T., Lee Y.-K., Nakagawa A., Onimura K., Tsutsumi H. J.: Syntheses and polymerizations of novel chiral poly(acrylamide) macromonomers and their chiral recognition abilities. *Journal of Polymer Science Part A: Polymer Chemistry*, **40**, 1726–1741 (2002). DOI: [10.1002/pola.10250](https://doi.org/10.1002/pola.10250)
- [4] Barbucci R., Casolaro M., Magnani A.: The role of poly electrolytes in the permeability control of insulin: Behavior of poly(*N*-acryloyl-glycine) grafted on porous cellulose membrane. *Journal of Controlled Release*, **17**, 79–88 (1991). DOI: [10.1016/0168-3659\(91\)90133-X](https://doi.org/10.1016/0168-3659(91)90133-X)
- [5] Xu H., Yao Q., Cai C., Gou J., Zhang Y., Zhong H., Tang X.: Amphiphilic poly(amino acid) based micelles applied to drug delivery: The *in vitro* and *in vivo* challenges and the corresponding potential strategies. *Journal of Controlled Release*, **199**, 84–97 (2015). DOI: [10.1016/j.jconrel.2014.12.012](https://doi.org/10.1016/j.jconrel.2014.12.012)
- [6] Roy S. G., Acharya R., Chatterji U., De P.: RAFT polymerization of methacrylates containing a tryptophan moiety: Controlled synthesis of biocompatible fluorescent cationic chiral polymers with smart pH-responsiveness. *Polymer Chemistry*, **4**, 1141–1152 (2013). DOI: [10.1039/c2py20821k](https://doi.org/10.1039/c2py20821k)
- [7] Bauri K., Roy S. G., Pant S., De P.: Controlled synthesis of amino acid-based pH-responsive chiral polymers and self-assembly of their block copolymers. *Langmuir*, **29**, 2764–2774 (2013). DOI: [10.1021/la304918s](https://doi.org/10.1021/la304918s)
- [8] Bauri K., Pant S., Roy S. G., De P.: Dual pH and temperature responsive helical copolymer libraries with pendant chiral leucine moieties. *Polymer Chemistry*, **4**, 4052–4060 (2013). DOI: [10.1039/c3py00434a](https://doi.org/10.1039/c3py00434a)
- [9] Bauri K., De P.: Polyisobutylene-based helical block copolymers with pH-responsive cationic side-chain amino acid moieties by Tandem living polymerizations. *Macromolecules*, **46**, 5861–5870 (2013). DOI: [10.1021/ma401395f](https://doi.org/10.1021/ma401395f)
- [10] Luo C., Zhao B., Li Z.: Dual stimuli-responsive polymers derived from α -amino acids: Effects of molecular structure, molecular weight and end-group. *Polymer*, **53**, 1725–1732 (2012). DOI: [10.1016/j.polymer.2012.02.032](https://doi.org/10.1016/j.polymer.2012.02.032)
- [11] Luo C., Liu Y., Li Z.: Thermo- and pH-responsive polymer derived from methacrylamide and aspartic acid. *Macromolecules*, **43**, 8101–8108 (2010). DOI: [10.1021/ma1015227](https://doi.org/10.1021/ma1015227)
- [12] Mori H., Kato I., Matsuyama M., Endo T.: RAFT polymerization of acrylamides containing proline and hydroxyproline moiety: Controlled synthesis of water-soluble and thermoresponsive polymers. *Macromolecules*, **41**, 5604–5615 (2008). DOI: [10.1021/ma800181h](https://doi.org/10.1021/ma800181h)
- [13] Lu A., Smart T. P., Epps T. H., Longbottom D. A., O’Reilly R. K.: L-proline functionalized polymers prepared by raft polymerization and their assemblies as supported organocatalysts. *Macromolecules*, **44**, 7233–7241 (2011). DOI: [10.1021/ma201256m](https://doi.org/10.1021/ma201256m)
- [14] Skey J., Willcock H., Lammens M., Prez F. D., O’Reilly R. K.: Synthesis and self-assembly of amphiphilic chiral poly(amino acid) star polymers. *Macromolecules*, **43**, 5949–5955 (2010). DOI: [10.1021/ma101019g](https://doi.org/10.1021/ma101019g)
- [15] Klok H.-A., Langenwalter J. F., Lecommandoux S.: Self-assembly of peptide-based diblock oligomers. *Macromolecules*, **33**, 7819–7826 (2000). DOI: [10.1021/ma0009606](https://doi.org/10.1021/ma0009606)
- [16] Mori H., Kato I., Saito S., Endo T.: Proline-based block copolymers displaying upper and lower critical solution temperatures. *Macromolecules*, **43**, 1289–1298 (2010). DOI: [10.1021/ma902002b](https://doi.org/10.1021/ma902002b)

- [17] Skey J., Hansell C. F., O'Reilly R. K.: Stabilization of amino acid derived diblock copolymer micelles through favorable D:L side chain interactions. *Macromolecules*, **43**, 1309–1318 (2010). DOI: [10.1021/ma902356u](https://doi.org/10.1021/ma902356u)
- [18] Mori H., Matsuyama M., Sutoh K., Endo T.: RAFT polymerization of acrylamide derivatives containing L-phenylalanine moiety. *Macromolecules*, **39**, 4351–4360 (2006). DOI: [10.1021/ma052756u](https://doi.org/10.1021/ma052756u)
- [19] Sanda F., Nakamura M., Endo T.: Syntheses and radical copolymerization behavior of optically active methacrylamides having L- and D-leucine moieties. Interaction between L- and D-forms. *Macromolecules*, **29**, 8064–8068 (1996). DOI: [10.1021/ma960906i](https://doi.org/10.1021/ma960906i)
- [20] Casolaro M.: Vinyl polymers containing L-valine and L-leucine residues: Thermodynamic behavior of homopolymers and copolymers with N-isopropylacrylamide. *Macromolecules*, **28**, 2351–2358 (1995). DOI: [10.1021/ma00111a031](https://doi.org/10.1021/ma00111a031)
- [21] Sanda F., Nakamura M., Endo T., Takata T., Handa H.: Synthesis of novel optically active polymethacrylamide having L-leucine structure in the side chain. *Macromolecules*, **27**, 7928–7929 (1994). DOI: [10.1021/ma00104a059](https://doi.org/10.1021/ma00104a059)
- [22] Safranji A., Yoshida M., Omichi H., Katakai R.: Surfactant effect on the inverse volume phase transition of a polymer with amino acid side chains. *Langmuir*, **9**, 3338–3340 (1993). DOI: [10.1021/la00036a003](https://doi.org/10.1021/la00036a003)
- [23] Roy S. G., Haldar U., De P.: Remarkable swelling capability of amino acid based cross-linked polymer networks in organic and aqueous medium. *ACS Applied Materials and Interfaces*, **6**, 4233–4241 (2014). DOI: [10.1021/am405932f](https://doi.org/10.1021/am405932f)
- [24] Roy S. G., De P.: Swelling properties of amino acid containing cross-linked polymeric organogels and their respective polyelectrolytic hydrogels with pH and salt responsive property. *Polymer*, **55**, 5425–5434 (2014). DOI: [10.1016/j.polymer.2014.08.072](https://doi.org/10.1016/j.polymer.2014.08.072)
- [25] Kumar S., Roy S. G., De P.: Cationic methacrylate polymers containing chiral amino acid moieties: Controlled synthesis *via* RAFT polymerization. *Polymer Chemistry*, **3**, 1239–1248 (2012). DOI: [10.1039/c2py00607c](https://doi.org/10.1039/c2py00607c)
- [26] Sun H., Gao C.: Facile synthesis of multiamino vinyl poly(amino acid)s for promising bioapplications. *Biomacromolecules*, **11**, 3609–3616 (2010). DOI: [10.1021/bm101060m](https://doi.org/10.1021/bm101060m)
- [27] Adams D. J., Atkins D., Cooper A. I., Furzeland S., Trewin A., Young I.: Vesicles from peptidic side-chain polymers synthesized by atom transfer radical polymerization. *Biomacromolecules*, **9**, 2997–3003 (2008). DOI: [10.1021/bm8006693](https://doi.org/10.1021/bm8006693)
- [28] Obeid R., Scholz C.: Synthesis and self-assembly of well-defined poly(amino acid) end-capped poly(ethylene glycol) and poly(2-methyl-2-oxazoline). *Biomacromolecules*, **12**, 3797–3804 (2011). DOI: [10.1021/bm201048x](https://doi.org/10.1021/bm201048x)
- [29] Hadjichristidis N., Iatrou H., Pitsikalis M., Sakellariou G.: Synthesis of well-defined polypeptide-based materials via the ring-opening polymerization of α -amino acid *N*-carboxyanhydrides. *Chemical Reviews*, **109**, 5528–5578 (2009). DOI: [10.1021/cr9000049t](https://doi.org/10.1021/cr9000049t)
- [30] Lu H., Cheng J.: Hexamethyldisilazane-mediated controlled polymerization of α -amino acid *N*-carboxyanhydrides. *Journal of the American Chemical Society*, **46**, 14114–14115 (2007). DOI: [10.1021/ja074961q](https://doi.org/10.1021/ja074961q)
- [31] Mallakpour S., Khani M.: Construction of chiral polyesters from polycondensation of multifunctional monomer containing both flexible amino acid and rigid pendant groups with aromatic diols. *Amino Acids*, **39**, 841–848 (2010). DOI: [10.1007/s00726-010-0539-x](https://doi.org/10.1007/s00726-010-0539-x)
- [32] Blocher M., Liu D., Luisi L.: Liposome-assisted selective polycondensation of α -amino acids and peptides: The case of charged liposomes. *Macromolecules*, **33**, 5787–5796 (2000). DOI: [10.1021/ma000540g](https://doi.org/10.1021/ma000540g)
- [33] Kiyotsukuri T., Nagata M., Kitazawa T., Tsutsumi N.: Synthesis of polymers from α -amino acids by polyaddition. *European Polymer Journal*, **27**, 183–186 (1992). DOI: [10.1016/0014-3057\(92\)90305-L](https://doi.org/10.1016/0014-3057(92)90305-L)
- [34] Li Y., Xiao F., Moon K-S., Wong C. P.: Novel curing agent for lead-free electronics: Amino acid. *Journal of Polymer Science Part A: Polymer Chemistry*, **44**, 1020–1027 (2006). DOI: [10.1002/pola.21239](https://doi.org/10.1002/pola.21239)
- [35] Li Y., Xiao F., Wong C. P.: Novel, environmentally friendly crosslinking system of an epoxy using an amino acid: Tryptophan-cured diglycidyl ether of bisphenol A epoxy. *Journal of Polymer Science Part A: Polymer Chemistry*, **45**, 181–190 (2007). DOI: [10.1002/pola.21742](https://doi.org/10.1002/pola.21742)
- [36] Ozawa Y., Shibata M.: Biobased thermosetting resins composed of L-lysine methyl ester and bismaleimide. *Journal of Applied Polymer Science*, **131**, 40379/1–40379/8 (2014). DOI: [10.1002/app.40379](https://doi.org/10.1002/app.40379)
- [37] Lowe A. B.: Thiol-ene 'click' reactions and recent applications in polymer and materials synthesis: A first update. *Polymer Chemistry*, **5**, 4820–4870 (2014). DOI: [10.1039/C4PY00339J](https://doi.org/10.1039/C4PY00339J)
- [38] Lowe A. B.: Thiol-ene 'click' reactions and recent applications in polymer and materials synthesis. *Polymer Chemistry*, **1**, 17–36 (2010). DOI: [10.1039/b9py00216b](https://doi.org/10.1039/b9py00216b)

- [39] Dondoni A.: The emergence of thiol–ene coupling as a click process for materials and bioorganic chemistry. *Angewandte Chemie International Edition*, **47**, 8995–8997 (2008).
DOI: [10.1002/anie.200802516](https://doi.org/10.1002/anie.200802516)
- [40] Morgan C. R., Magnotta F., Ketley A. D.: Thiol/ene photocurable polymers. *Journal of Polymer Science: Polymer Chemistry Edition*, **15**, 627–645 (1977).
DOI: [10.1002/pol.1977.170150311](https://doi.org/10.1002/pol.1977.170150311)
- [41] Echeverri D. A., Cádiz V., Ronda J. C., Rios L. A.: Synthesis of elastomeric networks from maleated soybean-oil glycerides by thiol-ene coupling. *European Polymer Journal*, **48**, 2040–2049 (2012).
DOI: [10.1016/j.eurpolymj.2012.09.004](https://doi.org/10.1016/j.eurpolymj.2012.09.004)
- [42] Ortiz R. A., Martínez A. Y. R., Valdez A. E. G., Duarte M. L. B.: Preparation of a crosslinked sucrose polymer by thiol–ene photopolymerization using dithiothreitol as comonomer. *Carbohydrate Polymers*, **82**, 822–882 (2010).
DOI: [10.1016/j.carbpol.2010.05.054](https://doi.org/10.1016/j.carbpol.2010.05.054)
- [43] Nagashima S., Shimasaki T., Teramoto N., Shibata M.: Trehalose-incorporated polymer network by thiol-ene photopolymerization. *Polymer Journal*, **46**, 728–735 (2014).
DOI: [10.1038/pj.2014.53](https://doi.org/10.1038/pj.2014.53)
- [44] Yoshimura T., Shimasaki T., Teramoto N., Shibata M.: Bio-based polymer networks by thiol–ene photopolymerizations of allyl-etherified eugenol derivatives. *European Polymer Journal*, in press (2015).
DOI: [10.1016/j.eurpolymj.2014.11.013](https://doi.org/10.1016/j.eurpolymj.2014.11.013)
- [45] Karmann L., Kazmaier U.: Thiol-ene click reactions – Versatile tools for the modification of unsaturated amino acids and peptides. *European Journal of Organic Chemistry*, **31**, 7101–7109 (2013).
DOI: [10.1002/ejoc.201300672](https://doi.org/10.1002/ejoc.201300672)
- [46] Tang W., Becker M.: ‘Click’ reactions: A versatile toolbox for the synthesis of peptide-conjugates. *Chemical Society Reviews*, **43**, 7013–7039 (2014).
DOI: [10.1039/c4cs00139g](https://doi.org/10.1039/c4cs00139g)